

DISSERTATION

DEVICE CHARACTERIZATION OF CADMIUM TELLURIDE PHOTOVOLTAICS

Submitted by

Russell M. Geisthardt

Department of Physics

In partial fulfillment of the requirements

For the Degree of Doctor of Philosophy

Colorado State University

Fort Collins, Colorado

Summer 2014

Doctoral Committee:

Advisor: James Sites

Martin Gelfand

Marko Topič

W. S. Sampath

Copyright by Russell Geisthardt 2014

All Rights Reserved

ABSTRACT

DEVICE CHARACTERIZATION OF CADMIUM TELLURIDE PHOTOVOLTAICS

Thin-film photovoltaics have the potential to make a large impact on the world energy supply. They can provide clean, affordable energy for the world. Understanding the device physics and behavior will enable increases in efficiency which will increase their impact. This work presents novel approaches for evaluating efficiency, as well as a set of tools for in-depth whole-cell and uniformity characterization.

The understanding of efficiency losses is essential for reducing or eliminating the losses. The efficiency can be characterized by a breakdown into three categories: solar spectrum, optical, and electronic efficiency. For several record devices, there is little difference in the solar spectrum efficiency, modest difference in the optical efficiency, and large difference in the electronic efficiency.

The losses within each category can also be further characterized. The losses due to the broad solar spectrum and finite temperature are well understood from a thermodynamic physics perspective. Optical losses can be fully characterized using quantum efficiency and optical measurements. Losses in fill factor can be quantified from series and shunt resistance, as well as the expected fill factor from the measured V_{oc} and A . Open-circuit voltage losses are the most significant, but are also be the hardest to understand, as well as the most technology-dependent.

Characterization of the whole cell helps to understand the behavior, performance, and properties of the cell. Several different tools can be used for whole-cell characterization, including current-voltage, quantum efficiency, and capacitance measurements. Each of these tools give specific information about the behavior of the cell. When combined, they can lead to a more complete understanding of the cell performance than when taken individually.

These tools were applied to several specific CdTe experiments. They have helped to characterize the baseline performance of both the deposition tool and the measurement

systems. Characterization of plasma-cleaned cells show an improvement in performance, even at thinner CdS layer thickness. Measurements of thinning CdTe samples reveal additional optical losses, likely caused by the increasing importance of the back diode. Characterization of Cd(S,O) devices show improved performance, both from improved optical properties and theorized improvement in band alignment properties.

Uniformity can have an effect on whole-cell performance, but can also be an important parameter to characterize on its own. Light-beam-induced current is a powerful tool for characterizing uniformity. The LBIC tool was upgraded to improve its accuracy, functionality, and speed.

The improved LBIC system aids in the collection of uniformity data. A number of parameters can be varied to provide in-depth uniformity information and help identify causes of nonuniformity. The wavelength can be varied to provide information on different layers. This can help identify variations in CdS thickness and local CdTe band gap. An applied voltage bias can be used to identify locations with weak diode properties. The resolution can also be varied to provide information on nonuniformities at different scales, from variations across the whole cell to variations on the size of several grains. LBIC can also be paired with electroluminescence to create a powerful nonuniformity characterization suite. The two can be paired with EL used as a screening tool to identify cells or areas which need further characterization from LBIC.

ACKNOWLEDGMENTS

Thank you first of all to my advisor, Jim Sites. None of this would have been possible without your leadership, guidance, and wisdom. By trusting in my abilities, you have allowed me to grow into an independent researcher. Your always tactful corrections have helped me to do the best work possible. Thank you as well to Marko Topič, W.S. Sampath, and Martin Gelfand for your guidance on and contributions to my research.

Thank you to the physics communities that have helped me grow, both at Lawrence University and at Colorado State University. My professors, especially Profs. Cook and Brandenberger, have shown me the joy of physics, and my fellow students, especially Chris, Praveen, Dan, Jacob, Max, Bao, Will, and Stefany, have helped me through the challenges of physics.

Thank you to everyone who has helped with the PV research at CSU: Ray Hsiao, Galym Koishiyev, Jun Pan, Marcel Baltès, Matevež Bokalič, Samaneh Sharbati, Zhipeng Huang, Elliot Best, Isaac Gonzalez, Tao Song, Andy Moore, Tyler McGoffin, Katherine Zaunbrecher, Jennifer Drayton, Paul Kobayakov, Jason Kephart, Kurt Barth, Kevan Cameron, Amit Munshi, Mohammed Tashkandi, Tushar Shimpi, and especially Drew Swanson and John Raguse for our many long and often-productive discussions. And thank you to all the students who came before who built the amazing structure to which I added a tiny component.

Thank you to my family and friends for your encouragement and support all along the way. Most importantly, thank you to Laura, for going on this crazy adventure with me. I cannot even express how much better this journey has been because of your constant support.

TABLE OF CONTENTS

Abstract	ii
Acknowledgments	iv
Table of Contents	v
List of Figures	vii
List of Tables	ix
1 Introduction	1
1.1 The World Energy Problem	1
1.2 The Case for CdTe Photovoltaics	2
2 Background	3
2.1 Physics of Thin-Film Photovoltaics	3
2.2 CdTe Device Structure	5
2.3 Measurement of Thin-Film Photovoltaics	6
2.3.1 Current Density-Voltage	7
2.3.2 Current-Voltage Analysis	8
2.3.3 Quantum Efficiency	10
2.3.4 Capacitance	12
2.3.5 Uniformity Measurements	13
3 Efficiency Analysis and Limits	14
3.1 Breakdown of Efficiency	14
3.1.1 Ideal Efficiency Parameters	15
3.1.2 Analysis of Record Cells	17
3.2 Solar Spectrum Efficiency Limit	20
3.3 Short-Circuit Current Density Analysis	22
3.4 Fill Factor Analysis	25
3.5 Open-Circuit Voltage Analysis	27
3.6 Variation of Spectrum, Temperature, and other Extensions	33
4 Whole-cell Characterization	35
4.1 Upgrades and Additions to Whole-Cell Characterization Systems	35
4.1.1 Upgrades	35
4.1.2 New Tools	38
4.2 Whole-Cell Measurement and Analysis Tools	40
4.2.1 Current Voltage	40
4.2.2 Quantum Efficiency and Optical Measurements	41
4.2.3 Capacitance	43
4.3 Applications to CdTe Experiments	44
4.3.1 Baseline Process	44
4.3.2 Plasma Cleaning	45

4.3.3	Thinning CdTe	46
4.3.4	High-Efficiency Cd(S,O)/CdTe Devices	48
4.4	Relationship between Uniformity and Whole-Cell Performance	52
5	LBIC Expansion and Improvement	57
5.1	Hardware Upgrades	58
5.1.1	405 nm Laser	58
5.1.2	Noise Reduction Efforts	61
5.1.3	Other Upgrades and Repairs	65
5.2	Software Upgrades	65
5.2.1	Data Viewer and Sub-Area Selector	66
5.2.2	Reduced Measurement Time	67
6	General Strategy for Nonuniformity Characterization using LBIC	74
6.1	Wavelength Dependence	74
6.2	Voltage Bias Dependence	78
6.3	Resolution Dependence	80
6.4	EL and LBIC as Complementary Tools	83
7	Conclusions	88
	Bibliography.	92

LIST OF FIGURES

2.1	Band diagram of typical cell	4
2.2	Equivalent circuit of a solar cell	5
2.3	Structural diagram of typical CdTe cell.	6
2.4	J-V curve of typical CdTe cell	7
2.5	Current-voltage analysis of several cells.	9
2.6	Quantum efficiency of a typical CdTe cell	11
3.1	Efficiency breakdown of record cells.	18
3.2	Efficiency breakdown of CdTe and GaAs cells	19
3.3	Losses due to solar spectrum and finite temperature	21
3.4	Ideal values for J_{sc} , V_{oc} , FF , and η with varying E_g	22
3.5	Accounting of losses in short-circuit current	23
3.6	Loss accounting in crystalline silicon	30
3.7	Semi-log J-V plot	31
3.8	V_{oc} vs T graphs for two sets of CdTe cells	32
4.1	Updates to the QE reference cell	37
4.2	Three cells measured seven times each	45
4.3	J-V measurements varying speed and direction	45
4.4	Results from the plasma cleaning experiment	47
4.5	Results from the thinning CdTe experiment	48
4.6	Results from replacing the CdS with Cd(S,O)	50
4.7	High efficiency cell using an HRT and Cd(S,O)	51
4.8	Improvement in efficiency and uniformity with plasma cleaning.	53
4.9	Histogram of uniformity measurements before and after stress	54
4.10	Images of uniformity measurements before and after stress	55

4.11	LBIC of a shunted cell	56
5.1	Diagram of CSU LBIC system	57
5.2	High resolution LBIC scans showing a region of thin CdS	59
5.3	High resolution LBIC scans showing a region of low oxygen Cd(S,O).	60
5.4	Cell response over time with old and new laser diode controllers	62
5.5	LBIC scans using electrically modulated and optically chopped light.	63
5.6	Ratio of cell to monitor signal before and after noise reduction	64
5.7	Data viewer and area selector	66
5.8	Illustration of stepped and continuous LBIC measurement process	68
5.9	LBIC scans using different speeds	69
5.10	LBIC scans at medium and high resolution using different speeds	71
5.11	LBIC scans with varying lock-in parameters and chopping frequencies.	73
6.1	QE of sample cell at varying voltage biases	75
6.2	LBIC scans at four different wavelengths.	76
6.3	Line scans using four different wavelengths.	77
6.4	LBIC scans using four different voltage biases	79
6.5	Line scans using four different voltage biases.	80
6.6	LBIC scans with wavelength and voltage bias variation	81
6.7	LBIC scans at different resolutions	82
6.8	J-V curves showing location of EL and LBIC measurements.	84
6.9	Comparison of EL and LBIC images	86
6.10	Comparison of EL and LBIC images with different passivations.	87

LIST OF TABLES

3.1	Short-circuit current density losses in a typical CSU CdTe cell	24
3.2	Fill factor losses in record cells.	27
3.3	Efficiency at different spectral and temperature conditions	33

Chapter 1

INTRODUCTION

1.1 The World Energy Problem

The world energy use in 2010 was above 500 quadrillion BTU, which means an average power use over 17 TW. The majority of this energy comes from burning fossil fuels [1]. This energy, and the growth in energy use, has allowed for great economic and standard-of-living development around the world. However, the use of fossil fuels has several major drawbacks. The first is the finite supply of earth-extracted fuels, which is a corollary of the round-earth theory. Although estimates of reserves differ, and have changed significantly over time, the finite supply will eventually forcibly curtail the use of fossil fuels. The second drawback, even before supply is reduced, is the pollution created by burning fossil fuels. This can be cleaned somewhat, though not completely. The pollution is often concentrated near population centers, and can lead to decreased health and quality of life. A final, and most significant, problem with fossil fuels is their contribution to climate change [2]. The increase in atmospheric greenhouse gases due to burning of fossil fuels has already begun affecting the climate. The effects will continue to increase if alternatives are not implemented.

Several possible alternative sources of energy are available, including nuclear, wind, hydro, geothermal, and solar. Wind, hydro, and geothermal suffer from a lack of total capacity [3]. Nuclear suffers from the same supply limit as fossil fuels, and has the added difficulty of waste management. Of these alternatives, solar stands out for its total potential, since several orders of magnitude more solar power strikes the earth than is used for all global power use. Solar is also competitive on the basis of cost, with cost dropping near or below grid parity in many markets [4]. Solar is also easily distributable, and can be deployed easily in energy-starved regions of the world. Although many different sources of energy will probably be used in the near term, solar is likely to be a major player in the long term.

1.2 The Case for CdTe Photovoltaics

Solar energy can be converted using thermal systems or photovoltaics (PV). PV can be made using crystalline materials (Si or GaAs), multiple junctions, or polycrystalline thin-films. Of these, polycrystalline thin-films, such as Cu(In,Ga)Se₂ or CdTe, offer several potential advantages. Since these cells are made with thin films, the materials usage is much lower, which reduces cost and materials needs. Less material and lower purity requirements also mean lower embodied energy, which means the energy payback time can be well under a year [5]. Although CdTe cells have historically underperformed crystalline Si cells (the dominant technology in the market), the gap has been reduced significantly in recent years [6]. CdTe is also easily manufacturable by a variety of methods, such as closed-space sublimation, vapor transport deposition, or molecular beam epitaxy [7].

Although the efficiency of most types of cells have increased over recent years, further gains in efficiency will continue to be beneficial. Improved efficiency helps to reduce the cost of the cells and panels, but it also reduces balance of system costs, since the same area or number of panels can provide more energy. Improved efficiency will make solar PV better able to supply the world's energy needs.

The goal of this work is to provide tools which can aid in improving cell efficiency, especially of CdTe cells. The analysis framework in Chapter 3 helps identify sources of efficiency loss. The remaining chapters deal with characterization and measurement tools which can be used to identify problems with individual cells. Cells will be examined both for whole-cell behavior and for uniformity. Improvements in these tools and characterization strategies for using these tools provide a path towards further gains in efficiency.

Chapter 2

BACKGROUND

This chapter contains the background which will be useful for reading this dissertation. It will describe the basic physics of photovoltaic devices, with special emphasis on thin-film CdTe devices, and the measurement tools used for characterizing these devices.

2.1 Physics of Thin-Film Photovoltaics

A photovoltaic device is generally a p-n semiconductor junction. As the n-type and p-type materials are brought together, free carriers flow between the materials to neutralize charged ions. This imbalance in charge produces an electric field which inhibits further flow of carriers. The result is a depletion region which has a depleted concentration of carriers and has a built in electric field.

Fig. 2.1 shows the band structure of a typical CdTe solar cell. Due to the low carrier concentration and thin layer, the depletion region covers the entire CdTe layer. This figure also illustrates the process by which current is created from light. A photon is absorbed in the cell and excites an electron from the valence to conduction band and leaves behind a hole in the valence band. Due to the electric field, the electron is directed towards the n-type side, and the hole further into the p-type side. If the front and back contacts are shorted, the flow of electrons and holes creates current.

As a forward voltage bias is applied to the cell, the Fermi Level is split by an energy equal to $q \cdot V_{applied}$. This shifts the n-type bands to higher energy relative to the p-type bands. This lessens the barrier, which allows electron flow from the n-type layer into the p-type layer, a current flow which is opposite in direction from the light-generated current flow. The increased current flow under applied bias, V , follows the exponential behavior of

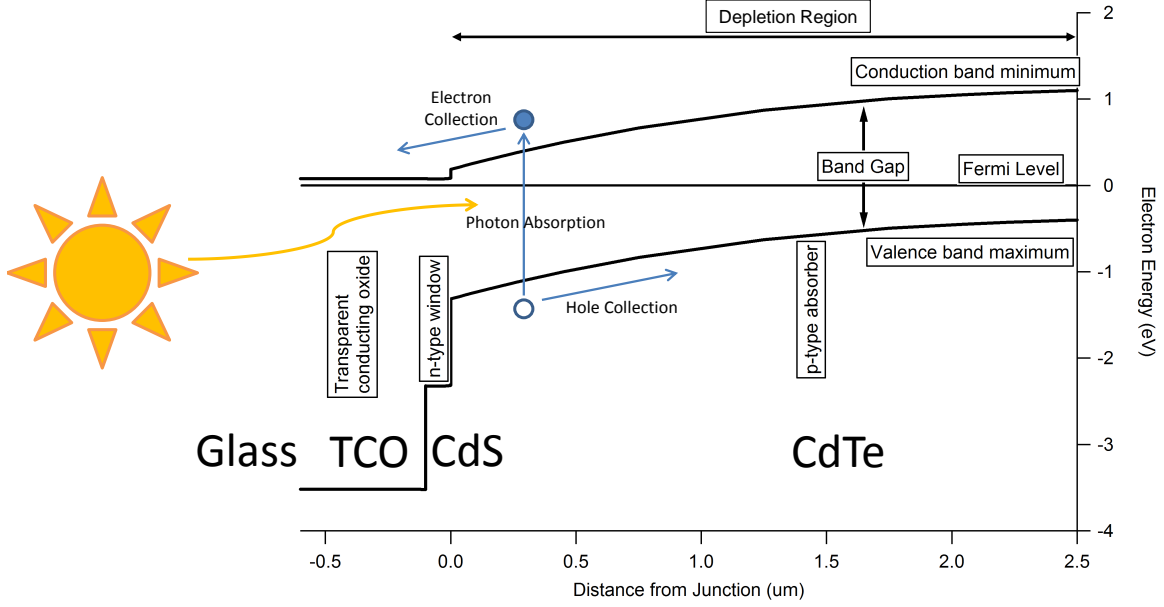


Figure 2.1: Band diagram of a typical CdTe solar cell.

the diode equation:

$$J = J_0(e^{qV/kT} - 1) - J_L \quad (2.1)$$

where currents have been normalized to the cell area, and where J_0 is the saturation current density, q the electron charge, k the Boltzmann constant, T the cell temperature, and J_L the light-generated current density.

Eq. 2.1 assumes that the primary forward current mechanism is electrons overcoming the barrier, a process known as thermionic emission. However, significant current flow can also come from recombination. In this case, the effective barrier height is reduced, and the exponent of e becomes $qV/2kT$. Intermediate cases are also possible, so it is useful to introduce a factor A , the diode quality factor, which can range from 1 to 2.

There can also be parasitic resistances in the circuit, either in parallel with or in series with the diode. The parallel component is called the shunt resistance, r_{sh} , and the series component the series resistance, R_s . An equivalent circuit diagram is given in Fig. 2.2. The combination of all these elements produces the standard photovoltaic diode equation

$$J = J_0 \left(e^{\frac{q(V-JR_s)}{AkT}} - 1 \right) + \frac{V - JR_s}{r_{sh}} - J_L \quad (2.2)$$

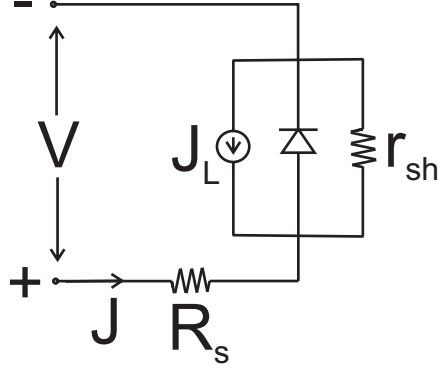


Figure 2.2: Equivalent circuit of a solar cell.

2.2 CdTe Device Structure

The cells measured in this dissertation are all CdTe cells manufactured in the Colorado State University (CSU) PV Manufacturing Laboratory, except where outside published results are used. A diagram of the standard structure is shown in Fig. 2.3. The cells are deposited in a superstrate structure, where the cell is deposited from the front to the back, and the light comes in through the front glass. The glass and transparent conductor are commercially-available products, often called TEC 10, where the 10 refers to the sheet resistance of the TCO in Ω/\square . Although it is not shown here, there can also be a high-resistance layer, or buffer, between the TCO and CdS.

The n-type layer is CdS. It is usually deposited by closed-space sublimation (CSS) to a thickness around 100 nm. CSS is a process where a cooler substrate is held above a hotter pocket containing the source material. The material sublimates, travels up to the substrate, and condenses on the cooler substrate. In addition to the standard CdS process, experiments in the following chapters will look at varying the thickness of CdS as well as varying the composition through sputter deposition in oxygen. The CdTe layer is also deposited by CSS to a thickness around 2 μm . A layer of CdCl_2 is deposited, annealed, and removed. A layer

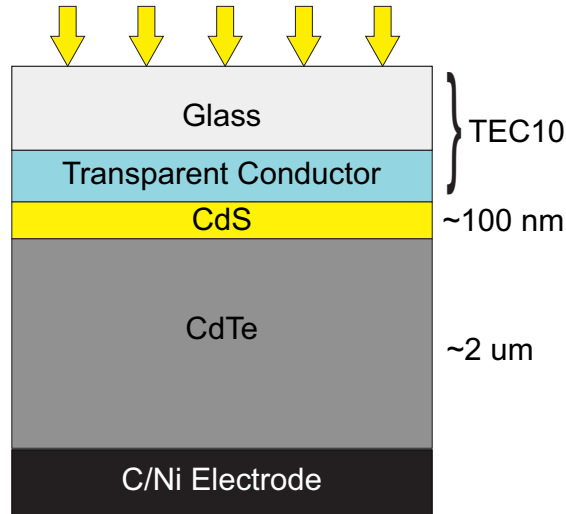


Figure 2.3: Structural diagram of a typical CdTe solar cell.

of copper is also applied. These steps are all performed in a single vacuum chamber, which is described in [8].

The device is finished outside of the vacuum chamber. The back contact is a sprayed-on layer of carbon paint, followed by sprayed-on layers of nickel paint. The cell is delineated into a circular shape, around 1 cm in diameter, using a blasting process around a mask. Deposition is done onto a substrate which is approximately 3 in by 3 in. Each substrate is turned into 9 finished devices in a 3 by 3 pattern.

2.3 Measurement of Thin-Film Photovoltaics

Several different tools are used for characterizing the performance and behavior of solar cells. This section will provide a basic description of these tools and their setups. Further descriptions of the information provided by these measurements will be provided in later chapters.

2.3.1 Current Density-Voltage

Several parameters which describe the performance of a cell can be obtained from a current-voltage, or I-V, measurement, which is then normalized to the cell area as a current density-voltage, or J-V graph. This is a measure of the output current as a function of applied voltage bias, both in the dark and in the light. Sample results are shown in Fig. 2.4. The dark curve shows the standard diode behavior with an exponential turn-up at forward bias. The light curve is shifted down by the light-generated current.

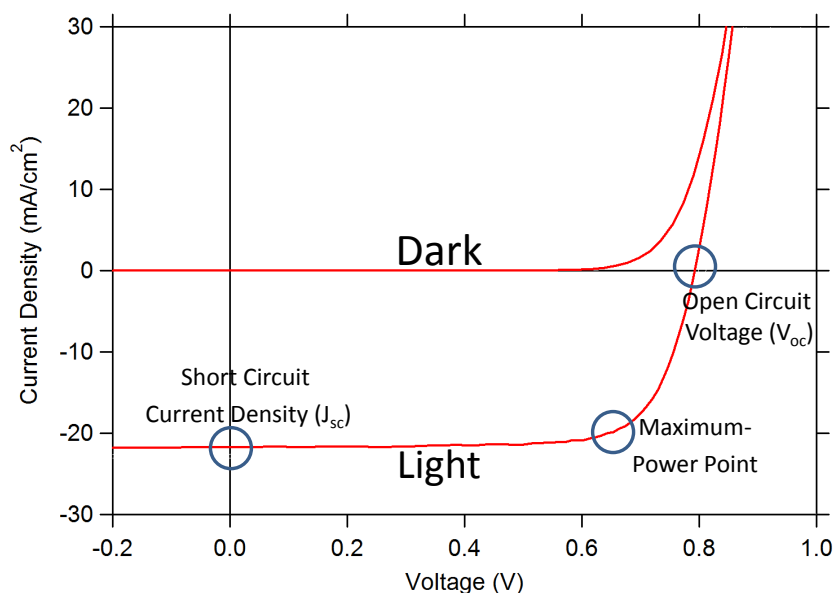


Figure 2.4: J-V curve of a typical CdTe solar cell.

Several important points are illustrated in the figure. The short-circuit current density, J_{sc} , is the current density at zero bias. It is often assumed to be the same as the light-generated current, though this assumption is frequently violated when the light-generated current is voltage dependent. The open-circuit voltage, V_{oc} , is the voltage at which the current is zero. The maximum-power point is the point at which the output power density, $|J \cdot V|$, is maximized in the power-generating quadrant. It also defines the maximum-power current density and voltage, J_{mp} and V_{mp} , respectively. A third parameter, fill factor, can

be defined as

$$FF = \frac{J_{mp}V_{mp}}{J_{sc}V_{oc}} \quad (2.3)$$

and is the measure of how well the curve fills the box bounded by J_{sc} and V_{oc} .

The final parameter is efficiency. This is defined as the power out as a fraction of the power in. For a solar cell, the output power is the electrical power from the maximum-power point of the J-V curve. The input power is the solar power shining on the cell, which usually defined by the AM1.5 spectrum (IEC 60904-3, Ed. 2, 2008 or ASTM G173-03). The spectrum has an integrated irradiance of 100 mW/cm². The efficiency can be written as

$$\eta = \frac{J_{sc}V_{oc}FF}{P_{in}} \quad (2.4)$$

where η is the efficiency and P_{in} is the light power incident on the cell.

Standard test conditions are an AM1.5 spectrum with 100 mW/cm² of irradiance at 25°C. All three of these conditions can be varied, however, to provide additional information.

In the CSU J-V system the light is provided by a xenon arc lamp with filters to approximate the standard spectrum. Applied bias and current and voltage measurement is provided by a Keithley 2401 sourcemeter. A four-point measurement system is used to minimize resistive losses in the external circuit. Spectral control is provided by color filters, and irradiance control by neutral-density filters. Temperature control can be provided by thermoelectric coolers and liquid nitrogen.

2.3.2 Current-Voltage Analysis

It is desirable to know the values of the parameters which make up the diode equation, Eq. 2.2. A fitting algorithm, however, is often insufficient for dealing with non-idealities in the behavior of the cell which do not fit the equation well. To solve this, a series of linearizations were implemented for current-voltage analysis, often called CurVA. These steps are illustrated in Fig. 2.5 for three cells, both in the dark and in the light.

Part a of Fig. 2.5 is simply the standard J-V plot. The first linearization appears in part b, which graphs dJ/dV against voltage. At zero or reverse bias, the value of the ordinate is

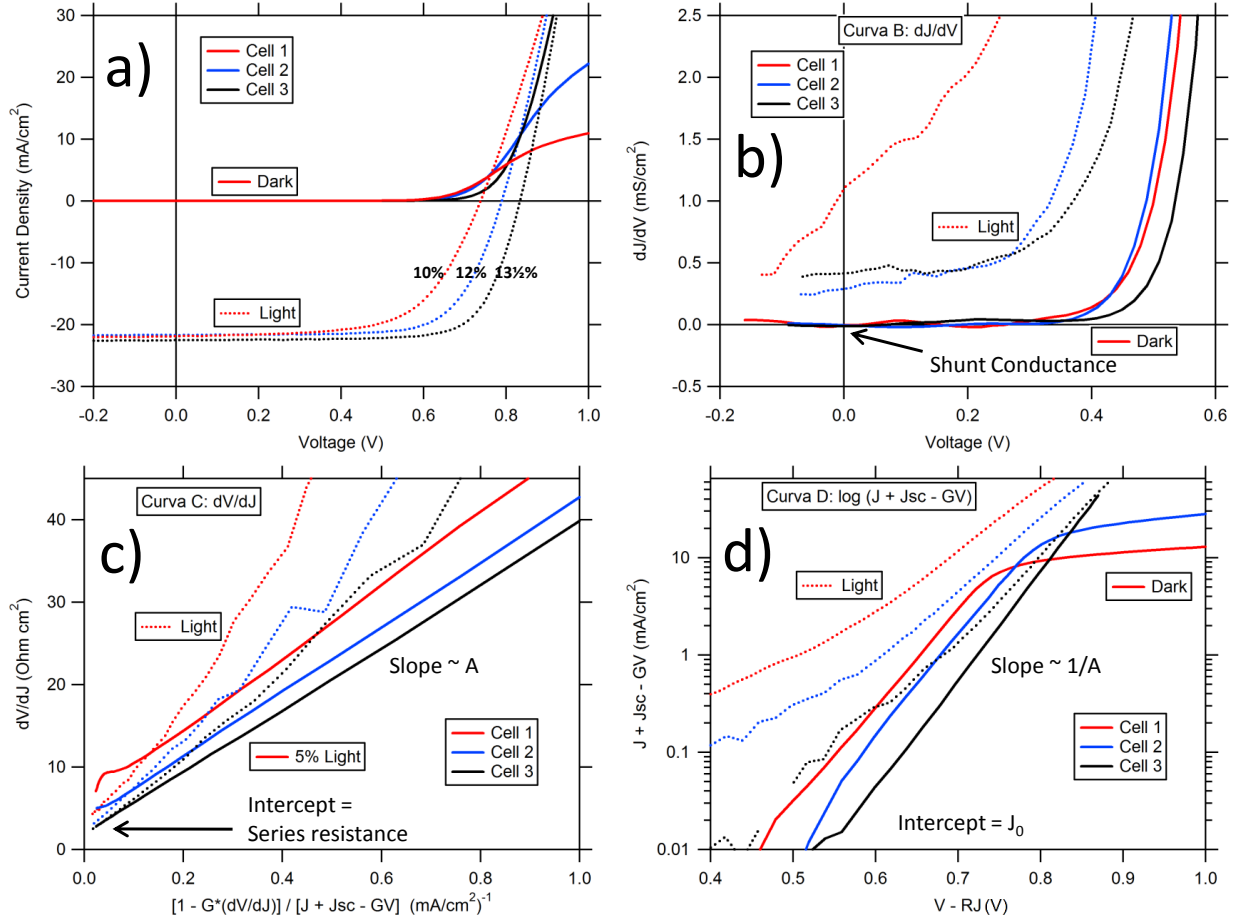


Figure 2.5: Current-voltage analysis of several cells in the dark and the light

the shunt conductance, $1/r_{sh}$. This can be poorly defined, as in the case of the light curve for cell 1. This often means that an apparent shunt resistance is actually caused by a voltage-dependent light-generated current. The extraction of the shunt resistance also assumes that the series resistance is small enough to have little effect in reverse bias.

The second linearization is shown in part c. This plots the inverted derivative dV/dJ against $1/(J + J_{sc})$ when the latter value is corrected for the shunt resistance. This should produce a straight line, which has intercept of series resistance and slope of AkT/q , from which A can be calculated. As can be seen from the light curves, nonlinear behavior often complicates this analysis.

The third linearization is shown in part d. Here, $J + J_{sc}$ is plotted on a logarithmic scale against V , where these values are corrected for the shunt resistance found in part b and the series resistance found in part c, respectively. This should again be linear, with a y-intercept of J_0 and slope of q/AkT . In this case, the dark curves show non-ideal behavior. For the non-ideal dark curves, the left-most portion was used for the linear fit, since the right portion would give unreasonable values. Values for A are calculated from both parts c and d, which provides a useful cross-check of calculated values.

The CurVA method provides a reliable method for extracting the full set of diode parameters. Caution must be used, however, since there is some subjectivity to the calculations. The method tends to be very consistent when applied by a single person, but there can be significant variation from person to person. A software-based implementation of this method developed by Markus Gloeckler was used for extracting all of the diode parameters used in this work.

2.3.3 Quantum Efficiency

Quantum efficiency (QE) is a measure of the ratio of the number of electrons collected out of the cell at short circuit to the number of photons incident on the cell. It is generally measured as a function of wavelength. Fig. 2.6 shows a typical QE response for a CdTe cell. At long wavelengths, the QE falls off as the absorption is reduced at the band gap of the absorber layer. Across the center region, QE is often relatively flat, with losses including reflection and absorption from the substrate. At short wavelengths, QE response is dominated by CdS absorption. The band gap of CdS is around 510 nm, so absorption increases strongly below this point. Due to short minority carrier lifetime in CdS, most of the generated carriers recombine before they can be collected from the cell.

When measured at short-circuit conditions, the QE can be integrated to calculate the short-circuit current density:

$$J_{sc} = q \int QE(\lambda) N_{ph}(\lambda) d\lambda \quad (2.5)$$

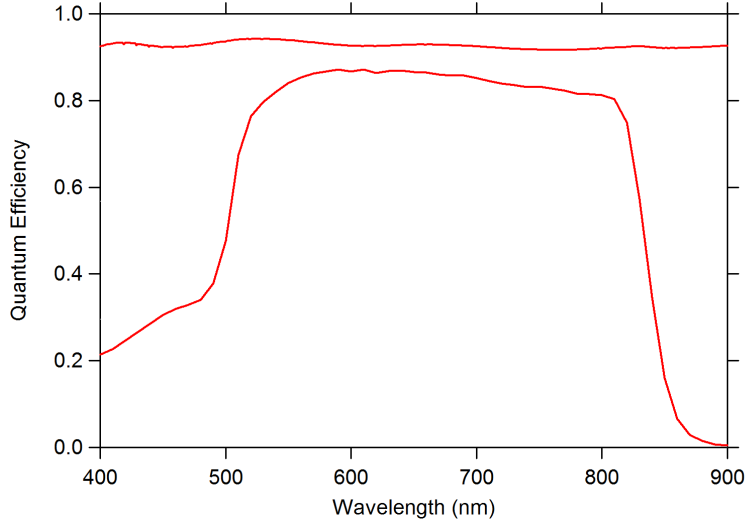


Figure 2.6: Quantum efficiency of a typical CdTe cell. The upper curve is reflection loss measured down from 1, and the lower curve is QE measured up from 0.

where q is the fundamental charge and N_{ph} is the number of photons at each wavelength in the solar spectrum. This provides a second way of calculating J_{sc} , which can be used as a cross-comparison with the value obtained from J-V measurements. A particular loss mechanism can replace QE in the equation to calculate the current lost due to that mechanism.

Light for the CSU QE setup is provided by a halogen bulb. The light passes through an Acton SpectraPro 150 monochromator, and the monochromatic light is chopped by an SRS SR540 chopper and focused onto the cell. The current output from the cell is amplified by a SRS SR570 preamplifier which can apply a voltage bias if desired, though the cell is usually measured at short circuit conditions. The amplified signal is measured by an SRS SR810 lock-in amplifier which is locked to the chopper frequency. A 620 nm long-pass filter is inserted into the beam after the sweep passes 650 nm to remove second order monochromator peaks. A light bias can be applied using a krypton bulb powered by a DC power supply.

2.3.4 Capacitance

Capacitance measurements are a tool for exploring the electronic properties of a cell. The two edges of the depletion region act as a parallel-plate capacitor with a dielectric in the middle. Capacitance is measured by applying a small AC bias. Capacitance can then be measured as the frequency of the AC bias is varied (capacitance-frequency, or C-f) or as a varying DC bias is applied (capacitance-voltage, or C-V).

Capacitance-frequency measurements can provide information about trap states, especially when temperature is varied. However, for CdTe cells, the trap states usually do not appear in C-f measurements. The primary use of C-f for CdTe cells at CSU has been to determine a frequency where capacitance is not changing with frequency. This is the frequency which is then used for measuring C-V.

Calculations can be done using the capacitance-voltage results based on equations for the capacitance of a parallel-plate capacitor

$$C = \varepsilon A/W \quad \text{or} \quad W = \varepsilon A/C \quad (2.6)$$

where ε is the dielectric constant, A is the area of the cell, and W the depletion width; and the capacitance of a one-sided junction

$$C^2 = \frac{A^2 q \varepsilon p}{2(V_{bi} - V)} \quad (2.7)$$

where V_{bi} is the built-in voltage and p is the position-dependent hole density. The second equation assumes a one-sided junction, where the depletion region is entirely within the CdTe. For CdTe, the value $\varepsilon = 9.4\varepsilon_0$ is used [7]. Since the value for V_{bi} is generally unknown, the discrete derivative is taken and the equation solved for p ,

$$p = \frac{C^3 \Delta V}{q \varepsilon A^2 \Delta C} \quad (2.8)$$

Equations 2.6 and 2.8 have been solved for W and p , respectively, and the result can be graphed parametrically to produce a graph of hole-density as a function of distance into the CdTe layer.

The capacitance measurement setup at CSU relies on an HP4192A impedance analyzer. The impedance analyzer provides both the AC and DC bias and can vary the frequency. The DC bias is checked using an HP33401A digital multimeter. A relay switch removes the multimeter from the circuit while capacitance measurements are being made. The phase angle of the complex impedance is also measured, since the accuracy drops significantly when the phase angle is below 20° .

2.3.5 Uniformity Measurements

Light-Beam-Induced Current

Light-beam-induced current (LBIC) is a measure of local quantum efficiency. A current measurement is performed as the cell is rastered under a monochromatic light spot. The intensity is also monitored in order to calculate QE. A point-by-point map of QE can be produced from this data. The system and procedure will be fully described in Ch. 5.

Electroluminescence

Electroluminescence (EL) is a measure of the light produced by an electrically biased cell. The cell is forward biased, so that electrically-excited carriers can recombine. The emitted light is then imaged.

The system at CSU uses an Apogee Alta 8300 camera with a Zeiss 50 mm macro lens and extension tubes for imaging. The CCD is cooled to -25°C to reduce dark noise. The camera is attached to a lab jack for fine focusing. The camera system is in a darkened enclosure to eliminate background light. Bias is applied to the cell using a DC power supply and measured using an HP33401A digital multimeter. Images are generally taken with 40 mA/cm^2 forward current and a 100 s exposure time. The images are generally plotted on a logarithmic z-scale, since the logarithm of the EL intensity has been found to be proportional to the cell's V_{oc} [9].

Chapter 3

EFFICIENCY ANALYSIS AND LIMITS

Although photo-sensitive devices had been made earlier, the first modern solar cell was created at Bell Labs in 1954, and had an efficiency of 6% [10]. The present record for single junction solar cells is 28.8% [6]. In between these two points, solar cell efficiencies have continuously moved upwards [11]. The single junction GaAs cell is nearing the theoretical efficiency limit. However, many other technologies lag far behind this record cell. In order to continue moving to higher efficiencies, it is necessary to understand the loss mechanisms which are reducing efficiency and the relative importance of these different loss mechanisms. To that end, this chapter presents a framework for breaking a cell's total efficiency into categories and analytically quantifying the loss mechanisms present in the cell.

3.1 Breakdown of Efficiency

A general expression for a solar cell's electrical power generation is broken down into three performance parameters, short-circuit current (J_{sc}), open-circuit voltage (V_{oc}), and fill factor (FF). When divided by input power density, this produces the standard definition of efficiency:

$$\eta = \frac{P_{electrical}}{P_{light}} = \frac{J_{sc} \cdot V_{oc} \cdot FF}{P_{light}} \quad (3.1)$$

which is usually measured under standardized conditions of 25°C, 100 mW/cm² irradiance, and AM1.5 spectrum (IEC 60904-3, Ed. 2, 2008 or ASTM G173-03). We can define the input power spectrum as $P(\lambda)$, so that the total input power density is $\int_0^\infty P(\lambda)d\lambda$.

We can introduce relevant ideal values by inserting ratios of identical terms and rearranging. By this means, we insert the ideal values for $J_{sc,ideal}$, $V_{oc,ideal}$, and FF_{ideal} , where these terms will be defined in Section 3.1.1. This produces the equation

$$\eta = \frac{J_{sc,ideal} \cdot V_{oc,ideal} \cdot FF_{ideal}}{\int_0^\infty P(\lambda)d\lambda} \cdot \frac{J_{sc}}{J_{sc,ideal}} \cdot \left(\frac{V_{oc}}{V_{oc,ideal}} \frac{FF}{FF_{ideal}} \right) \quad (3.2)$$

which has four factors which multiply to produce the total efficiency. Each of these four factors will be explored in Sections 3.2 through 3.4, respectively. Equation 3.2 can be grouped into three efficiency factors. The first factor is described as the solar spectrum efficiency, the second as the optical efficiency, and the final two as the electronic efficiency. We can thus rewrite the equation as

$$\eta = \eta_{\text{SolarSpectrum}} \cdot \eta_{\text{Optical}} \cdot \eta_{\text{Electronic}} \quad (3.3)$$

The separation of η_{Optical} from $\eta_{\text{Electronic}}$ requires a voltage-independent collection. This three-category analysis of efficiency will be explored for record cells in Section 3.1.2.

3.1.1 Ideal Efficiency Parameters

The above ideal values must be defined. The ideal value of the short-circuit current density can be obtained by integrating the solar spectrum for all wavelengths below the band gap. It is thus defined as

$$J_{sc,\text{ideal}} = q \int_0^{\lambda_g} N_{ph}(\lambda) d\lambda \quad (3.4)$$

where q is the fundamental charge, and N_{ph} is the number of photons at each wavelength, which can be calculated by dividing the power spectrum by the energy per photon, $N_{ph}(\lambda) = \lambda P(\lambda)/hc$. In this definition each photon with energy greater than the band gap creates one electron-hole pair of charge q which is collected out of the cell. This value is idealized in that the band gap is assumed to produce a sharp absorption edge, and that complete photon absorption and resulting collection of photo-generated carriers take place.

The ideal open-circuit voltage begins with rearranging the standard diode equation (ignoring parasitic resistances in the idealized case) at zero current to solve for V_{oc} :

$$V_{oc,\text{ideal}} = \frac{kT}{q} \ln \left(\frac{J_{sc,\text{ideal}}}{J_{0,\text{ideal}}} + 1 \right) \quad (3.5)$$

where k is the Boltzmann constant, T is the temperature, and $J_{sc,\text{ideal}}$ is the ideal value from Eq. 3.4. The ideal value for J_0 , the saturation current, can be determined thermodynamically, by applying the principle of detailed balance. The cell is treated as a black body, and emits

radiation as such by the recombination of electron-hole pairs. The saturation current is then connected to the black-body spectrum by the equation

$$J_{0_ideal} = q \int_0^{\infty} \phi_{bb}(\lambda) a(\lambda) d\lambda \quad (3.6)$$

where $a(\lambda)$ is the absorption of the cell, and ϕ_{bb} is the black-body spectrum, given by

$$\phi_{bb}(\lambda) = \frac{2\pi}{h\lambda^2} e^{-\frac{hc}{\lambda kT}} \quad (3.7)$$

where h is the Planck constant. If the absorption is assumed to be a step function above the band-gap energy, this reduces to

$$J_{0_ideal} = q \int_0^{\lambda_g} \frac{2\pi}{h\lambda^2} e^{-\frac{hc}{\lambda kT}} d\lambda \quad (3.8)$$

This can be analytically integrated to

$$J_{0_ideal} = \frac{2\pi q}{h^3 c^2} \frac{(E_g/kT)^2 + 2E_g/kT + 2}{e^{E_g/kT}} \quad (3.9)$$

where the energy of the band gap $E_g = hc/\lambda_g$ has been substituted for the wavelength of the band gap.

Equations 3.4 and 3.8 can be substituted into Eq. 3.5 to produce the ideal open-circuit voltage:

$$V_{oc_ideal} = \frac{kT}{q} \ln \left(\frac{\int_0^{\lambda_g} N_{ph}(\lambda) d\lambda}{\int_0^{\lambda_g} \frac{2\pi}{h\lambda^2} e^{-\frac{hc}{\lambda kT}} d\lambda} + 1 \right) \quad (3.10)$$

To derive an equation for the fill factor, the maximum-power voltage must be calculated. In principle, this can be solved by maximizing the power, which occurs when the equation

$$\frac{d}{dV}(JV) = 0 \quad (3.11)$$

is satisfied. Unfortunately, this leads to the transcendental equation

$$e^{\frac{qV_{max}}{kT}} = \left(1 + \frac{J_L}{J_0} \right) \left(1 + \frac{qV_{max}}{kT} \right)^{-1} \quad (3.12)$$

which cannot be solved analytically. A numerical mapping approach was developed by Shockley and Queisser [12], and Green later developed a function which fits the numerical solution [13] and can be expressed as a function of only the open-circuit voltage

$$FF = \frac{v_{oc} - \ln(v_{oc} + 0.72)}{v_{oc} + 1} \quad (3.13)$$

where

$$v_{oc} = qV_{oc}/AkT \quad (3.14)$$

This expression is accurate to 4 significant digits for $v_{oc} > 10$. The ideal value of fill factor is obtained from this equation by setting V_{oc} to the ideal value obtained from Eq. 3.10 and $A = 1$. A limiting maximum for FF for actual values of V_{oc} and A can be obtained by using these values in this equation, as will be discussed in Section 3.4.

3.1.2 Analysis of Record Cells

The three-category analysis can be applied to the record cells of each technology, as shown in Fig. 3.1. The J_{sc} , V_{oc} , FF , and η values are drawn from the efficiency tables in Ref. [6], except the CdTe [14] [15] and Si-HIT [16]. Apart from the four cell parameters, band gap is the only other factor necessary for this general analysis. In all cases, the band gap was chosen at the 20% point of the quantum efficiency curves, if available, or as a standard value of band gap for the material. The record cells are arranged from highest to lowest total efficiency. Note that throughout this section, the term “technology” refers to a specific absorber material. Within each technology, there can also be significant differences in performance because of processing conditions.

Despite the fact that the total efficiencies spread a range from 10 to nearly 30%, there are several clear trends in the results. There is little variation between the solar spectrum efficiencies between the cells, since the peak is broad, as will be seen in section 3.2. There is a general trend towards higher optical efficiency with higher total efficiency, though there are obvious outliers. CdTe has a higher optical efficiency than its nearest efficiency neighbors, possibly because this has been the easiest parameter for commercial companies to optimize. GaAs, despite a very high overall efficiency, has a slightly lower optical efficiency than Si-HIT, c-Si’.

The trend between electronic efficiency and total efficiency is very strong, suggesting that this is the dominant parameter in determining overall efficiency. Here, GaAs stands out with electronic efficiency nearly 15% above its nearest competitor. CZTSS stands out as the only

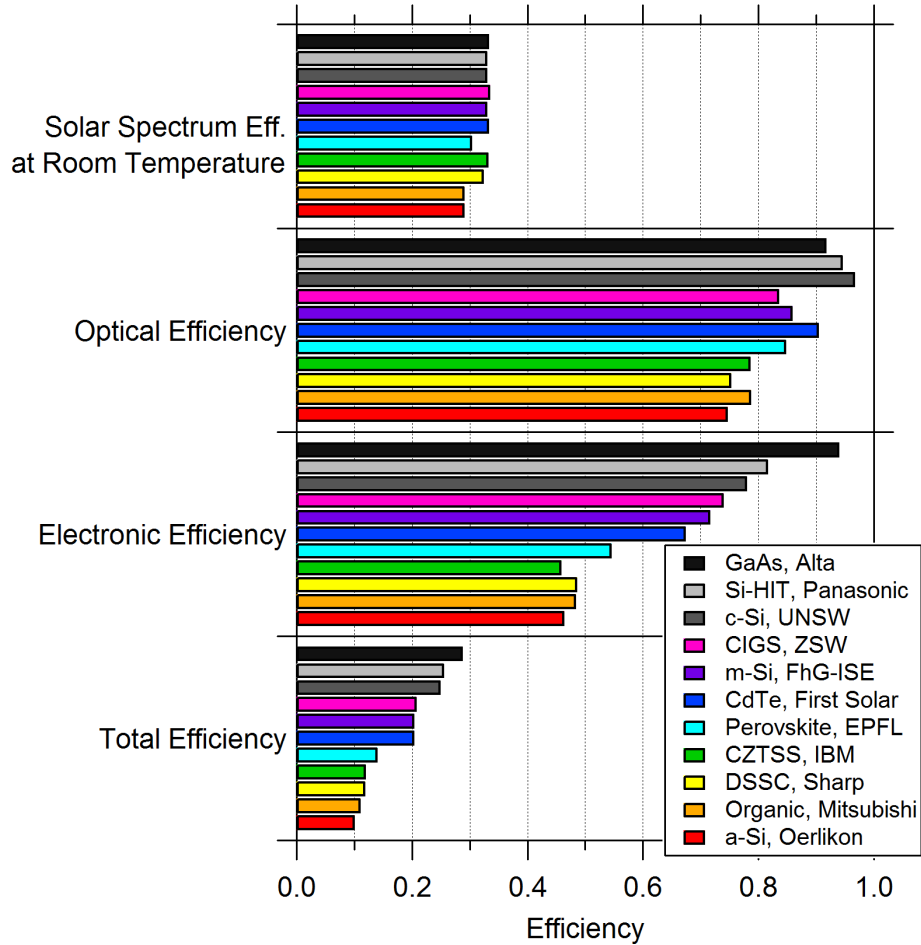


Figure 3.1: Breakdown into three efficiency categories for record cells.

technology that does not fit the trend. A good optical efficiency of CZTSS, combined with a better solar spectrum efficiency than its nearest neighbors, likely compensates for the poorer electronic efficiency.

It is worth noting that this work was based on the highest efficiency values published with complete cell parameters at the time the work was done. As new records continue to be set, this work will quickly become out of date quantitatively, and eventually qualitatively. For instance, a new perovskite record of 16.2% has already been announced by KRICT, although the full cell parameters necessary for this analysis have not yet been published.

Although this approach is powerful because it is technology- and band-gap-independent, it also has power when applied to a single band gap or technology, such as CdTe. Fig. 3.2

compares the categorical efficiencies of several CdTe cells. A GaAs cell is included for comparison purposes, because it is of similar band gap and is the leading single-junction cell. The CSU cells are a standard process (baseline), a replacement of the CdS with Cd(S,O), and with an additional CdMgTe electron reflector, respectively. These types of cells will be described more fully in Chapter 4. The First Solar cell is the present CdTe record [14], and the GE cell is a previous CdTe record [6].

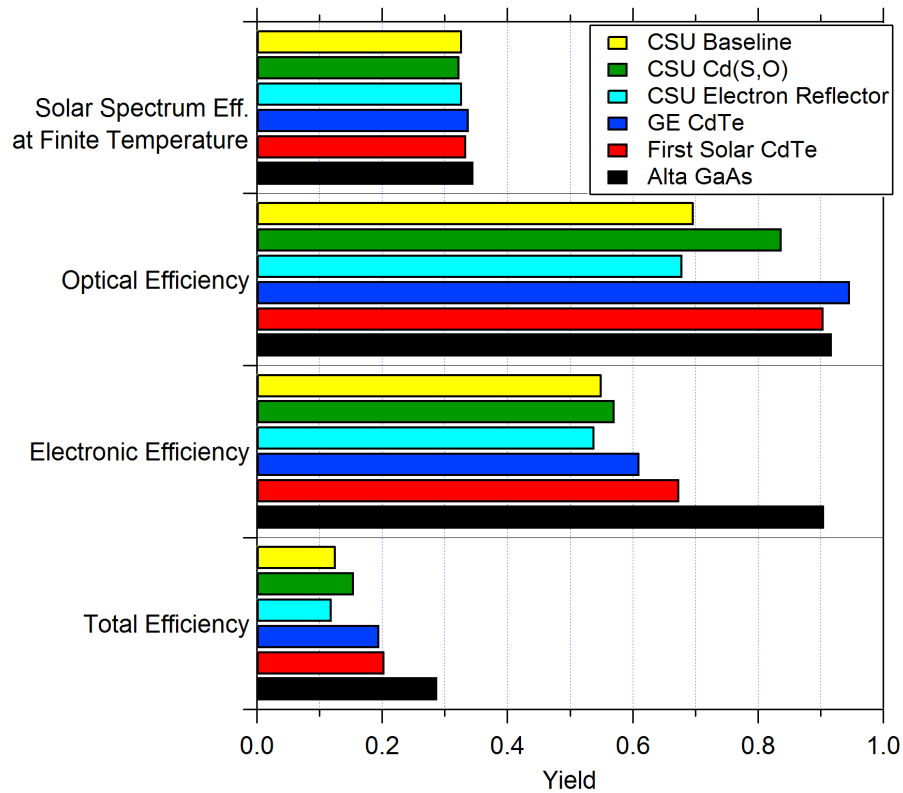


Figure 3.2: Breakdown of several CdTe cells and one GaAs cell into three efficiency categories.

Since all the cells in Fig. 3.2 are of similar band gaps, the first category shows very little difference between the cells. The optical efficiency is what sets the low-performing CdTe apart from the high-performing CdTe. The Cd(S,O) is clearly seen as a major step in improving CSU cells. GaAs is separated from CdTe on the basis of its electronic efficiency, since the optical efficiency is comparable to the record CdTe cells. The electron reflector

has the potential to significantly improve the electronic efficiency of CdTe cells fabricated by CSU and others.

3.2 Solar Spectrum Efficiency Limit

The efficiency of a single-junction solar cell is fundamentally limited because of the broad spectrum of solar light, in addition to the finite temperature at which cells operate. For a standard spectrum and cell temperature, this limiting efficiency depends only on the band gap of the cell, and is commonly called the Shockley-Queisser Limit, after the authors of the original theoretical work [12]. This is all encompassed by the first factor of Eq. 3.2. We can expand this equation by inserting factors of one into this equation, as was done before, and including the definition of the ideal $J_{sc,ideal}$ from Eq. 3.4

$$\eta_{\text{SolarSpectrum}} = \frac{\int_0^{\lambda_g} P(\lambda) d\lambda}{\int_0^{\infty} P(\lambda) d\lambda} \cdot \frac{E_g \int_0^{\lambda_g} N_{ph}(\lambda) d\lambda}{\int_0^{\lambda_g} P(\lambda) d\lambda} \cdot \frac{qV_{oc,ideal}}{E_g} \cdot \frac{FF_{ideal}}{1} \quad (3.15)$$

These factors are depicted in Fig 3.3. The first factor (red line) is due to non-absorption of photons with energy greater than the band gap. The second factor (purple line) is the losses due to the thermalization of electron-hole pairs generated by photons with energy higher than the band gap. Although the electron-hole pairs initially have energy greater than the band gap, this energy is very quickly lost through thermal processes, so that the pair ends with energy equal to the band gap. The thick green line is the product of these first two factors, and is the limiting efficiency if the cell temperature was 0 K. It has a maximum of 49% at a band gap of 1.12 eV.

At finite temperatures, the ideal open-circuit voltage is below the band gap, which produces the pink line when multiplied by the first two factors. The ideal fill factor is also less than unity at finite temperatures. Inclusion of the temperature factors produces the thick black line, which is the limiting efficiency for a single-junction cell at 25°C under AM1.5 illumination. The maximum efficiency is 33.7% at 1.34 eV, though there is another near-maximum around 1.1 eV, and the peak is fairly broad, staying above 30% from 0.9 to 1.6 eV. These results agree well with other published versions of this calculation, see for example

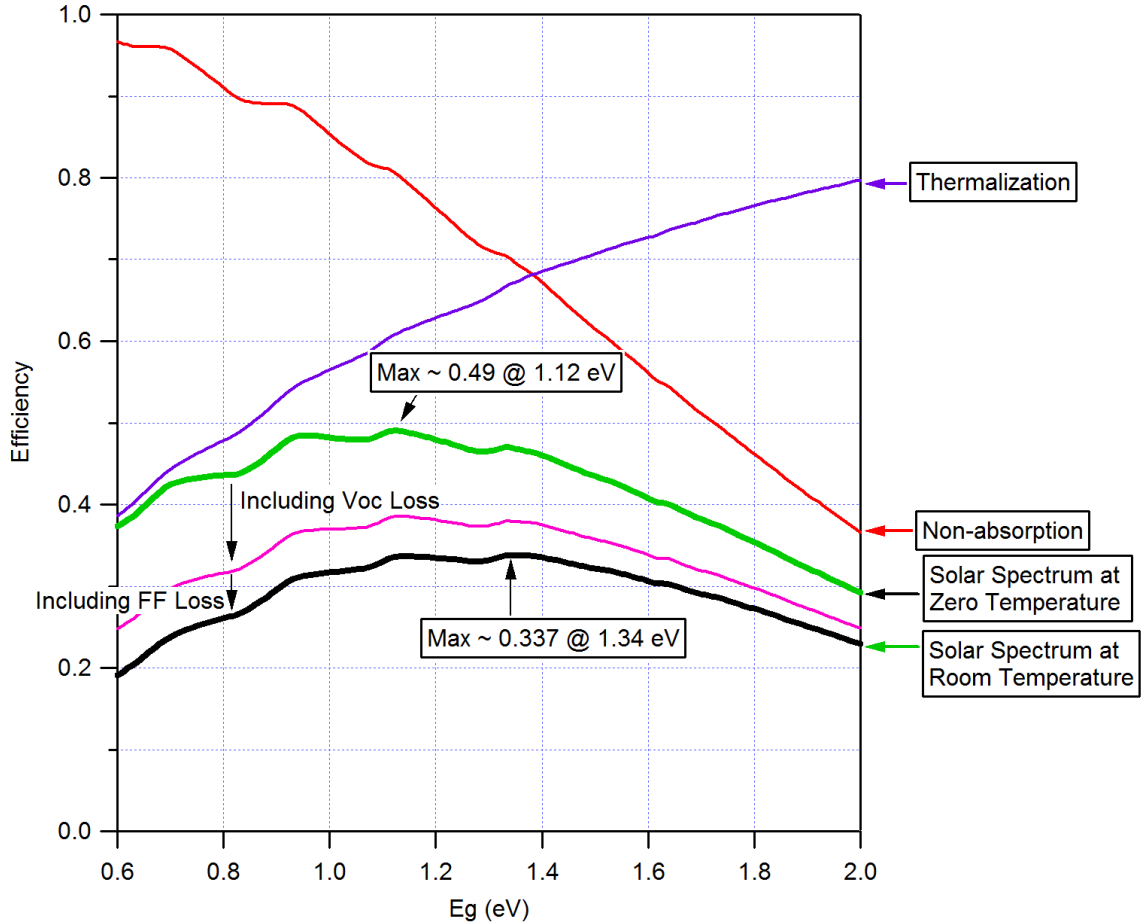


Figure 3.3: Maximum efficiency as a function of band gap due to the broad solar spectrum and finite cell temperature.

[17] and [18]. The results are not, however, exactly comparable to Shockley and Quieser’s original results, since they assumed a 6000 K black-body input spectrum [12], rather than the AM1.5 spectrum used here.

The limiting efficiency can also be described in terms of ideal values of J_{sc} , V_{oc} , and FF , as shown in Fig. 3.4. These values are calculated from Eqs. 3.4, 3.10, and 3.13, respectively. The J_{sc} values in this figure (blue line) decrease with increasing band gap, because fewer photons are absorbed at larger band gaps. The flatter regions in J_{sc} are due to absorption gaps in the solar spectrum, which means that few photons contribute to the current in those ranges. The V_{oc} values (red line), by contrast, increase smoothly with increasing band gap,

because of improved collection of the energy of each absorbed photon. Since the ideal FF (green line) depends only on V_{oc} , the fill factor follows the trend of V_{oc} . The limiting efficiency can be calculated by multiplying the three together and dividing by the input solar power, in this case 100 mW/cm^2 , as shown by the black line, which matches the black line in Fig. 3.3.

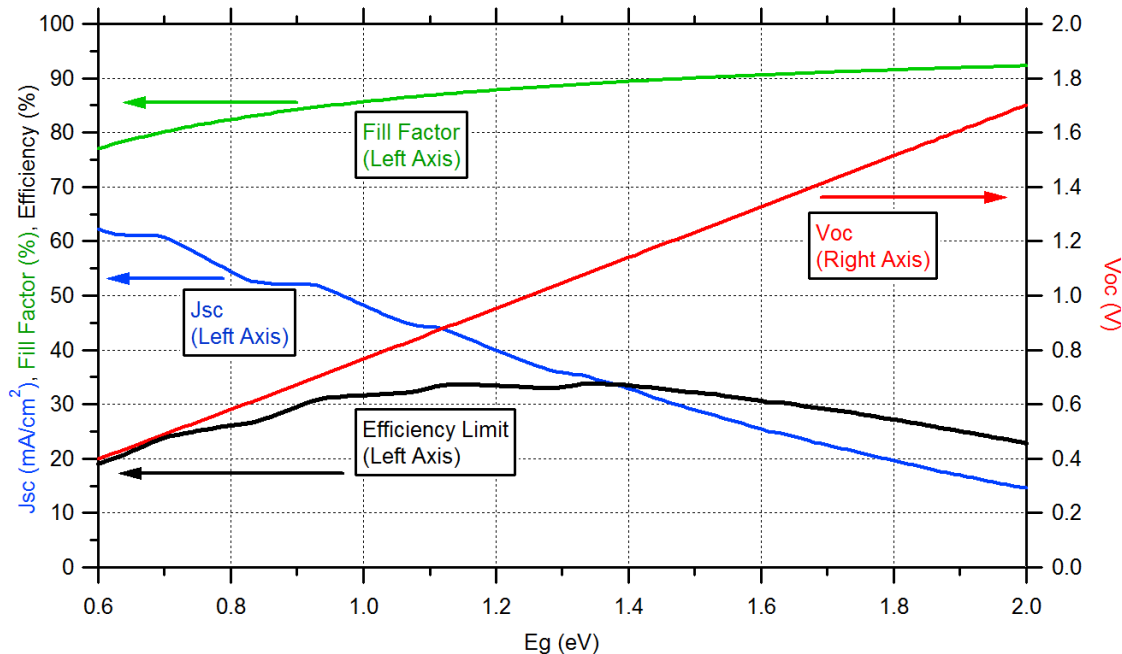


Figure 3.4: Ideal values for J_{sc} , V_{oc} , FF , and η with varying E_g .

3.3 Short-Circuit Current Density Analysis

The losses in J_{sc} can be accounted for through a straightforward analysis of quantum efficiency and optical measurements. This accounting is depicted in Fig. 3.5 as additions to a quantum efficiency graph for a typical CSU CdTe cell. The colored sections are additive up to 100%, so that the entire set of incident photons is counted. The red block is the actual collected current from the cell. The white block to the right is sub-band-gap light which is not expected to be collected. Everything else is considered a loss.

Since the cell is made in a superstrate configuration, there is glass and TCO between the incident light and the cell. Some fraction, typically 5-10%, is reflected from the front

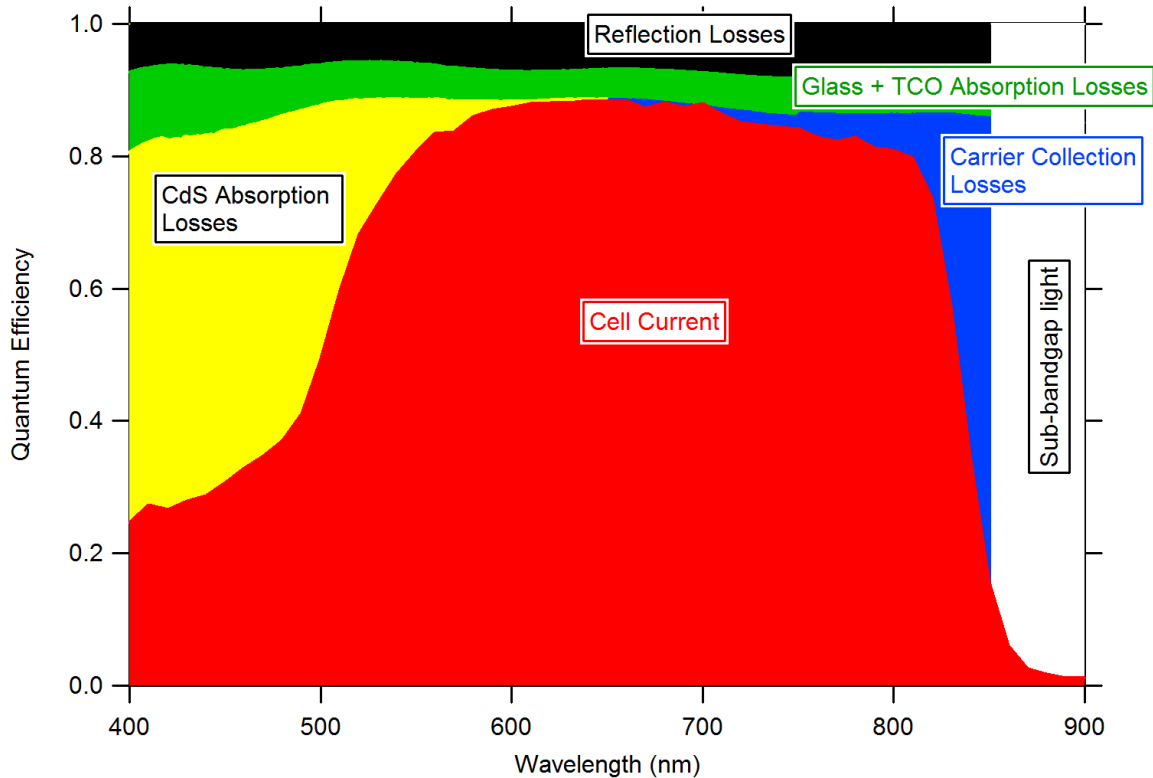


Figure 3.5: Accounting of losses in short-circuit current due to both optical and electronic means in a typical CSU CdTe cell.

of the cell, which is the black section. This measurement was made on a finished cell, since deposition of semiconductor material affects the reflection by modifying the indices of refraction at the interfaces. Generally, there is also 5-10% of the light absorbed by the glass and TCO, which is the green section. This value was calculated by subtracting measured reflection and transmission from 100% for a bare substrate. When TCO-free glass samples are available, the glass and TCO absorption losses can be further separated.

The light which penetrates the substrate is absorbed by the cell, as long as the cell is sufficiently thick. The CdS window layer absorbs a significant fraction of the light with energy above the 510 nm CdS band gap. Due to the low minority-carrier lifetime in CdS, most of the generated electron-hole pairs are not collected, which are the yellow losses. There is also some loss beyond the CdS band gap due to alloying of the CdS and CdTe layers. The blue losses are due to electron-hole pairs which are generated by photons that penetrate

deeply into the CdTe absorber and are not collected. In thin cells, these regions will also include losses due to transmission of longer-wavelength photons through the absorber.

The QE and each optical loss as a function of wavelength can be integrated with the solar spectrum to produce associated current density

$$J_{f(\lambda)} = q \int_0^{\infty} f(\lambda) N_{ph}(\lambda) d\lambda \quad (3.16)$$

where $f(\lambda)$ can be QE, reflection, absorption, or any other loss. Table 3.1 shows the integrated current densities and equivalent current density losses from Fig. 3.5. Collectively, the multiple loss mechanisms remove a significant amount of current from the cell. The largest of these, CdS absorption, can be reduced or removed using oxygenated CdS, as will be described in Section 4.3.4. Reflection losses can be reduced through antireflective coatings. Absorption losses can be reduced by thinning the glass or TCO, or making either more transparent. Although the collection losses here are relatively small, they can be symptomatic of larger electronic issues.

Table 3.1: Current density losses in a typical CSU CdTe cell.

Loss Mechanism	Current Density (mA/cm ²)
Reflection	2.1
Glass + TCO Absorption	1.7
CdS Absorption	3.4
Collection Loss	0.9
Cell Current	21.0
Total Current	29.1

3.4 Fill Factor Analysis

An expression for $FF(v_{oc})$ was already presented in Eq. 3.13. The normalized open-circuit voltage, v_{oc} , is a function of both V_{oc} and the diode ideality factor, A . Although these two factors limit the fill factor for high-efficiency devices, other factors can play a role in determining the fill factor for lower-performing devices. These other factors include parasitic resistances (series and shunt) and distortions to the regular diode shape, often caused by barriers [19] [20] [21].

The fill factor term which appears in Eq 3.2 is normalized to the ideal value. We can expand this term to include the limitation based on non-ideal parameters:

$$\frac{FF}{FF_{ideal}} = \frac{FF_{V_{oc},A}}{FF_{ideal}} \cdot FF_{series} \cdot FF_{shunt} \cdot FF_{other} \quad (3.17)$$

where $FF_{V_{oc},A}$ is calculated from Eq. 3.13 using real values for V_{oc} and A . Approximate analytical expressions for the effect of series and shunt resistance on fill factor were developed by Green [13]. For series resistance, the expression is

$$FF_{series} \approx 1 - \frac{R_s}{R_{ch}} \quad (3.18)$$

where

$$R_{ch} = \frac{V_{oc}}{J_{sc}} \quad (3.19)$$

is the characteristic resistance of the cell. In order to have little impact on fill factor, the series resistance must be much smaller than the characteristic resistance, and the shunt resistance must be much larger than the characteristic resistance. The expression for shunt resistance is

$$FF_{shunt} \approx 1 - \frac{R_{ch}}{r_{sh}} \quad (3.20)$$

The FF_{other} term in 3.17 is defined to catch all the fill factor losses which are not encompassed by the other terms. It is a derived value, calculated such that the actual fill factor value is correct. To avoid coupling between terms, this analysis is best applied to high-fill-factor cells.

The first factor in Eq 3.17 depends on two variables, open-circuit voltage and ideality factor. It can therefore be expanded to separate out the changes in fill factor due to the changes in these two variables. Similar to previous expressions, this is done by introducing factors of one which are ratios of $FF(V, A)$ where $V = V_{ideal}$ or $V = V_{oc}$ and A is either 1 or its actual value. The full expansion is

$$\frac{FF_{V_{oc},A}}{FF_{ideal}} = \frac{FF_{V_{oc},A=1}}{FF_{ideal}} \cdot \frac{FF_{V_{oc,ideal},A}}{FF_{V_{oc},A=1}} \cdot \frac{FF_{V_{oc},A}}{FF_{V_{oc,ideal},A}} \quad (3.21)$$

Although this expression is mathematically valid, there is not an unambiguous physical meaning to all the factors. The first factor is due to reductions in V_{oc} which are independent of A . This could be due to a reduced value of E_a , as described in Section 3.5. The second and third factors are the reductions in fill factor due to increased A in addition to the losses due to reduced V_{oc} .

The fill-factor analysis can be performed on several record cells for which J-V curves are available. Table 3.2 shows analysis for the 28.8% Alta GaAs cell, the 20.3% ZSW CIGS cell [6], the 24.7% Si-HIT cell [22] and the 17.3% First Solar CdTe cell [23]. From this table, we can compare the fill factor losses between the single-crystal cells (GaAs and Si) and the polycrystalline cells (CIGS and CdTe). The single-crystal cells generally have slightly smaller losses in all of the individual categories, resulting in a higher overall fill factor. This analysis allows for all the losses to be directly accounted for in the HIT and CdTe cells, since the “other” factor is 1 in both cases. The HIT cell also has effectively zero losses due to resistance issues; hence, its fill factor is reduced solely due to reduced V_{oc} and increased A .

It should be noted that the analysis of fill factor requires the shunt and series resistances and the diode ideality factor to be accurately calculated. This is done by processing published J-V data using the CurVA analysis described in Section 2.3.2. However, there are uncertainties inherent in this technique. For instance, apparent shunt resistances for low-lifetime cells may actually be caused by voltage-dependent collection, rather than a true resistance. Likewise, the ideality factor may not be constant with voltage. Because of this, standards has been adopted. The shunt resistance is calculated from the light curve near

Table 3.2: Fill factor losses in record cells. All values are ± 0.005 , except actual fill factor values are as published. The first three rows multiply to $FF_{V_{oc},A}/FF_{ideal}$.

Loss Mechanism	GaAs	Si HIT	CIGS	CdTe
$FF_{V_{oc},A=1}/FF_{ideal}$	0.994	0.983	0.974	0.962
$FF_{V_{oc,ideal},A}/FF_{V_{oc},A=1}$	0.988	0.992	0.987	0.978
$FF_{V_{oc},A}/FF_{V_{oc,ideal},A}$	0.993	0.980	0.967	0.941
FF_{series}	0.992	1.000	0.989	0.958
FF_{shunt}	1.000	0.999	0.976	0.987
FF_{other}	0.995	1.000	0.986	1.000
FF	0.865	0.832	0.775	0.756
FF_{ideal}	0.898	0.869	0.876	0.901

zero bias. The ideality factor, series resistance and saturation current are assumed to be constant and are calculated in the region between the maximum-power point and open-circuit voltage. The ideality factor is calculated two different ways, and an average value is used, assuming they are in reasonable agreement. These standards all work well for reasonably well-behaved cells, which includes most record efficiency cells.

3.5 Open-Circuit Voltage Analysis

It is difficult to analyze open circuit voltage from a perspective which is physically meaningful, analytically tractable, and based on direct measurements. Therefore, this section will explore the methods presented by other authors, some of the physical bases for V_{oc} losses, and some measurements which can provide insight.

An approach used by other authors is to focus on the difference between the band gap, E_g and the actual V_{oc} . This is the approach used by Polman and Atwater [24] and Hirst and

Ekins-Daukes [25]. They derive similar equations; the one from Hirst and Ekins-Daukes is

$$qV_{oc} \approx E_g \left(1 - \frac{T}{T_{sun}} \right) - kT \ln \left(\frac{\Omega_{emit}}{\Omega_{abs}} \right) + kT \ln \left(\frac{\gamma(E_g, T_s)}{\gamma(E_g, T)} \right) \quad (3.22)$$

with the approximate sign due to taking the Boltzman approximation, and where

$$\gamma(E, T) = \frac{2kT}{c^2 h^3} (E^2 + 2kTE + 2k^2 T^2) \quad (3.23)$$

In this equation, Ω_{abs} is the solid angle from which light is absorbed and Ω_{emit} is the angle over which light is emitted from the cell, up to 4π . The first term is called the Carnot factor, has a value approximately 95% of the band gap, and is due to the Carnot efficiency limit for two extracting work from two reservoirs at different temperatures. The second term is the Boltzman factor, which is associated with the increase in entropy due to absorption and unconstrained re-emission of light from the cell. For the worst case scenario of absorption from the sun and a full 4π re-emission, this factor is about 310 mV at room temperature. This loss can be reduced by restriction of the angle of emission [26]. The third term is due to an increase in the free energy per carrier due to transfer of entropy between the lattice and carriers. Polman and Atwater derive a similar equation, though theirs is more focused on non-ideal situations. Note that this analysis also uses a 6000 K black-body spectrum, rather than the AM1.5 spectrum.

A more interesting approach, from a practical device analysis point of view, is to focus on the losses below the thermodynamically-limited open-circuit voltage. One approach is presented by Rau [27] and Miller, Yablonovitch, and Kurtz [26]. They present the equation

$$V_{oc} = V_{oc,ideal} - \frac{kT}{q} |\ln(\eta_{ext})| \quad (3.24)$$

where $V_{oc,ideal}$ is calculated from Eq. 3.10 and η_{ext} is the fraction of recombination which leads to light radiation from the cell. It can also be called EQE_{LED} , which is the external quantum efficiency of the cell when treated as a light-emitting diode. This identifies the source of all voltage loss as nonradiative recombination. As a practical matter, this should be treated as a definition or calculation method for the amount of nonradiative recombination, rather than a means for identifying the sources of recombination loss. It is also worth noting that

recombination has a much larger effect on V_{oc} than J_{sc} , since the built-in electric field under short-circuit conditions quickly separates electrons and holes.

An alternative limiting V_{oc} was developed by Toberer *et al.*, and is called the detailed balance voltage [28]. This voltage is calculated by assuming the external quantum efficiency (EQE) is a good approximation for the absorption of a cell. The detailed-balance voltage is thus defined by

$$V_{db} = \frac{kT}{q} \ln \left(\frac{\int_0^\infty EQE(\lambda) N_{ph}(\lambda) d\lambda}{\int_0^\infty EQE(\lambda) \phi_{bb}(\lambda) d\lambda} + 1 \right) \quad (3.25)$$

This expression incorporates many of the losses in the quantum efficiency into the voltage. It is, in effect, a limiting V_{oc} for a given EQE. It does not, however, provide any insight into the reductions in V_{oc} below this limiting value.

Another approach is to use simulations to calculate the losses due to various mechanisms specific to a particular material, as was done by Swanson for the case of crystalline silicon (c-Si) [29]. These losses are re-created in Fig. 3.6. Swanson's analysis treated all the losses purely as efficiency losses, so I have added the breakdown into which parameter is affected. The majority of losses are clearly in V_{oc} , with J_{sc} and fill factor losses less than 3% total. The largest source of losses in c-Si is clearly due to Auger recombination, which primarily reduces open-circuit voltage. This analysis is very useful, since it provides clear detail of what the limiting loss mechanisms are, apart from 1% which is still unaccounted for in this analysis. Unfortunately, it has the disadvantage of being extremely technology specific. It also requires reliable values for several parameters such as mobility, saturation current densities of the contacts, and several others. Although it may be possible to measure or calculate these specific values for semi-idealized crystalline devices, it can be somewhat problematic for less ideal polycrystalline materials. Ultimately, the goal is separating the strength of different recombination mechanisms, including interfaces, defects, and the Auger process.

Some insight into the behavior of V_{oc} can also be gained from expressing the saturation current density in the same way as Scheer [30]:

$$J_0 = J_{00} e^{-\frac{E_g}{AkT}} \quad (3.26)$$

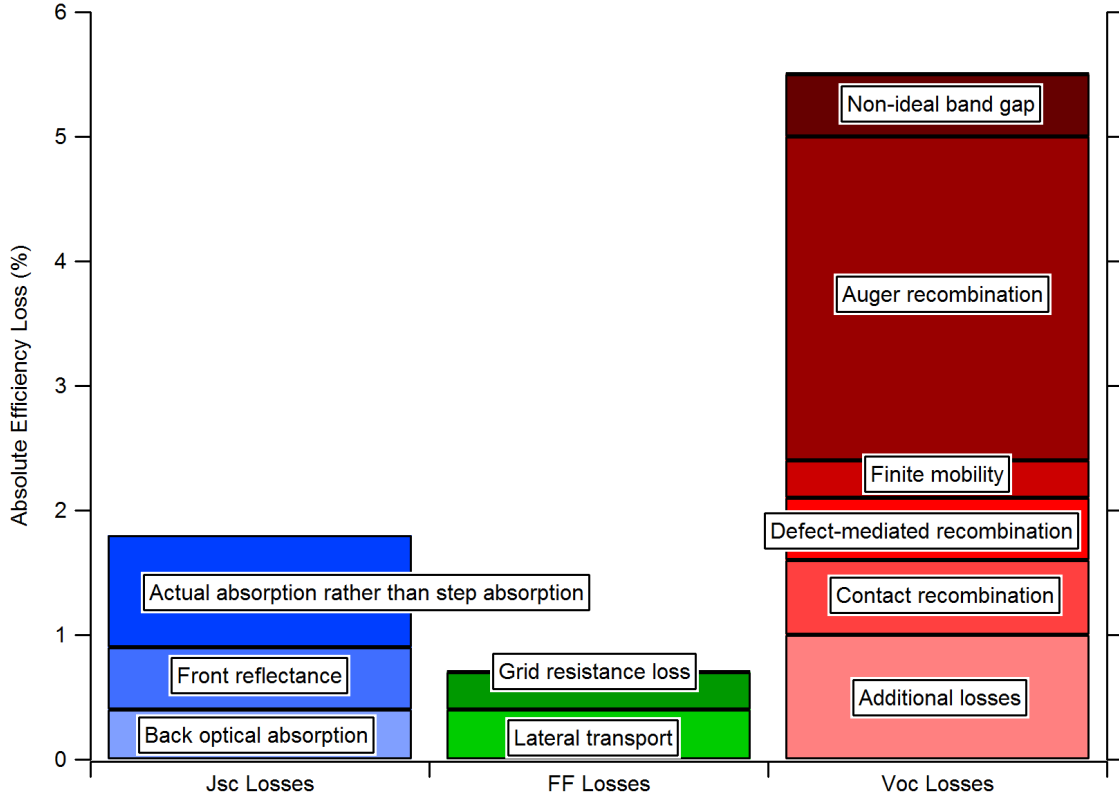


Figure 3.6: Accounting of losses in crystalline silicon using Swanson’s modeled values.

where E_a is the activation energy of J_0 . This can be inserted into the diode equation (neglecting the +1)

$$J = J_{00}e^{-\frac{qV-E_a}{AkT}} - J_{sc} \quad (3.27)$$

and solved for V_{oc} by setting $J = 0$

$$V_{oc} = \frac{E_a}{q} - \frac{AkT}{q} \ln \left(\frac{J_{00}}{J_{sc}} \right) \quad (3.28)$$

It then becomes apparent that there are four parameters which can mathematically reduce V_{oc} : increased J_{00} , increased A , decreased E_a , or decreased J_{sc} (or voltage-dependent collection of J_{sc}). Further, equations 3.27 and 3.28 can both be graphed for additional insight.

Fig. 3.7 shows the application of Eq. 3.27 to a typical CdTe cell with $A \approx 1.7$ and the extrapolation of this data. It is plotted shifted up by J_{sc} , corrected for parasitic resistances, and on a semi-log scale. The y-intercept gives a value for J_0 around 10^{-7} mA/cm². As can

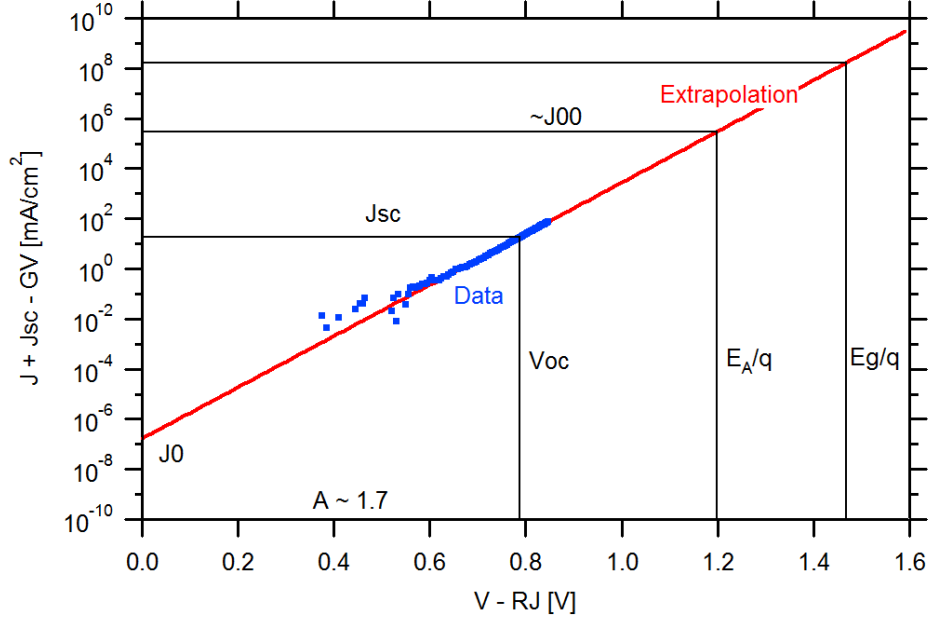


Figure 3.7: Semi-log J-V plot of typical CdTe cell and extrapolation.

be seen from Eq. 3.27, when $V = E_a/q$, then $J + J_{sc} = J_{00}$. However, since neither E_a nor J_{00} are experimentally measured, one cannot be used to directly calculate the other. Both can be calculated theoretically, however, and cross-compared for consistency. The value for J_{00} is the current flow with no barrier, given by

$$J_{00} = pqv_t \quad (3.29)$$

with p the hole concentration and v_t the thermal velocity. Choosing reasonable values for these parameters for a typical CdTe cell gives a J_{00} slightly above 10^5 mA/cm². Likewise, the activation energy can be calculated from the difference between the Fermi level and the conduction band, or

$$E_a = E_c - E_f = E_g - (E_f - E_v) \quad (3.30)$$

Again, choosing reasonable values gives a E_a around 1.2 eV for a typical CdTe cell. These agree reasonably well with each other when matched up on the graph in Fig. 3.7.

Equation 3.28 can be used to gain information from a graph of V_{oc} vs temperature based on experimental measurements. Fig. 3.8 shows open-circuit voltage against temperature for

two sets of CdTe cells, taken from [8] and [31]. The information comes from comparing the slope and intercept between the cells in each pair. In the top case, the slopes are similar, but the intercepts are different; in the lower case, both slope and intercept are different. The difference in intercepts is attributable to a difference in activation energies. The difference in slope results from a difference in either A , J_{00} , or J_{sc} , though this is difficult to separate without additional information.

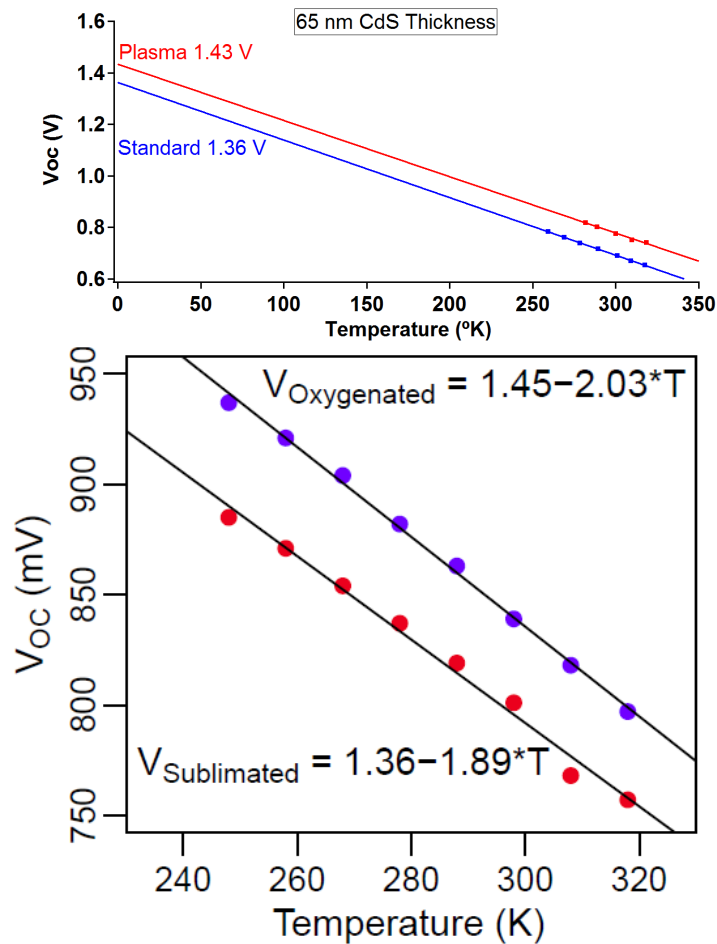


Figure 3.8: V_{oc} vs T graphs for two sets of CdTe cells. The top pair compares plasma cleaned substrates with standard-cleaned substrates. The lower pair compares oxygenated CdS with sublimated CdS.

3.6 Variation of Spectrum, Temperature, and other Extensions

The analysis presented in this chapter was deliberately specific in the test conditions and broad in the cell details. This positions it well to be used as a general framework for evaluating efficiency loss in any cell under standard test conditions. There are, however, several possible extensions and applications of this more general framework. Examples of extensions would be variation in temperature and spectrum, light concentration, or analysis of multi-junction or graded band gap cells. Applications would include detailed analysis of a single technology, as Swanson did with silicon, which was presented above.

Table 3.3: Limiting efficiency and efficiency parameters at different spectral and temperature conditions for two bandgaps

Band Gap (eV)	Temperature (°C)	Air Mass	Irradiance (mW/cm ²)	J_{sc} (mA/cm ²)	V_{oc} (V)	FF	η (%)
1.12	25	0	136.6	53.0	0.884	0.871	29.9
1.12	25	1.5	100.0	43.8	0.879	0.871	33.5
1.12	25	3	67.8	30.3	0.869	0.870	33.8
1.12	25	4	55.8	25.1	0.865	0.869	33.8
1.47	25	0	136.6	36.9	1.210	0.899	29.4
1.47	25	1.5	100.0	30.1	1.205	0.898	32.6
1.47	25	3	67.8	20.0	1.195	0.898	31.6
1.47	25	4	55.8	16.1	1.189	0.898	30.8
1.12	60	1.5	100.0	43.8	0.847	0.856	31.7
1.47	60	1.5	100.0	30.1	1.171	0.887	31.2

Table 3.3 shows how the efficiency and associated parameters change for two band gaps under different spectra and temperatures. The band gaps used in this table were chosen to

match silicon and CdTe, as these are two currently dominant technologies in the market. The temperatures are 25 °C and 60 °C, which are the standard test condition and a nominal upper-limit operating temperature, respectively. The spectra are determined from air masses of 0, 1.5, 3, and 4 based off of SMARTS modeling [32]. For both bandgaps, J_{sc} , V_{oc} , and FF all decrease with decreasing irradiance. However, the total efficiency increases, since the irradiance is decreasing faster than the cell output power. For 1.12 eV, the efficiency continues increasing to AM4, while for 1.47 eV, it peaks at AM1.5. This difference is due to the way in which the spectrum changes with increasing air mass, with most of the loss below 900 nm. This effectively makes the spectrum broader, which has more impact on the higher band gap. There is also significant efficiency loss at higher temperature, although the loss is larger for the smaller band gap cell.

This suggests that a larger band gap would be more useful for areas with strong sunlight and high temperatures, such as desert locations. Lower band gap materials, by contrast, would be better for areas with less light and lower temperatures, such as northern climates.

Chapter 4

WHOLE-CELL CHARACTERIZATION

In order to understand the behavior of a particular cell, the cell must be carefully characterized using a variety of measurements, each of which provides different information. This information can then be combined to provide a more complete picture, since results from one measurement can explain results from a different measurement. This chapter will focus on whole-cell characterization, while uniformity measurements will be addressed in later chapters. This chapter will describe the upgrades to the measurement systems at CSU, information that can be gained and how it can be combined, and applications to several experiments modifying the standard CSU CdTe cell process. The link between whole-cell performance and uniformity will also be explored.

4.1 Upgrades and Additions to Whole-Cell Characterization Systems

In order to provide the most accurate, complete, and quickest information, several upgrades and additions were made to the measurement systems at CSU. These include improvements of the calibration, upgrades to the current-voltage measurement tools, a new area measurement tool, and a new cell stressing system.

4.1.1 Upgrades

Calibration Improvements

The calibration of the light sources for J-V and QE measurements is done using calibrated reference cells. The reference cells have been measured in well-calibrated systems at the National Renewable Energy Laboratory (NREL). For J-V, the solar simulator intensity is

adjusted until the measured short-circuit current of the reference cell matches the known value. For the QE, as the wavelength is varied the cell current is amplified and measured as a lock-in amplifier output. The measurement is done first for the reference cell, then for the test cell. Since QE is proportional to the ratio of cell current to light power at a given wavelength, this can be used to set up the relation

$$QE_{\text{TestCell}} = QE_{\text{RefCell}} \frac{L_{\text{TestCell}}}{L_{\text{RefCell}}} \quad (4.1)$$

where L is the lock-in output. This procedure avoids the need to know the proportionality constants, such as the actual light output, losses in the optical path, or current amplification, as long as these are constant between the reference cell and test cell measurements.

These calibration procedures require reference cells to be stable and have accurate values. However, there was a large time period when the cells were not calibrated after obtaining the reference cells. During this time, the silicon reference cell had drifted significantly in its QE response and the GaAs cell had fallen out of use. Both of these cells were remeasured on well-calibrated NREL systems. Fig. 4.1 shows the original QE calibration data for the Si reference cell from 2006, as well as measurements which were updated in 2011 and 2013. It is apparent in the figure that the cell is still changing, which means that the cell should be remeasured periodically.

A number of CdTe and CIGS devices have also been measured on NREL systems, including the official test systems. Results from these devices are periodically compared with the calibration of the reference cell. The reference cells are also periodically remeasured. This ensures that the calibration is accurate and up-to-date with any changes in the reference cells.

Because the simulator light is not a perfect spectral match for the solar spectrum, it is important to have a reference cell which is a near match for the band gap of the test cell. Having a reference cell and a test cell which are close in band gap ensures that the spectral mismatches are the same for both cells. A silicon cell was originally used as the sole calibration cell, and is still being used for calibration of CIGS devices. In addition, a GaAs

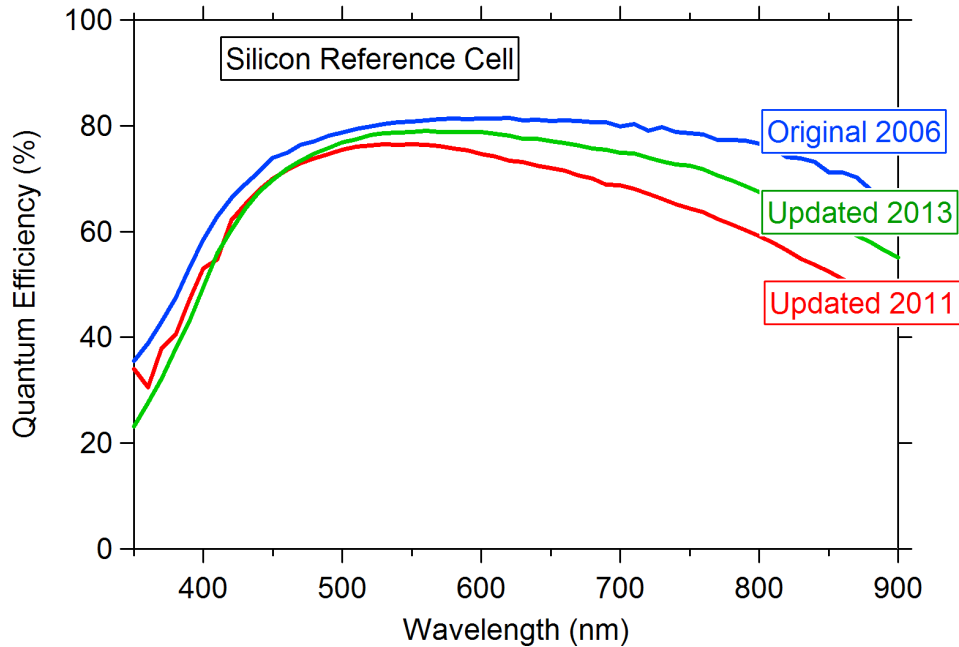


Figure 4.1: Original (2006) and updated (2011) and (2013) QE calibration values for the Si reference cell.

cell is now being used for calibration of CdTe cells because GaAs and CdTe are a closer band gap match than Si and CdTe.

Sourcimeter for Current-Voltage Measurements

The existing current-voltage measurement system had a number of problems, including concerns over accuracy and a slow measurement speed. The system used a programmable power supply to apply bias to the cell. The current and voltage were then measured independently using digital multimeters. These three independent tools were replaced by a single Keithley 2401 sourcimeter. New LabView software was written to operate the system.

The sourcimeter-based system has several advantages over the separated system. The first is speed. The sourcimeter can step through voltages faster than the programmable power supply. This reduces measurement time from about 2 minutes to about 20 seconds. In addition to saving user time, this reduces light-induced heating of the cell, since the

light is shining on the cell for less time. Increased scan speed can introduce errors [33], so measurements at multiple speeds were compared to ensure there were no significant errors.

The second advantage is accuracy. A four-point measurement system is maintained, which ensures that external resistances do not affect the results. The sourcemeter has a feedback system built in so that the measured voltage is the same as the applied voltage. The reduced heating also improves accuracy at forward bias since increased temperature reduces open-circuit voltage.

A final benefit is simplicity. A circuit incorporating the multimeters and power supply has been replaced by two doubled wires plugged directly into the sourcemeter. In addition, a switch was added to change between the four-point J-V measurement and the two-point QE and capacitance measurements, which increases simplicity and reduces user error. The software user interface and data output were also simplified to improve usability and data-sharing capabilities.

4.1.2 New Tools

Area Measurement Tool

In order to accurately determine current density, it is necessary to have accurate measurement of the cell area. An optical system was co-developed with John Raguse to measure contacted area of CdTe cells.

The original measurement technique simply measured a diameter of the cell using a ruler, and assumed the cell was circular. However, a number of asymmetrical cells challenged this assumption and led to an imaging system. The original imaging system was an optical image of the cell, with software to calculate the area. Further problems with the delineation process produced cells where the semiconductor material was not completely removed, or did not line up well with the contacted area.

This led to a transmission-based system. The cell is illuminated from below with sub-CdTe-band-gap infrared light provided by LEDs. The CdTe is transparent to this light, but

the back contact is not. A filter is used on the camera lens to ensure the system is sensitive only to the transmitted light. By careful choice of cutoff intensity, the boundary of the contact can be determined and the area calculated. It was shown from comparisons between optical and EL measurements that the contacted area is the only active area of the device.

Calibration is done using calibrated areas available commercially. These calibrated areas are metal circles printed onto glass slides. When the circles are imaged at the same height as the cell, the pixel size can be calculated. From the pixel size and pixel count of the cell, the cell area can be calculated.

The uncertainties in the system include uncertainty in focal plane while calibrating, area of the calibration source, and choosing the cell boundary. The uncertainty in the cell boundary dominates, and limits the accuracy to within $\pm 2\%$. This uncertainty is consistent with the differences between J_{sc} when measured from J-V and integrated from QE.

Cell Stressing System

Understanding long-term stability is important for making good solar cells. An accelerated cell stressing system was co-developed with John Raguse and Jennifer Drayton [34].

The system uses LED arrays for a light source and a scientific oven for a heat source. This is contrasted with commonly-used systems where incandescent lights are used for both illumination and heating, and a separate cooling system must be used to set cell temperature. The LEDs emit a broad visible spectrum, but very little infrared, which reduces the light-induced heating of the cell. The LEDs are cooled using computer fans. The system provides a large area with relatively uniform light intensity and very uniform heating.

Preliminary results show that degradation can be induced in cells through applying heat and light. Pairing this stressing system with the whole-cell and uniformity characterization described in this dissertation should enable greater understanding of the mechanisms by which cells change under stress.

4.2 Whole-Cell Measurement and Analysis Tools

It is difficult to list in an abstract setting what information can be provided by the various measurement techniques and how they can be used together. Therefore, this section will present only a brief description of the tools and information available. The power of these tools is best explored through applied examples, as will be discussed in Section 4.3.

4.2.1 Current Voltage

Since solar cells are designed for electrical output under light input, the fundamental measurement of a cell is a current-voltage measurement. This is a straightforward process, where a varying voltage is applied to the cell and current through the cell is measured. Since the current should be proportional to the area, the normalized current density (current/area) is usually used instead of current. This measurement can be done both in the dark and in the light. Response to variations in cell temperature and light intensity or spectrum can also be investigated. Although this is a simple measurement, much valuable information is provided.

The first piece of information is determined by three points from the J-V curve which are directly related to the cell output. These are the short-circuit, open-circuit, and maximum-power points. These provide the highest-level metrics for characterizing the cell. However, they are only a starting point.

The next level of analysis involves fitting to the diode equation. This involves the CurVA procedure described in section 2.3.2. From this analysis, values for J_0 , A , r_{sh} , and R_s can be obtained. These provide information about the sources of losses and help explain the shape of the J-V curve. However, when barriers have a significant effect on the behavior of a cell, CurVA analysis can break down. Barriers are often exhibited through non-exponential behavior of the J-V curve. Examples of barrier behavior can include rollover beyond V_{oc} , a kink in the power quadrant, crossover between light and dark curves, or severe current restriction.

Further information about the cell can be gained by repeating J-V measurements at varying temperatures. This can provide information about losses in V_{oc} , as described in Section 3.5. It can also provide information about barriers, since these tend to become more severe at lower temperatures due to reduced carrier energy for overcoming barriers. This has been used to quantify barrier height, with procedures developed by Stollwerck [35] and Koishiyev [36].

Information can also be gained by varying the light intensity. The short-circuit current density is expected to be linear with light intensity. Variations from this linear behavior can reveal photosensitive effects, such as photoconductivity change of CdS. It can also help explain light-dark crossover behavior by illustrating the transition from light behavior to dark behavior. Variation of the light spectrum can also reveal barrier behavior, especially in CIGS, as explored by Song [21].

Although J-V analysis provides much information on its own, it can be further informed by QE and Capacitance measurements. QE measurements can explain the J_{sc} value. Capacitance can provide insight into whether low V_{oc} is related to poor doping or high trap density.

4.2.2 Quantum Efficiency and Optical Measurements

Quantum efficiency is a measure of the conversion efficiency of photons into collected electrons and holes at the cell contacts. It is usually measured at short-circuit current as a function of incident wavelength. It can provide insight into losses of short circuit current, especially when combined with reflection and transmission measurements, as was discussed in Section 3.3. The QE values, distribution, and slopes all provide information. The band gap can also be estimated from QE by looking at the long-wavelength fall-off point.

The CdS thickness can also be determined from QE measurements. This is done using a Beer-Lambert Law absorption profile and known absorption coefficients, $\alpha(\lambda)$. The QE below the CdS band gap is compared to the QE above the CdS band gap. The thickness

can be calculated from

$$t = \frac{1}{\alpha(x)} \ln \left(\frac{QE(y)}{QE(x)} \right) \quad (4.2)$$

where x is a wavelength which is strongly absorbed by CdS, typically 400-500 nm, and y is a wavelength which is absorbed by CdTe but not CdS, such as 600 nm. An average QE value over 600-800 nm can be used for y . The calculation can be done for several values of x , and an average of these calculated values used. This calculation assumes that all other losses are uniform with wavelength. This is not a perfect assumption, but by averaging over several wavelengths, a reasonable value can be reached which agrees well with the intended deposition thickness.

Further information can be gained by applying a light or voltage bias. The role of light bias was explored by Nagle [37] and can be used to explore photoconductivity and light-dependent collection in a device. Voltage bias was explored by Gloeckler [38] and can aid in understanding photoconductivity, contact collection, and barriers.

Optical measurements of reflection and transmission of a cell, its substrate, and various layers can be used to quantify current losses. Reflection measurements from a finished cell provide one source of loss information. Absorption for any material can be calculated from the equation

$$\text{Reflection} + \text{Absorption} + \text{Transmission} = 100\% \quad (4.3)$$

where reflection and transmission can be easily measured. Further, absorption losses should add linearly. By finding the absorption for devices at each stage in the process, the absorption of each layer can be calculated. For example, absorption measurements on a bare substrate, substrate/CdS, and substrate/CdS/CdTe yield absorption values for the substrate, CdS, and CdTe layers. It is important to note that reflection is highly dependent on the layer stack, so it must be measured each time for changing stacks. However, the reflection is very consistent for similar devices.

4.2.3 Capacitance

Capacitance measurements can be used to understand the electronic structure of cells. In the simplest model, the two edges of the depletion region are treated like the plates in a parallel-plate capacitor with a dielectric between them. Complications to this model include trap states, varying doping densities, and additional diodes. The capacitance can be measured by applying an AC bias. Information can be gained by sweeping the DC bias, frequency, temperature, modulation height, and light bias. Our measurements focus primarily on the first two.

Capacitance-frequency measurements can be used to deduce trap states [39]. States which are longer-lived will not be accessible at higher frequencies, and will result in a step in the C-f graph. However, these states are rarely seen in CdTe cells at room temperature. High frequencies (near 1 MHz) are often approaching an L-C resonance in the measurement circuit and give erroneous capacitance values [40]. Between the low-frequency trap states and the high-frequency resonance is a well behaved region, often near 100 kHz. The primary use of C-f in this lab has been to choose a well-behaved frequency to use for C-V measurements.

Capacitance-voltage measurements can provide a profile of doping in the cell by moving the edge of the depletion region with applied bias. This can give information about the electronic width (which could also be called the apparent width or the C-V width), which is the point where the hole concentration turns up at the back, as well as the bulk hole concentration, which is the bottom of the curve. However, there are several caveats to any quantitative data. There are several violated assumptions in the simple model, including the presence of deep levels, multiple junctions, and lack of quasi-neutral region. These often lead to artificial upturns towards the front and back of the device, as well as artificially high doping values [41]. Nonetheless, C-V can provide valuable information about the doping of a solar cell.

4.3 Applications to CdTe Experiments

The previous section laid out generally what information could be gathered from these measurements and tools. It is more illustrative to use specific examples to demonstrate how they are beneficial. This section contains several examples of how these tools have been applied to various CdTe experiments to understand the cell behavior and improve device performance. My role in this work was device characterization. The credit for developing and implementing the experiments goes to the authors as cited in the appropriate sections.

4.3.1 Baseline Process

A baseline process is important so that experiments which modify the process have a control sample. K. Cameron and K. Barth have largely been responsible for maintaining the baseline process at CSU. The above characterization tools have been used for tracking the performance of CSU CdTe cells under standard processing conditions. This has helped to identify when things are awry in the manufacturing process. For example, it has helped to find inconsistencies in delineation, copper contamination, and nonuniform heating problems. Having standard samples has also helped to keep calibration standard up to par at both labs, and has been useful for characterizing the measurement process.

One concern with the measurement process is consistency over time. To check for consistency, 3 cells were measured seven times over seven different days. The results are shown in Fig. 4.2 and are highly consistent. Variation in each parameter, J_{sc} , V_{oc} , and FF was found to be 1% or less. Variation in the total efficiency was less than 2% relative, or $\pm 0.2\%$ absolute. This is simply a measure of the random uncertainty in the measurement, and makes no claim about the systematic error.

A standard sample was also used to ensure that the J-V measurement was insensitive to direction or speed. The results are shown in Fig. 4.3. The standard procedure is reverse to forward bias with a 0 ms wait. It can be seen that there is relatively little change in the results by changing either direction or speed. The slight difference in V_{oc} and fill factor is

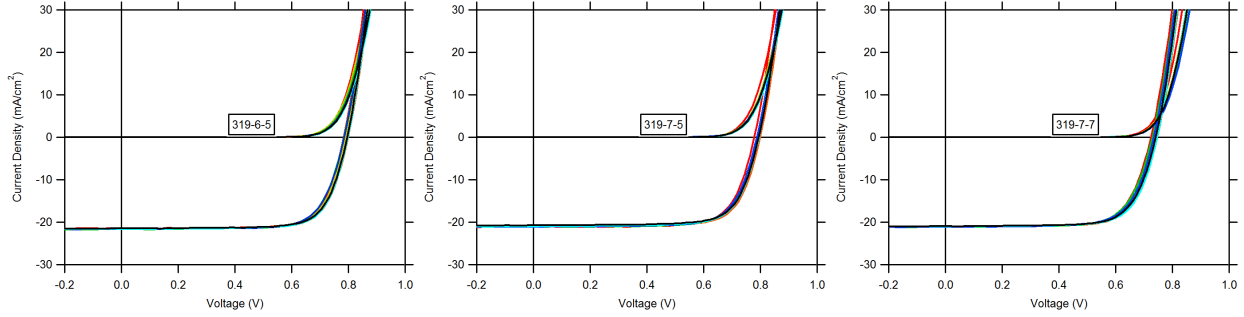


Figure 4.2: Three different cells measured seven times over seven days.

likely due to changes in heating, caused by differences in the time between the start of the measurement and reaching the open-circuit point.

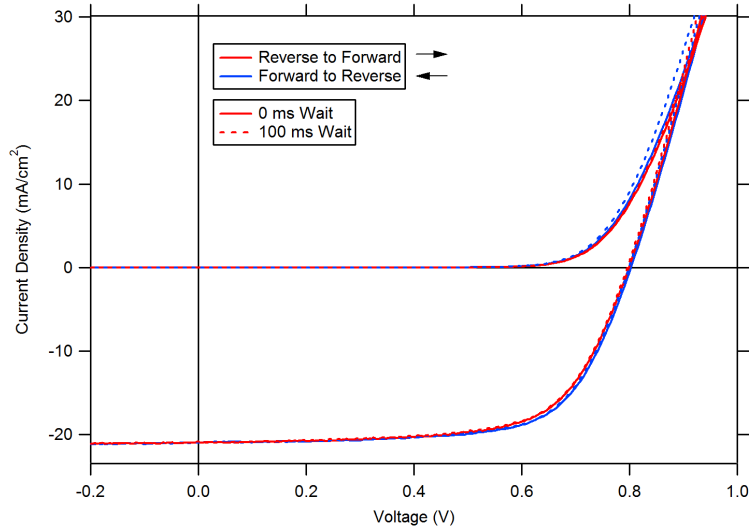


Figure 4.3: J-V measurements of a single cell while varying voltage-sweep direction and wait time between voltage data points. There is little difference with either of these variations.

4.3.2 Plasma Cleaning

A hollow-cathode plasma source for cleaning the substrate prior to cell deposition was developed by Drew Swanson [8]. This was intended to provide cleaner substrates than the standard cleaning process, which involved ultrasonic detergent, water, and isopropyl alcohol rinses. A cleaner substrate should reduce problems with the CdS deposition. As shown

in Fig. 4.4a, thinner CdS is desirable because it can increase the short-circuit current by allowing better blue current collection. Blue current is defined as the current calculated when QE is integrated from 400-500 nm as in Eq. 2.5. However, as the CdS is thinned, the open-circuit voltage falls off. There is a cliff below 100 nm which reduces performance significantly.

Fig. 4.4b shows that plasma cleaning can shift the cliff relative to the standard cleaning and reduce the slope of the cliff. This allows slightly thinner CdS to have higher current with little loss in voltage, which increases the peak efficiency by as much as 1.5% absolute. This improvement may be related to the reduction of pinholes in the CdS layer, or may be related to improved interface properties. The plasma cleaning also leads to modest improvements in the uniformity of the samples under EL and LBIC measurements, especially at forward bias.

One other consequence of the plasma cleaning is to affect the growth rate of CdS. This was identified through QE measurements, as shown in Fig. 4.4c. These cells were made under identical CdS growth conditions, but had varying plasma currents applied during the cleaning step. A small plasma current reduces the growth rate from the standard cleaning baseline, but increasing current leads to higher growth rates. The QE results helped to optimize the CdS deposition time so that devices with comparable CdS thicknesses could be directly compared. QE was also used to calculate CdS thickness to determine the x-values and the blue current used in Fig. 4.4a and b.

4.3.3 Thinning CdTe

Work is being done to incorporate an electron reflector into CdTe devices. In order for an electron reflector to have maximum effect, however, the cell must be fully depleted even at forward bias [42]. Without direct control over the doping of the CdTe, this requires the CdTe be thinned. Thin CdTe, however, comes with the potential drawbacks of reduced current due to incomplete absorption or collection and reduced voltage due to a reduced

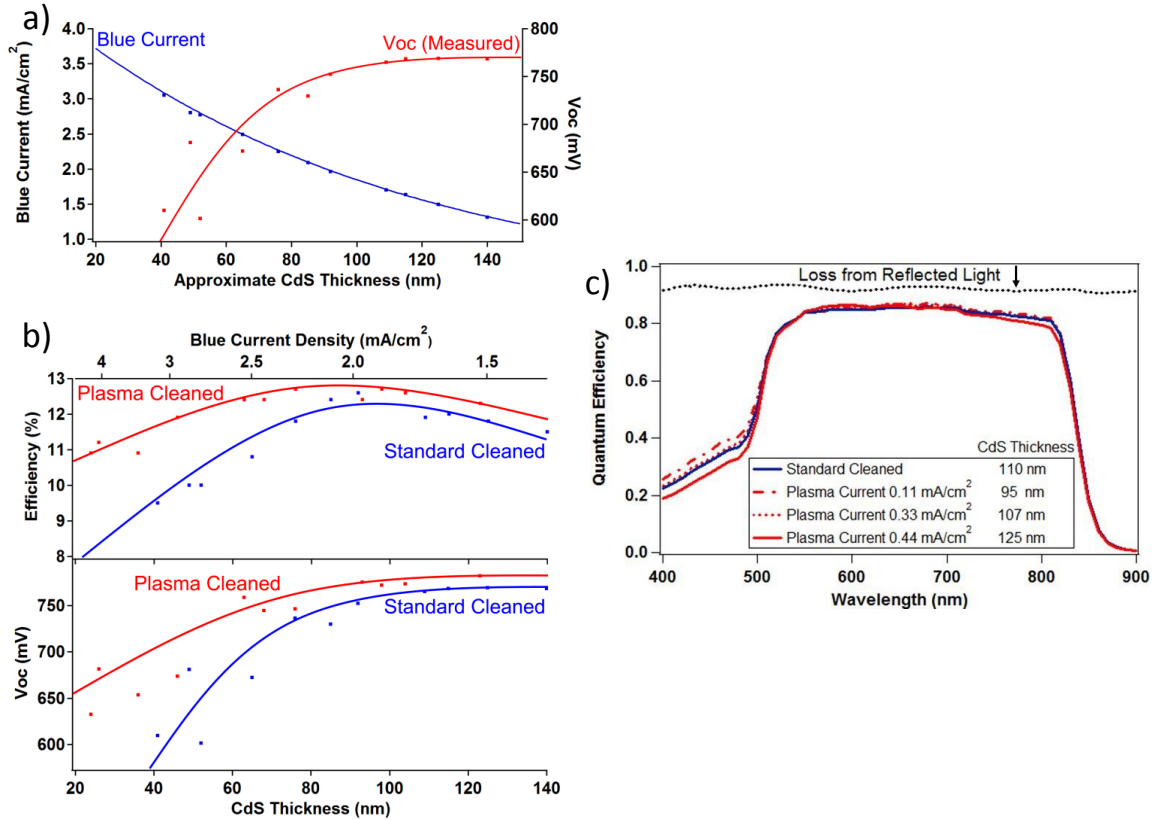


Figure 4.4: a) The voltage cliff and current pickup with thin CdS. b) The improvement in V_{oc} and efficiency with plasma cleaning. c) QE which shows changes in CdS thickness with changing plasma current.

built-in field. To understand the behavior as thickness is varied, several cells were made with CdTe thickness below the standard $2.2 \mu\text{m}$ [43].

To explore current losses, QE and transmission measurements were performed. Fig. 4.5a shows the breakdown for a $0.6 \mu\text{m}$ thick CdTe cell. Reflection was measured on a finished device and substrate absorption was measured for a bare substrate. These values were assumed to be constant for all the devices in the run. Transmission was then measured on a film without a back contact and QE was measured on a contacted device of the same thickness. This allows for the separation of the blue “Not Absorbed” region which was transmitted through the film from the green “Not Collected” region which was absorbed but

did not show up in the collected current. The “CdS Absorption” was cut off at 510 nm, the band gap of CdS, although the actual boundary is certainly not this abrupt.

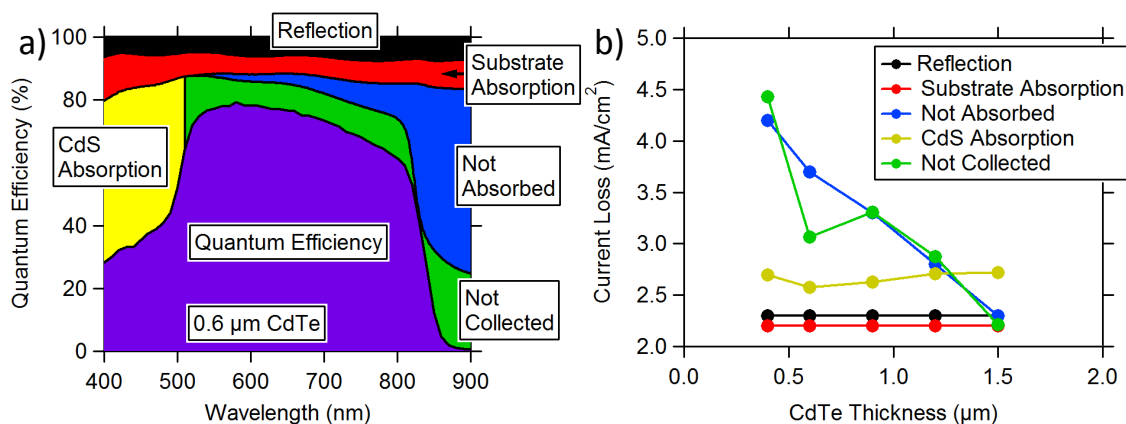


Figure 4.5: a) Current loss analysis for a cell with a 0.6 μm thick CdTe layer. b) Current losses as CdTe thickness varies.

Fig. 4.5b shows quantification of this analysis for cells with CdTe thicknesses from 0.4 μm to 1.5 μm . The CdS absorption is relatively constant. The losses from non-absorption (transmission) increase significantly with thinning CdTe, as expected. Except for one data point (which may be an artifact), the losses from non-collection increase at the same rate as the transmission losses. This may be related to a non-ohmic contact, which creates a reversed diode at the back of the cell. Since the bands are sloping to the back of the cell, any electron-hole pairs generated in this region will be collected in the wrong direction, causing a double loss in QE. Assuming this back diode has a fixed width, the fractional area of the back diode increases with decreasing CdTe thickness. The back diode also gets more photons as the cell is thinned. The 0.4 μm cell is severely shunted, which could also be explained by the overlap of the front and back diode.

4.3.4 High-Efficiency Cd(S,O)/CdTe Devices

Parasitic absorption in the CdS layer can be a major source of loss, as was seen in Figs. 3.5 and 4.5. One approach to reducing this loss is thinning the CdS layers, as described in

Section 4.3.2, which has the downside of reducing V_{oc} . Another approach involves choosing new materials or modifying the CdS to be more transparent. A system for sputtering CdS in the presence of oxygen was developed by Jason Kephart [44]. Oxygen incorporation during sputtering of CdS creates Cd(S,O), which increases in transparency with increased oxygen. Pairing this with a more transparent glass/TCO and a high-resistance transparent (HRT) or buffer layer leads to higher efficiency cells [45] [31].

Fig. 4.6 shows the changes in the cell behavior with oxygen. The oxygen is measured as a fraction of argon in the gas flowing into the deposition chamber. Although higher oxygen in the flow gas leads to higher oxygen incorporation into the film, this is not a direct measurement of oxygen in the Cd(S,O). The improvement from oxygenation is most apparent in the QE graphs in Fig. 4.6a. The low-oxygen cells have similar QE to a standard CdS cell, though the CdS absorption edge is much less sharp. At 2% and above, the short-wavelength response increases significantly. However, at 2.5%, the QE drops uniformly, and at 3% it drops to nearly zero. This is likely caused by a significant current-limiting barrier at the front of the device.

Fig. 4.6b shows J-V results for this same set of cells. The 0% cell has poor performance, while the 1% cell has performance similar to a typical CSU CdTe cell. At 2%, there is a large jump in current, which is accompanied by an increased series resistance. The 2% cell has an efficiency of 12.7%. Beyond 2%, the current is severely limited. At 3%, both the light-generated and the forward current are severely limited, preventing the typical diode turn-up at far forward bias.

The hole density profile from C-V measurements is shown in Fig. 4.6c. At 2% and below, there is little change with oxygen. Above 2%, there appears to be an increase in hole density. However, this may be caused by barrier effects which change the capacitance behavior, rather than an actual change in the hole density.

Optimizing the HRT layer and the Cd(S,O) layer can result in very high-efficiency devices relative to the baseline. One such device is shown in Fig. 4.7. Part a of this figure shows the near-total use of available current. Significant further gains could be made by reducing

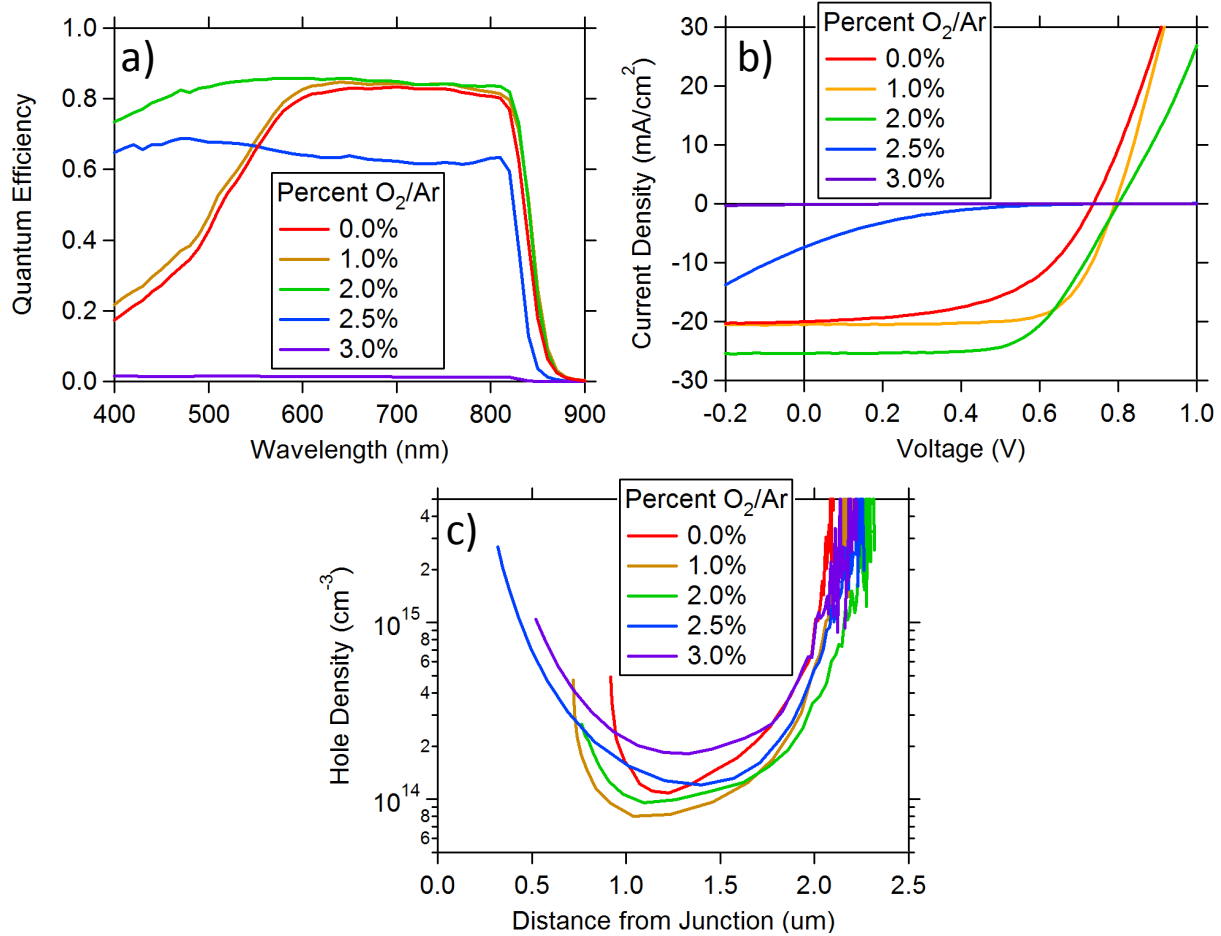


Figure 4.6: a) Quantum efficiency results, b) J-V results, and c) C-V results with increasing oxygen flow.

the reflection and absorption of the substrate, but the losses internal to the cell are very small, and only present at longer wavelengths. Part b shows the J-V curve for this device. Because the solar simulator has low short-wavelength intensity, and because there was difficulty measuring the area correctly, this J-V curve was corrected to the J_{sc} value obtained from QE measurements by shifting the light J-V curve. The other parameters reflect this correction as well, though not as directly. A cell measuring 15.2% was confirmed by NREL, though there was difficulty with contacting and area measurement, so higher efficiency may be possible.

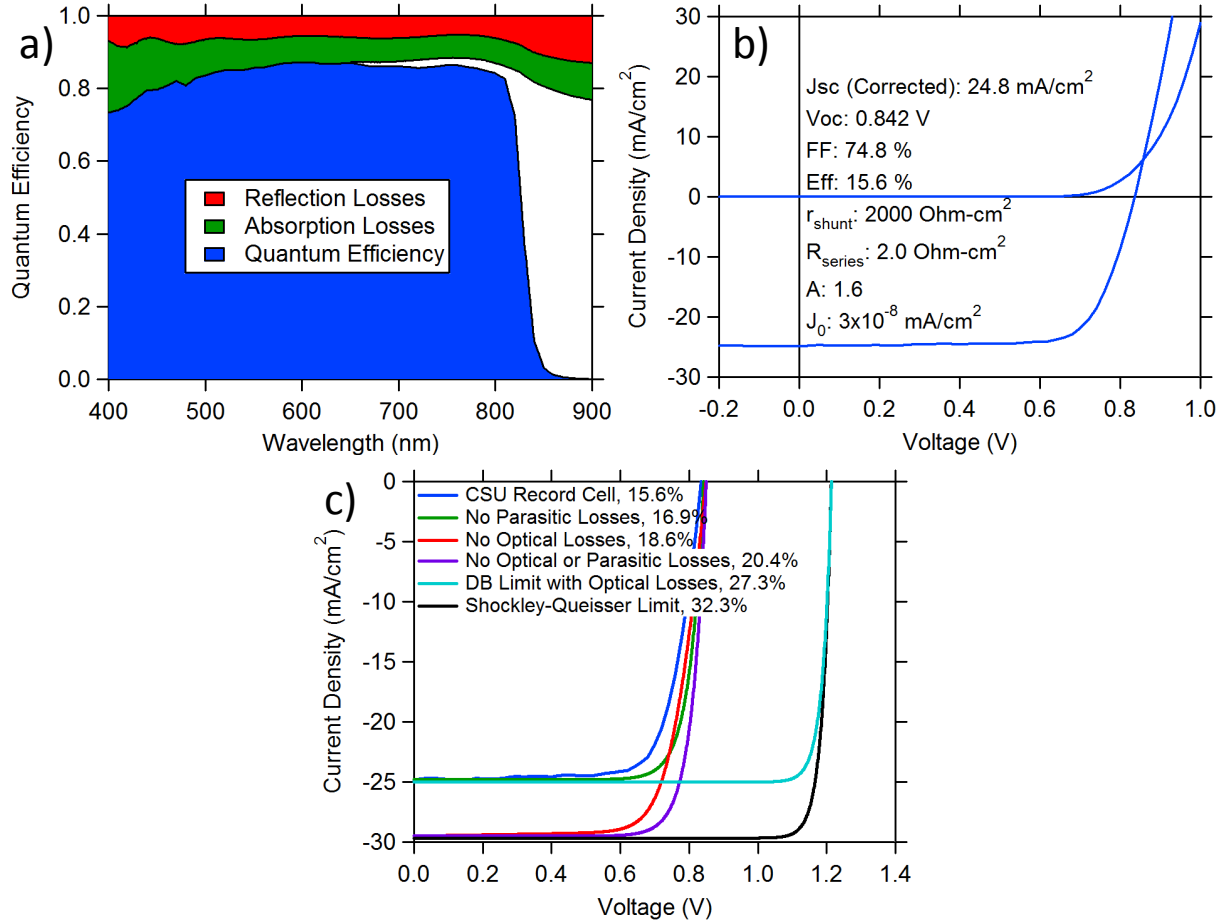


Figure 4.7: a) Quantum efficiency results, b) J-V results, and c) loss analysis results with for a high-efficiency cell using an optimized HRT and Cd(S,O).

Part c of Fig. 4.7 shows theoretical routes to higher efficiency. Removing parasitic losses due to r_{shunt} and R_{series} would improve efficiency by 1.3%. Removing optical losses would increase J_{sc} to 29 mA/cm², and efficiency by 3%. Combining these improvements gives an additional boost, increasing efficiency beyond the sum of the two gains by 0.5%. It is interesting to note that the 20.4% of this hypothetical cell is the same as the present CdTe record, although the record cell has lower FF and higher V_{oc} . The detailed balance limit is calculated from Eq. 3.25 based on no electronic losses, and is the limiting efficiency for the measured QE. Finally, the Shockley-Queisser limit assumes perfect optical and electronic characteristics, but an actual CdTe band gap, rather than an ideal band gap.

4.4 Relationship between Uniformity and Whole-Cell Performance

The preceding material has focused on whole-cell performance. The following chapters will focus on uniformity. This section is an attempt to bridge between the two approaches to device analysis. It will explore the ways in which uniformity can affect whole cell performance, as well as the direction and magnitude of the effects. It will be largely qualitative, though with some attempts and direction to move towards a more quantitative analysis.

To begin, it is necessary to have a way to obtain quantitative information from nonuniformity measurements. This is often done using a histogram which plots the number of pixels or data points at every value. The simplest quantity to derived from a histogram is an average value, either the QE value which can be obtained from LBIC (which is related to J_{sc}), or the EL intensity (which is related to V_{oc}). This value is directly connected to the device performance. In most cases, a simple arithmetic mean is appropriate, though when logarithms are involved, as is often the case for EL images, the geometric mean may be more appropriate.

The next step is to actually measure the nonuniformity, which is the width of the peak in the histogram. The simplest measure is the full width at half max (FWHM), which works well for single-peaked shapes. It is also useful to divide by the average, to express the FWHM as a percent distribution about the average. In theory, higher moments could be included, but there is diminishing value in quantifying these values, since the peaks tend to be very nonideal. It is worth noting that peaks tend to be skewed towards lower performance with a relatively sharp falloff at higher performance. This is connected to the fact that defects in the material tend to reduce performance, rather than improve it.

With a method of quantifying nonuniformity, the next question is whether good uniformity is correlated with efficiency or other parameters. In general, the answer seems to be no. The average is more important than the distribution. There can be correlation, but this is often due to a third effect improving both, rather than the uniformity directly improving the

performance. In addition, a narrower distribution can be centered higher, which can cause a slight improvement in performance.

There can certainly be occasions where better uniformity and better performance are correlated. This is true for plasma cleaning, as shown in Fig. 4.8. For two cells with 65 nm of CdS, the standard-cleaned cell has clearly lower performance than the plasma-cleaned cell. Likewise, the standard-cleaned cell has modestly worse uniformity, especially at forward bias, as can be seen both from the LBIC maps and from the histograms. However, this is likely a case of the plasma cleaning improving both the uniformity and the efficiency, and there is no causation between the uniformity and the efficiency. This is especially true because the improvement in efficiency is exclusively due to improved voltage, to which the LBIC is less sensitive.

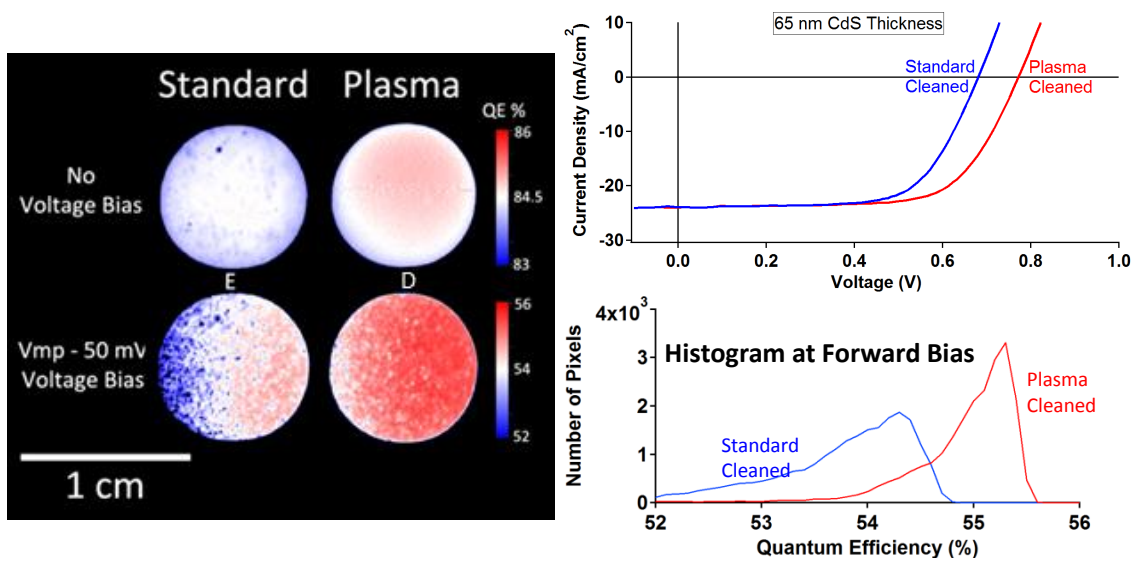


Figure 4.8: Standard and plasma cleaned cells with 65 nm CdS. The J-V (upper right) shows improved V_{oc} with plasma cleaning. The LBIC shows modestly improved uniformity with plasma cleaning, both from the scans (left) and histogram at forward bias (lower right).

For a cell which has undergone stress, both the uniformity and the performance can change. However, they need not change in the same direction. Figs. 4.9 and 4.10 show the results in histogram and image form, respectively, for a cell which underwent a 24 hours of

stress at 85 °C with nominally 1 sun irradiance. The J-V curve in Fig. 4.9a clearly shows that the cell has degraded, mostly through fill factor. EL and LBIC at 638 nm (b and c) show that the peak value shifted down and the width, expressed as a percent of the peak value, increased after stress. However, for the 850-nm LBIC, the opposite effect was observed. The peak shifted to a higher value, and the distribution narrowed.

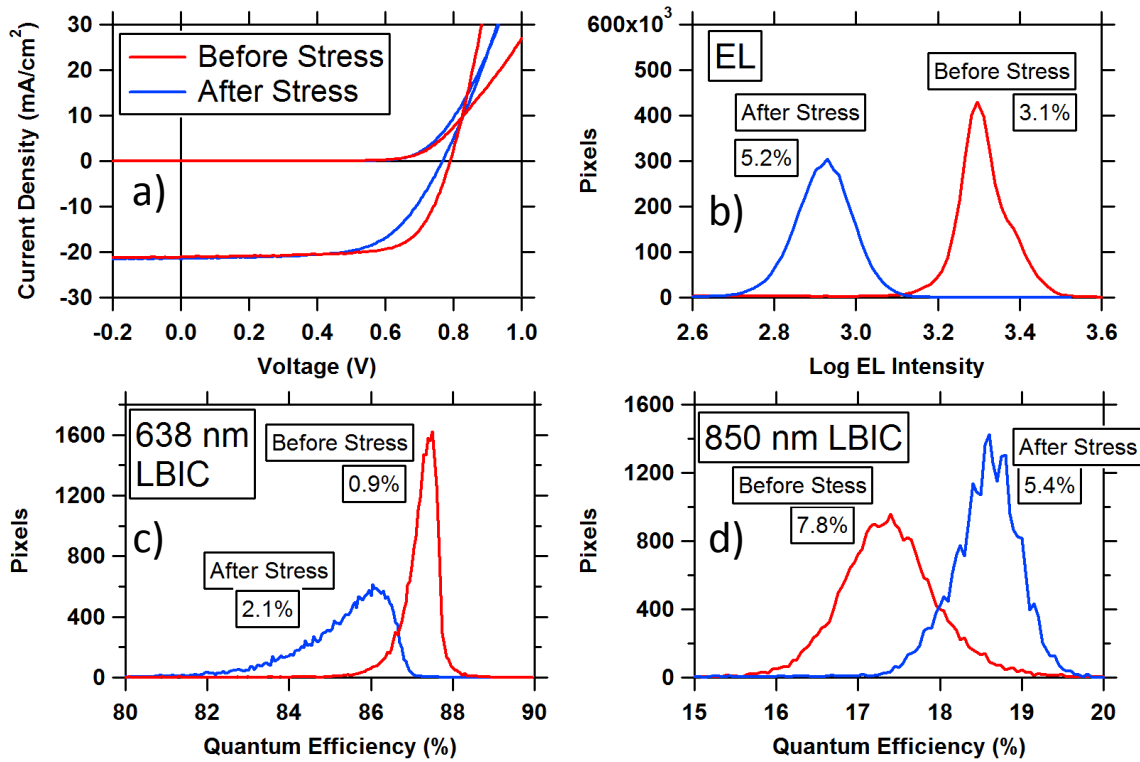


Figure 4.9: a) J-V measurements before and after stress. Histograms of uniformity measurements before and after stress for b) EL, c) 638 nm LBIC, and d) 850 nm LBIC. Numbers are peak FWHM as a percent of peak value.

The images in Fig. 4.10 show the same effect as the histograms. The EL and 638-nm LBIC clearly become less uniform and have a lower average value. The 850-nm LBIC, by contrast, increases its average and smooths slightly. The smoothing may be caused by the sulfur which modifies the band gap moving to a more uniform distribution during the stressing process.

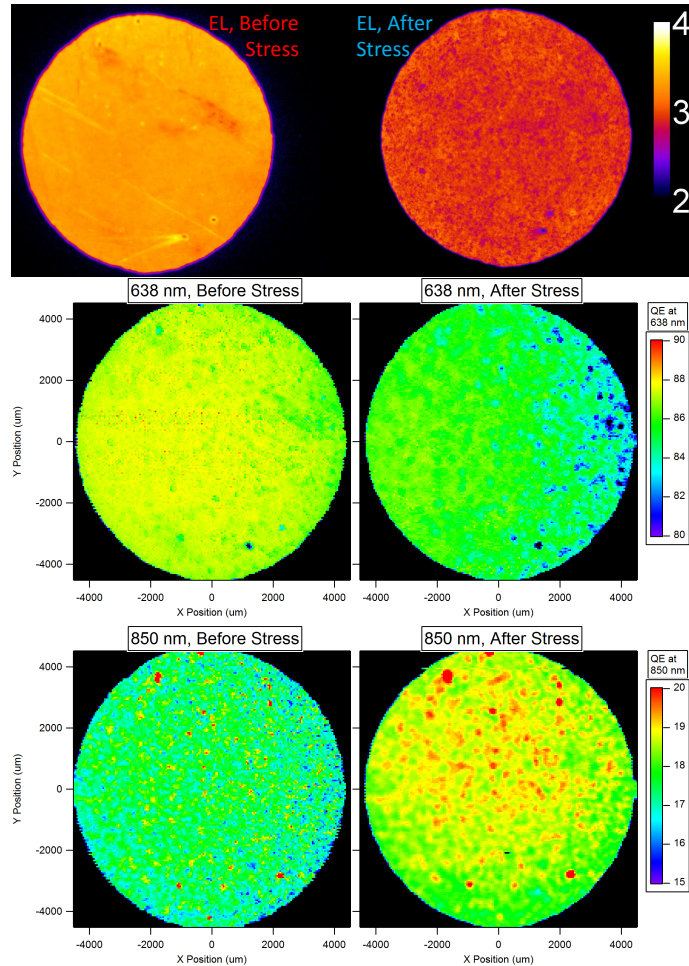


Figure 4.10: EL (top), LBIC at 638 nm (middle) and LBIC at 850 nm (bottom) of the same cell before (left) and after (right) stress. EL images by J. Raguse.

Sometimes, however, a single nonuniformity can effect the performance of the entire cell. This is especially true for shunts, which can effect an extremely large area of the cell. Fig. 4.11 shows a cell which became shunted after stress. Although it is clear from the low-contrast image (left) that the shunt is not large in area, it is clear from the high-contrast image (right) that the shunt reduces QE across a large area. The severity of the shunt prevented forward-bias LBIC, but it is expected that high bias would localize the shunt further [46]. The shunt also completely eliminated any measurable EL signal.

This section has given examples of the relationship between whole-cell performance and uniformity. The examples have been largely qualitative. A goal for future work in this area

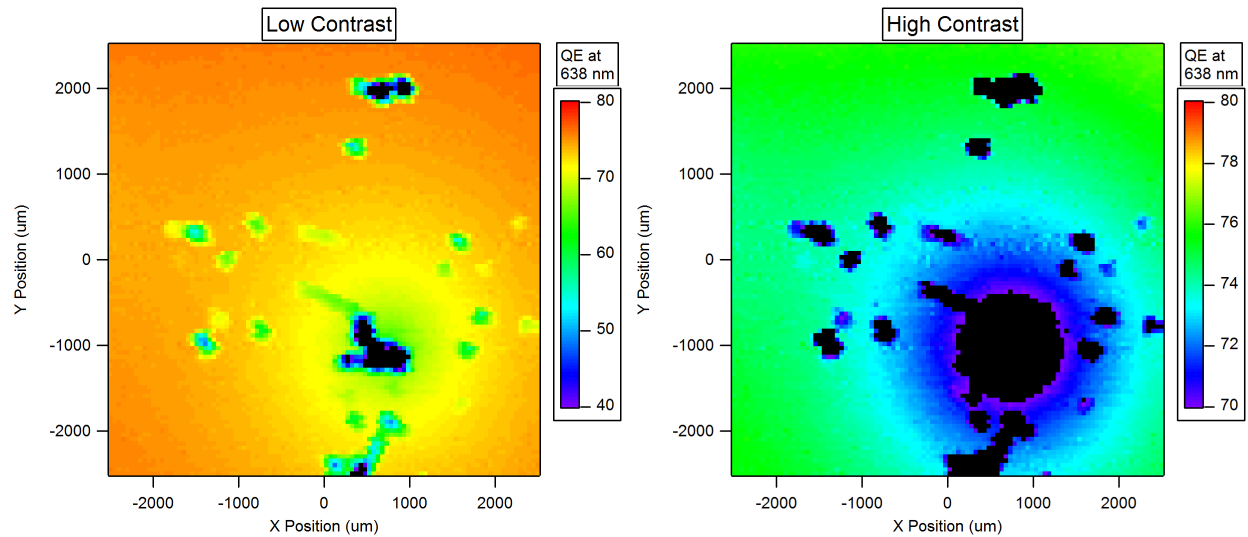


Figure 4.11: LBIC of a cell with a shunt at low contrast (left) of 40-80% QE and high contrast (right) of 70-80% QE.

would be a better way of quantifying uniformity. An extensive comparison between quantified uniformity and cell efficiency or other parameters could then be made. By comparing across many cells, it could be shown conclusively the ways in which uniformity and performance were or were not related. It is possible that there would be little, if any, correlation between uniformity and any of the other cell performance parameters.

Chapter 5

LBIC EXPANSION AND IMPROVEMENT

The LBIC system at Colorado State was originally designed and built by Jason Hiltner [47]. It consists of a light source and optics with controllable wavelength and intensity, a system for measuring cell response, and stepper motors for focus control and cell motion. The apparatus is depicted in Fig. 5.1.

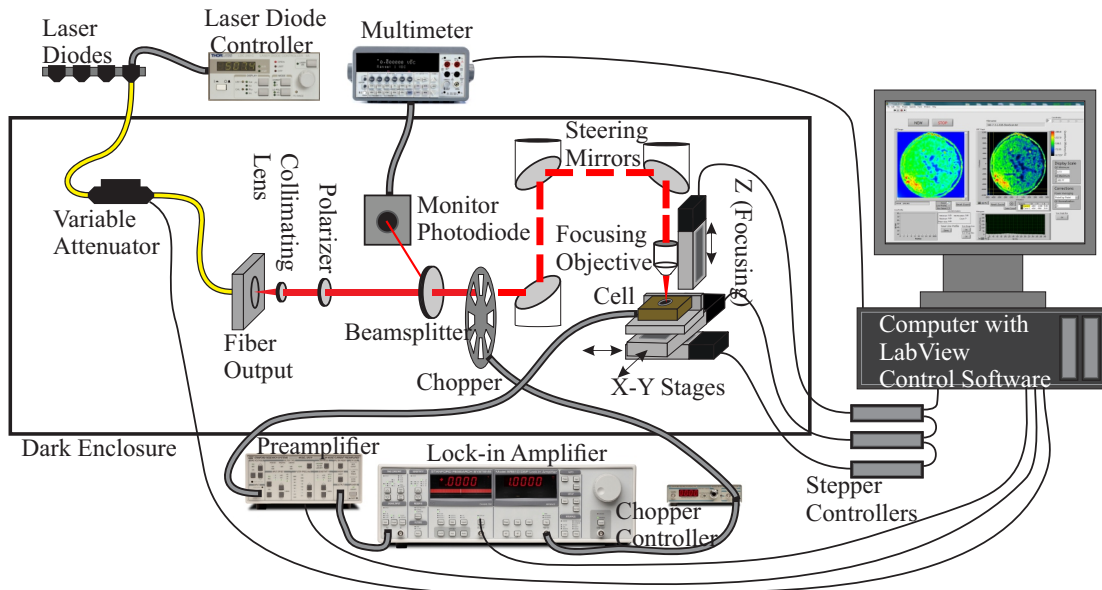


Figure 5.1: Diagram of CSU LBIC System.

The light source is provided by laser diodes controlled by a Thorlabs LDC201C controller. The lasers are pigtailed into a fiber optic, which passes through a computer-controlled attenuator. The fiber terminates into free space, where it passes through a collimating lens, a polarizer, and a 90/10 beamsplitter. Since the splitting of the beamsplitter is polarization dependent, the polarizer ensures that the splitting fraction is constant. The smaller fraction of the beam is sent to an amplified monitor photodiode (Thorlabs PDA100A), and the signal is measured by a Chroma 12061 multimeter.

The remainder of the beam passes through a mechanical chopper (SRS SR540). Steering mirrors direct the beam to a focusing objective (Olympus 1-UB367). The focused beam shines on the cell. Stepper motors (Newport CONEX-MFACC) control the position of the objective for focusing, as well as the position of the cell for scanning. The output of the cell goes to a preamplifier (SRS SR570), whose output goes into a lock-in amplifier (SRS SR810). The frequency from the chopper is used as the reference frequency for the lock-in. The entire system is controlled by a computer using home-built LabView software.

Four laser wavelengths are available in the system: 405 nm, 638 nm, 830 nm, and 850 nm. Since these different wavelengths are absorbed differently by the layers in a solar cell, they can provide information about the different layers.

The system does not have a bias light. In the case of CdTe cells, there is generally little difference in QE between cells which are light-biased and those which are not. In addition, the light bias would degrade the signal-to-noise of the system.

5.1 Hardware Upgrades

Part of the dissertation research consisted of several upgrades to the original LBIC system. These upgrades fall into three broad categories: a new laser, efforts to reduce system noise, and general repairs and upgrades. The first is a true upgrade which adds additional functionality and information to the system. The second is an effort to improve the reliability and results from the system by a multi-pronged attack on noise. The third contains general upgrades to both hardware and software needed to keep the system functioning into the future.

5.1.1 405 nm Laser

Existing LBIC wavelengths of 638 nm, 830 nm, and 850 nm are sufficient for thoroughly exploring the absorber layer of a CdTe cell. However, the window layer, usually CdS, of the cell is not probed by these wavelengths, yet can contribute significantly to the nonuniformity

and performance losses of the cell. A 405-nm laser was added to look at the CdS layer. The existing mirrors in the system were not reflective at 405 nm, so they were replaced with Thorlabs BB1-E02 mirrors, which are reflective from 400 to 900 nm.

Nonuniform CdS deposition can cause significant problems in the cell performance [8] [48]. Regions of missing CdS, often called “pinholes”, put the CdTe and TCO are in direct contact. Since CdTe and TCO form a poor junction, this type of region will likely have reduced performance. Even regions of thin CdS can reduce performance through poor junction quality, likely as a result of unfavorable band alignment [49].

Because the 405-nm light is higher energy than the 512-nm CdS band gap, the light is strongly absorbed by the CdS layer. Electron-hole pairs generated in the CdS are not usually collected, so this light will not contribute to current. Light which passes through the CdS and is absorbed in the CdTe will be well collected, given a high overall QE of the cell. Since transmission through CdS depends on thickness, the QE at 405 nm is primarily a measurement of CdS thickness. Thinner CdS layers or regions will absorb less light, and have higher QE due to better collection in the CdTe. Thicker CdS layers or regions will absorb more light, and have lower QE due to the worse collection in the CdS.

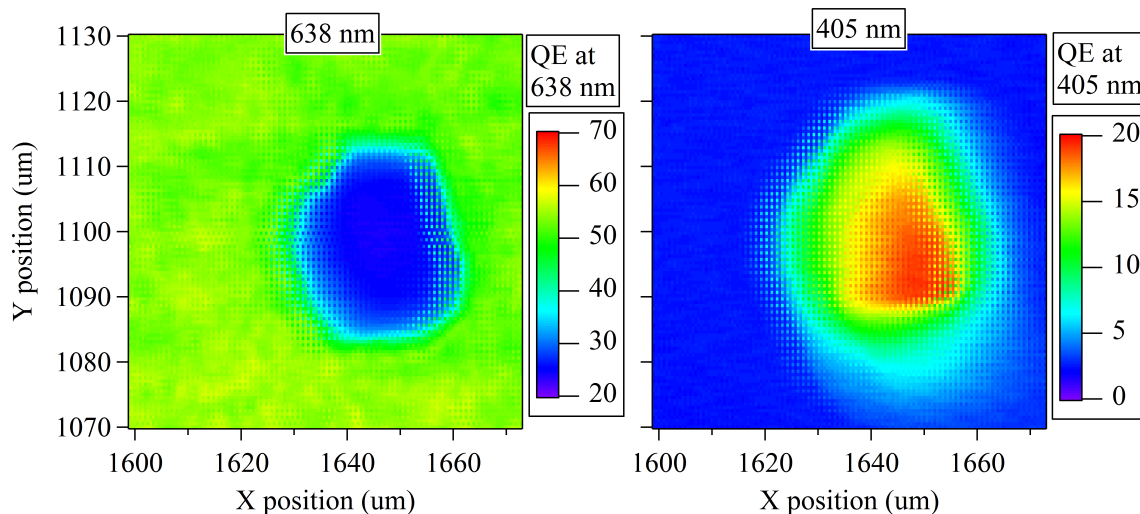


Figure 5.2: High resolution LBIC scans showing a region of thin CdS.

Fig. 5.2 shows a region which has a thin CdS layer, about 20 μm in diameter [50]. The 405-nm scan at right shows an increased response, while the 638 shows a decreased response. The increase at 405 nm is likely a thin region of CdS, allowing higher transmission to the CdTe where there is better collection. The decreased response at 638 nm is likely caused by reduced junction quality due to the thin CdS. These spots are often referred to as “pinholes”. However, there is not good evidence to suggest that the CdS has zero thickness in this region. A true hole would result in QE at 405 nm similar to QE at 638 nm. Since there is only an increase to 20% QE, it is likely only a thinning of the CdS, rather than a complete absence of CdS.

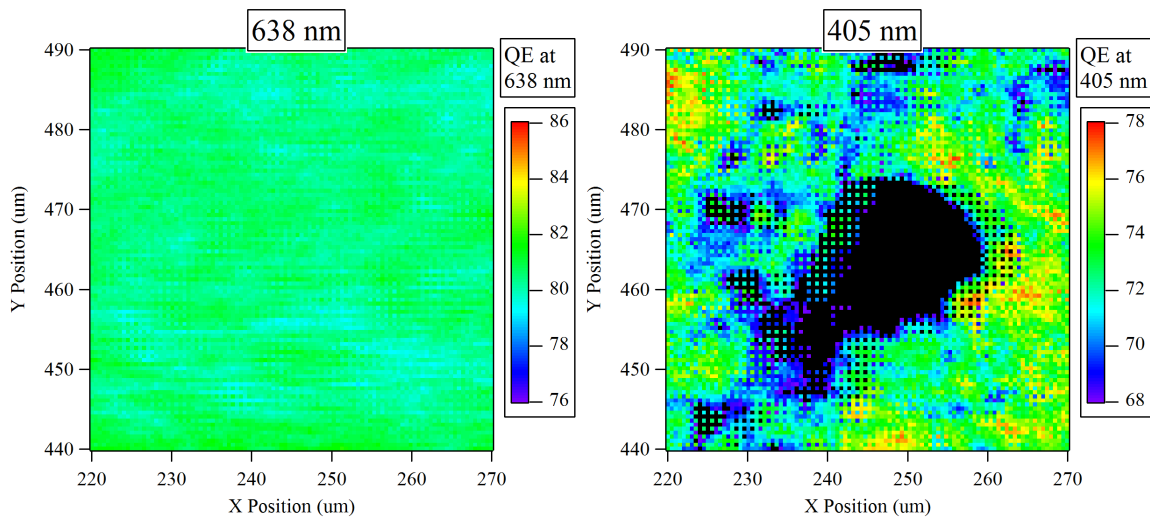


Figure 5.3: High resolution LBIC scans showing a region of low oxygen Cd(S,O). The cells are made with 2.5% oxygen in the sputter gas.

When using Cd(S,O) as the window layer, as described in section 4.3.4, changes in 405 nm QE can be caused by oxygen content rather than layer thickness. It was shown in Fig. 4.6a that lower oxygen led to lower QE at short wavelengths. Fig. 5.3 shows a region of reduced QE at 405 nm [44]. Since this is a reduction in QE, rather than an increase, it is not caused by thinning CdS. The 638 nm response is unchanged, so this region does not cause a weak diode. This feature could potentially be a region of thicker Cd(S,O), though since this material is very transparent, it would have to be extremely thick to cause such a reduction

in QE. More likely, this reduced QE is caused by a region of reduced oxygen content, which reduces transparency to 405 nm light.

5.1.2 Noise Reduction Efforts

Since the light falling on the cell during an LBIC measurement can often be very low power, especially at small spot sizes, noise is a constant concern. Several methods were used to reduce the noise, including a darkened enclosure, a power conditioner, a new laser diode controller, an optical chopper, and a new intensity monitoring system.

The darkened enclosure is designed to reduce room light. It is not sufficiently dark, however, that the room lights can be left on with no noise penalty, except maybe with the least sensitive measurements. The enclosure is also more robust and makes access to all the components easier.

The power conditioner is designed to filter the AC line power to provide a constant voltage to the instruments. To date, it has not been shown to produce a measurable reduction in noise, likely because all the instruments have protections already built in. It may, however, provide additional protection and stability to the instruments in the case of a larger power fluctuation.

One major source of noise is from fluctuations in laser intensity, partially due to instability in the laser diode controller. The old controller was replaced with a new Thorlabs LDC 201C. The results from the old and new controller are shown in Fig. 5.4 The old controller has obvious short term variations which are problematic. The new controller, after a short warm-up time, is relatively stable. Although it is generally very stable, it can still have occasional periods of fluctuations in the long term. These long term instabilities are likely caused by temperature fluctuations in the laser diode and could be corrected with temperature control. Their magnitude, however, has been small compared to the usual display resolution of the LBIC images.

In order to use the lock-in amplifier for low-noise measurements, an AC light source is needed. The system previously used a sine wave from the lock-in to electronically modulate

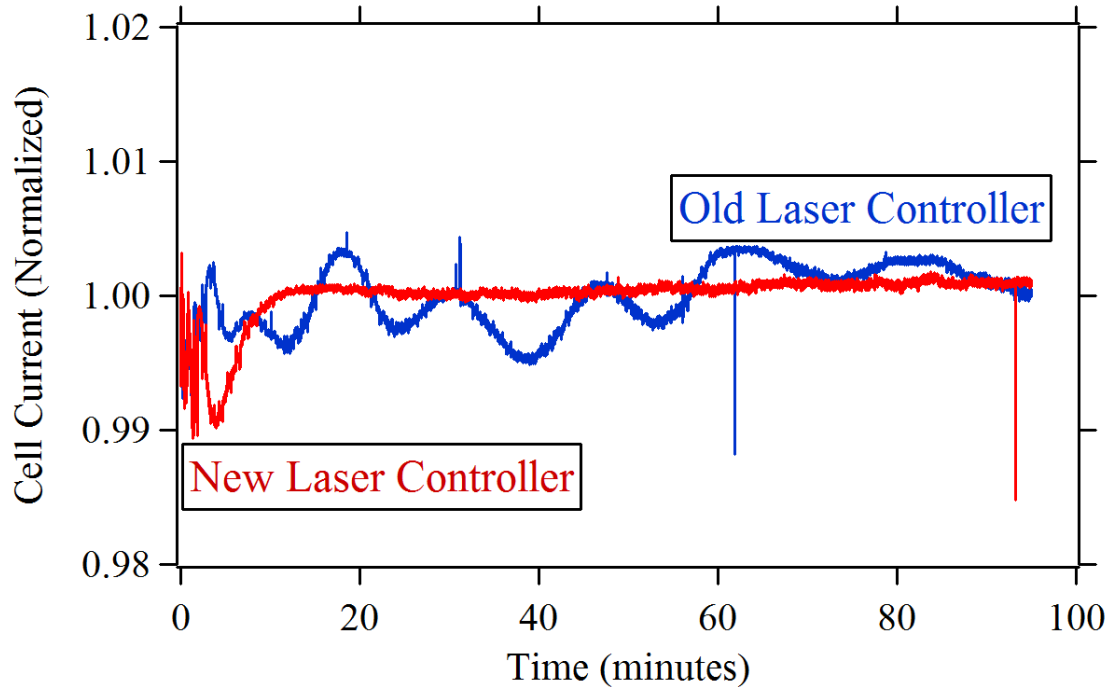


Figure 5.4: Measured cell response over time with old and new laser diode controllers. Measurements were made at a fixed position over 95 minutes.

the current to the laser diode. This method, however, required precise tuning of the laser current to achieve proper waveforms of the output light. More importantly, it was unable to provide a sufficient modulation of the 405 nm laser, as seen in the “Electrically Modulated” scan in Fig. 5.5. The solution was to introduce an optical chopper (SRS SR540). Optical chopping has been avoided at CSU in the past because of the higher-order frequencies introduced by the square wave. This problem, however, is relatively insignificant and is further reduced since the lock-in selects only the lowest-order frequency. The optical chopper has significantly reduced the noise in scans, especially at 405 nm, as seen in the “Mechanically Chopped” scan in Fig. 5.5.

The LBIC system has a beamsplitter and intensity monitor to record laser power. The old system used a photodiode with a homebuilt amplifier and AC measurement using a DAQBoard in the computer. In addition to being incompatible with the computer upgrade, the system did a poor job of tracking and correcting changes in the laser intensity, as seen in

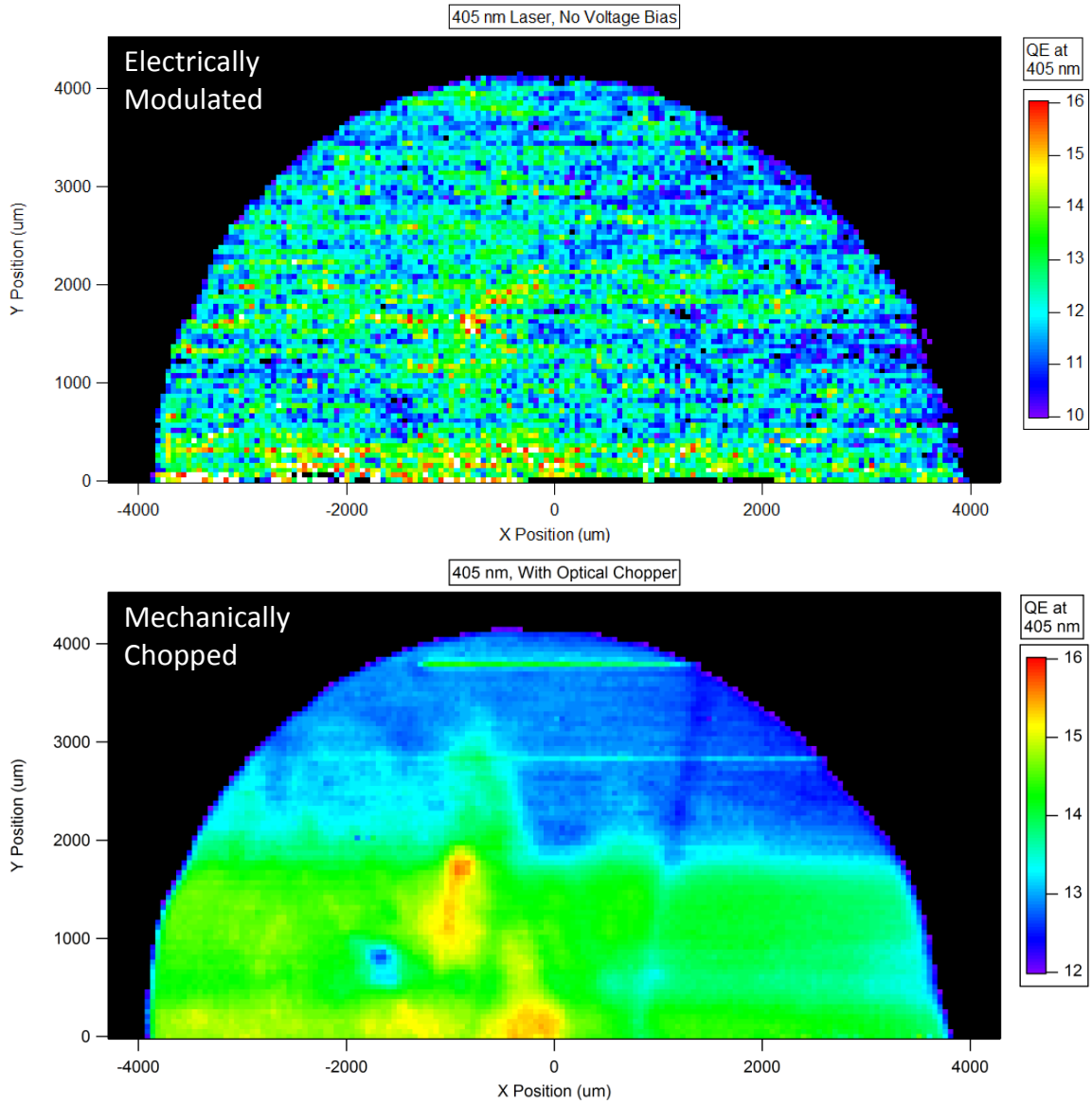


Figure 5.5: LBIC scans of the same area using electrically modulated light (top) and optically chopped light (bottom). Scans were done with 405 nm light, no voltage bias, and 100- μm spot size.

the blue curve of Fig. 5.6. This system was replaced with an amplified photodiode (Thorlabs PDA100A) connected to a multimeter (Chroma 12061). The AC measurement setting of the multimeter took 0.6 s per measurement, which is much slower than desirable for LBIC measurements. The DC setting, by contrast, takes 0.024 s per measurement, which is fast enough. Therefore, the chopper was moved downstream from the beamsplitter, so that the monitor sees only DC light.

The results of these upgrades are shown in the red curve of Fig. 5.6. The upgrades were done in parallel, so their individual effects cannot easily be separated. The cumulative effect, however, is a clear reduction in noise as well as a ratio which tracks within 1% of constant. One potential problem is that the DC sensor will be more sensitive to stray light. To correct for this problem, a tube was added to reduce the solid angle visible to the sensor. This is also an additional reason for leaving the room lights off during measurements.

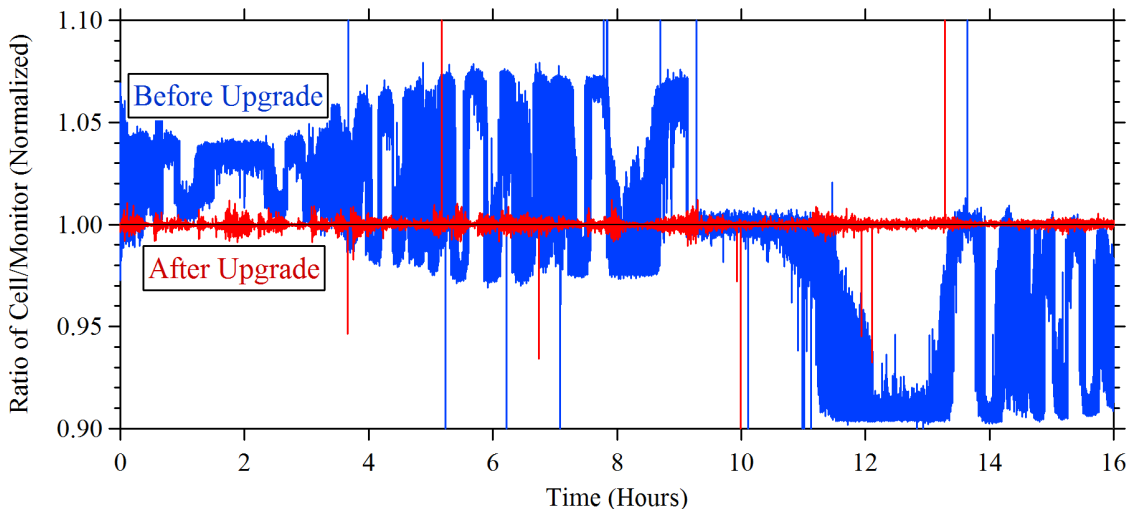


Figure 5.6: Ratio of cell current to monitor voltage, normalized to have an average of 1, before and after system upgrade. Measurements were made at a fixed cell position over 16 hours.

These upgrades together have made significant reductions in the noise of the system. The largest remaining upgrade which could further reduce noise would be a temperature

stability system for the lasers, such as the Thorlabs LM9LP. This should reduce long term fluctuations in laser power and wavelength caused by mode hopping in the laser.

5.1.3 Other Upgrades and Repairs

Various other repairs and upgrades were done to keep the system functioning and providing data well into the future. The attenuator was repaired to fix a damaged input fiber. The stepper motors were replaced, which enabled an upgrade of the computer.

The old stepper motors had needed significant repairs, and were beginning to fail in their calibration and directional control. In addition, they used a computer connection which is unavailable in more modern computers, which had delayed the use of a new computer for the LBIC system. The old computer made normal operation tedious and new software development difficult.

The stepper motors were replaced with Newport CONEX-MFACC stepper motors. These motors had very similar design to the old steppers, but have individual control systems and USB connection which should remain compatible with future computer needs. The computer was replaced with a modern, high-performance computer, and the existing software was transferred to the new computer. Since the new steppers use a different command scheme, pieces of the software which control motion had to be rewritten.

5.2 Software Upgrades

In order to improve the flexibility, functionality, and speed of the LBIC system, two new software tools were developed. The first tool is a program to view data and select areas or lines of interest. The user can either view available data from these areas or lines immediately, or can scan them at higher resolution automatically with the click of a button. The second tool is a way to reduce measurement time using a continuous, rather than a stepped process.

5.2.1 Data Viewer and Sub-Area Selector

A LabView tool for displaying data and selecting areas was developed. A screenshot of the tool is shown in Fig. 5.7. The user first selects a new file to display (a). Since the file format was changed for the fast scan described in Section 5.2.2, the software is able to identify the appropriate format and display the data. The data is displayed in two formats: as an image (b) and as a graph (c). These two formats were chosen because of the built-in LabView tools available for each.

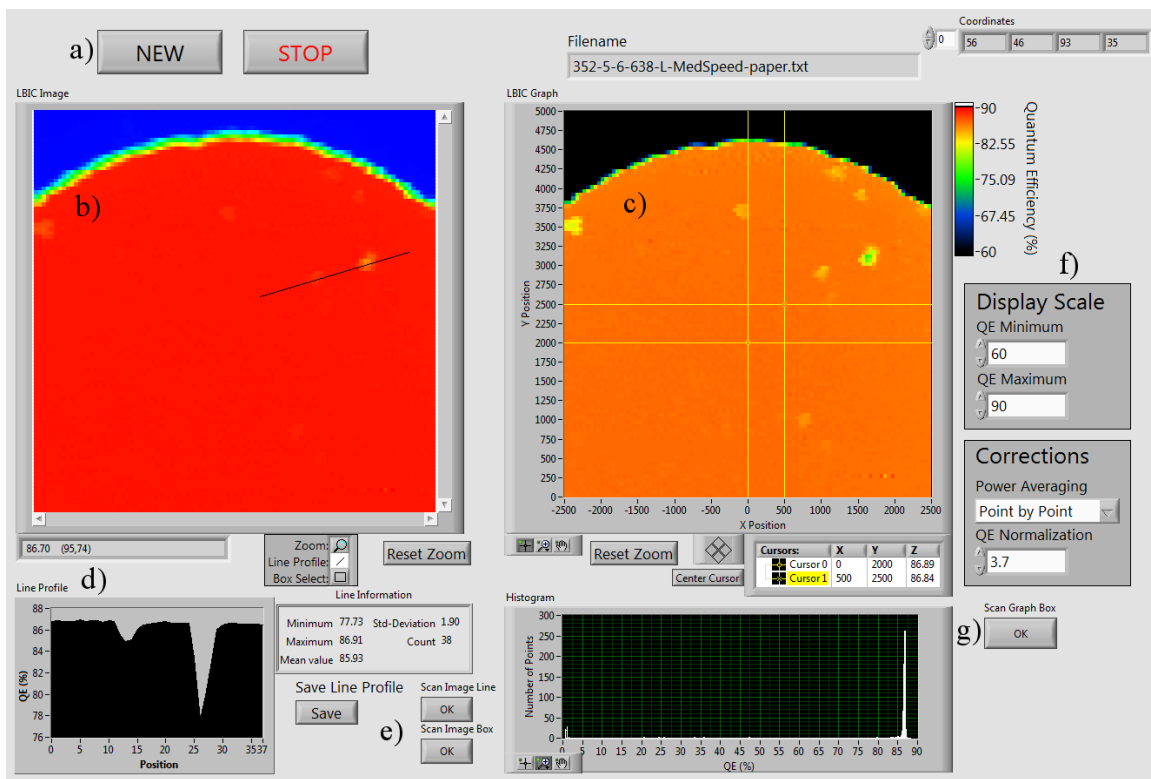


Figure 5.7: Data viewer and area selector. Explanation in text.

The image format (b) has tools available for simple line profile selection, area selection, and zooming. The black line in the image is a line selection. The data contained in this line is shown in the line profile graph (d). The tools at (e) allow the user to save the selected line to a file, to do a linescan of the selected line at higher resolution, or to scan the selected box at higher resolution.

The graph format (c) has better tools available for manipulating the data range and x-y coordinates. The tools at right (f) allow the user to change the display range. This allows the user to emphasize different features. The corrections allow the user to correct for laser power variations through the “Power Averaging” selector, or to correct for calibration errors by normalizing the QE to the correct value. The yellow cursors in the graph can be dragged around to allow the user to select a box, which can be scanned using a button (g). A histogram is also provided to show the uniformity distribution.

The data-viewer and area-selector tools help streamline the process of medium and high resolution scanning. Because they are built into the LBIC control program, no external software is needed to display data. In addition, since the positions of the cursors are calculated automatically and entered into the scan range automatically, the possibility of missing features of interest is avoided, as is any need to write down coordinates for scanning. The ability to view data quickly also makes it useful for sorting through files. The line profile feature provides immediate quantitative information and the option to produce a higher resolution measurement over the desired area, again with a single button click.

5.2.2 Reduced Measurement Time

A common problem with LBIC that has reduced its industrial applicability is the long measurement time. The total time for an LBIC scan is a combination of motion time and measurement time. A procedure has been developed which replaces the stepped measurement process with an on-the-fly, continuous measurement process.

The previous LBIC measurement technique used a discrete process. The system was commanded to a new position, paused until the cell arrived, then took a measurement. This was repeated in a raster pattern over the entire cell. This resulted in motion and wait times as long as 200 ms, in addition to a measurement time of 55 ms. For a typical scan of 10,000 data points, this resulted in scan times of approximately 45 minutes. This procedure is illustrated as the “Stepped Process” in Fig. 5.8 and the results are the 45 minute scan in Fig. 5.9.

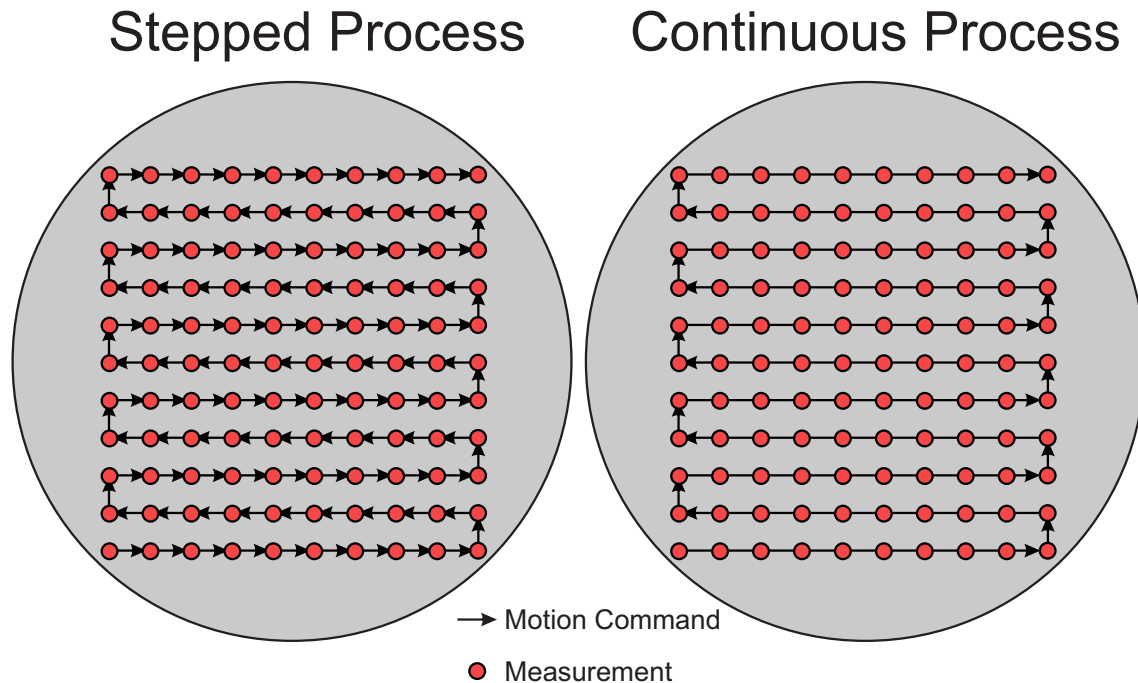


Figure 5.8: Illustration of stepped and continuous LBIC measurement process.

In the continuous process, the system is commanded to move all the way across the cell. As it is moving, measurements are made continuously and as quickly as possible until the motion stops. The raster pattern is the same as in the stepped process, but with only one x and y motion command for each pass. This procedure is illustrated as the “Continuous Process” in Fig. 5.8. For the same 55-ms measurement time, but without the 200-ms wait time, the total scan time for 10,000 data points is reduced to under 10 minutes. The speed of the stepper motors is set such that the motion takes the same time as the measurements. This fit was done empirically. The results are shown as the 10-minute scan in 5.9.

Two permutations of this procedure can be applied. The first is a method of reducing position inaccuracy. The 55 ms measurement time is only an average; the actual time per point can fluctuate by as much as ± 10 ms. This can lead to variations in the spacing of collected data points. To correct for this, a fixed measurement time of 100 ms was introduced

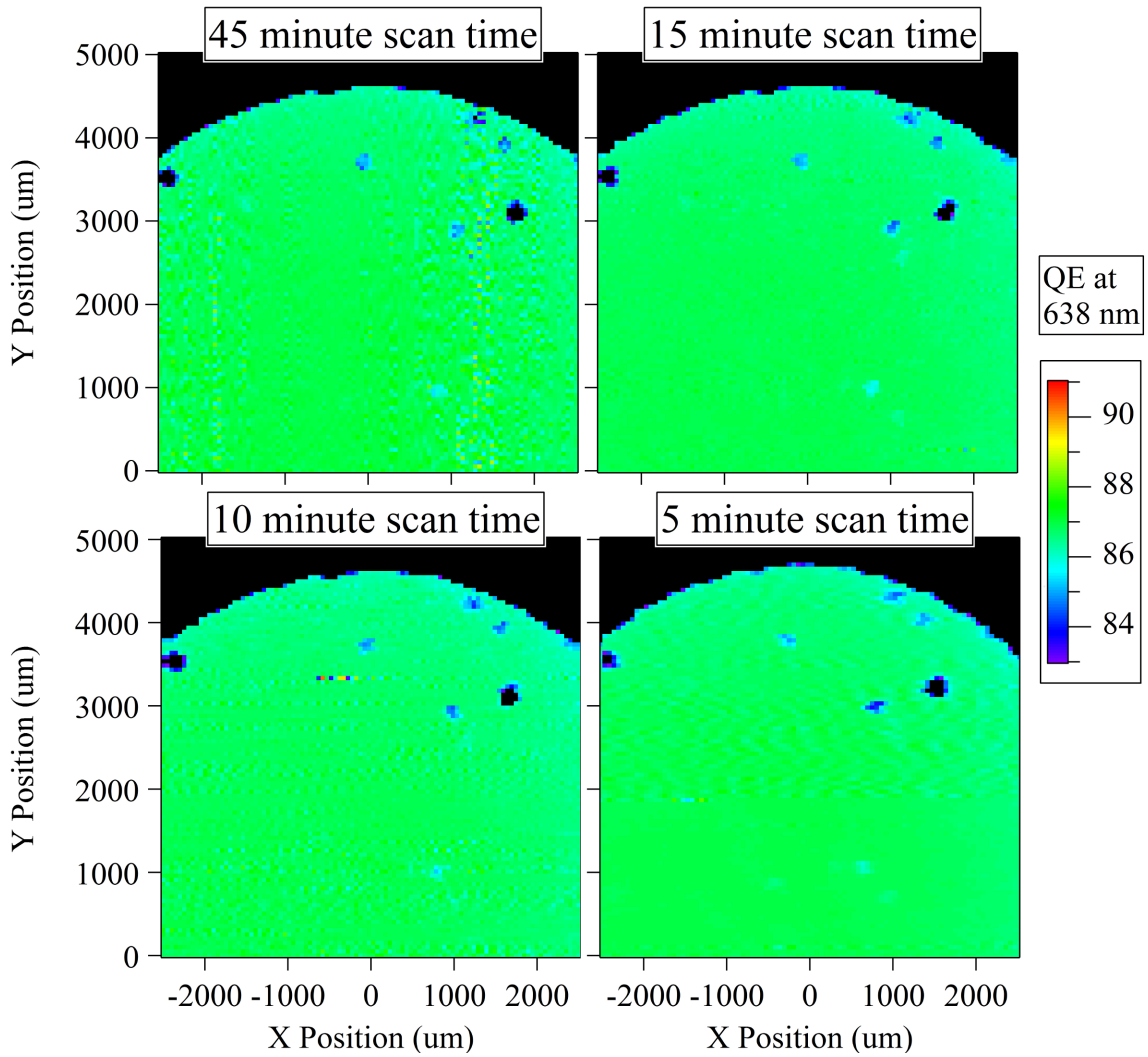


Figure 5.9: Scans of the same area using the stepped process (45 min), fixed-time process (15 min), continuous process (10 min), and manually-corrected reduced-measurement-time process (5 min).

into the procedure. This ensures that the measurements are always equally spaced in both time and position. In addition, the slower total speed reduces nonlinearity in the motion, which further improves the position accuracy. However, the additional time results in scans which take 15 minutes. This is shown as the 15 minute, or fixed-time, scan in 5.9.

A second permutation allows for even faster measurements. A redesign of the code to separate the slowest elements into a parallel slave loop can reduce the measurement time per point to 24 ms, which is the multimeter measurement speed. This has the potential to reduce total measurement time to under 5 minutes. However, the high speed of motion accentuates nonlinearities in the motion, which reduces position accuracy and makes synchronization of the motion and measurement difficult. It can also lead to significant distortion of the final results. The results are shown as the 5 minute, or reduced-measurement-time, scan in 5.9. The distortion had to be manually corrected in this figure. Nevertheless, the 5-min scans may prove very valuable for screening purposes

The continuous process presents no additional challenges for medium or high resolution scanning. Fig. 5.10 shows medium and high resolution scans using the stepped (45 min), fixed-time (15 min) and continuous process (10 min). There are no apparent differences between any of the scans.

There are potential pitfalls with moving to the continuous process to increase the speed, including possible blurring, overdriving the lock-in wait time, and inconsistent spacing. There is also the potential benefit of reduced laser noise.

Since the cell is moving continuously as the measurements are taken, instead of a circular laser spot, the effective laser spot is elongated. This creates the potential for blurring of features. The scans, however, are deliberately designed with overlap of data points, which reduces the concern over blurring. Further, there is no apparent blurring of features in Fig. 5.9, or Fig. 5.10.

The lock-in amplifier is designed with a time constant to reduce output noise by averaging over input noise. This averaging also limits the speed at which the lock-in responds to actual changes in signal. The previous settings were a 10-ms time constant with a 24dB/octave

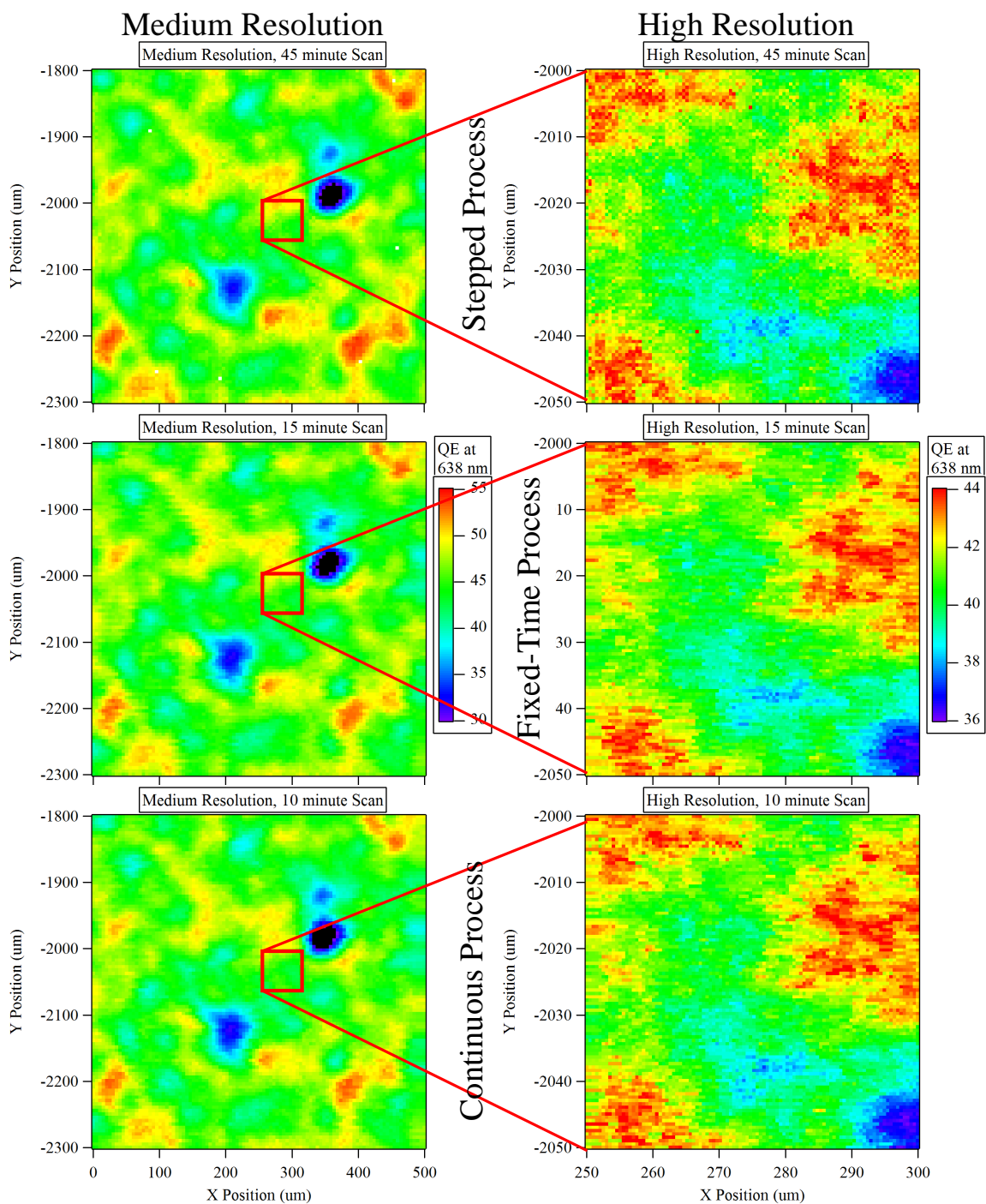


Figure 5.10: Medium- (left column) and high- (right column) resolution scans using the stepped process (45 min, top), fixed-time process (15 min, middle), and continuous process (10 min, bottom).

filter rolloff, as shown in Fig. 5.11a. This requires a 100-ms wait time for full response, which is shorter than the measurement time. Fig. 5.11 shows the results of changing the time constant, filter rolloff, and chopping frequency. All scans were taken with the 10-minute scan time, or 55 ms per point. For the standard frequency, there is no apparent increase in noise by changing the time constant or filter rolloff. The minimum satisfactory reduction should be used, so the 3 ms and 24 dB/oct filter (Fig. 5.11b), which gives a 30-ms response time, is sufficient for the 10 minute scan. The 3 ms and 12 dB/oct (Fig. 5.11b) is necessary for the 5-minute scan, because its 21-ms response is shorter than the 24-ms measurement time. There is no clear advantage to increasing the chopping frequency (Fig. 5.11 d,e,f). Indeed, it seems to increase the noise in most cases. Implementing these changes removes problems with lock-in response without a significant increase in noise.

A final pitfall is inconsistent spacing. Since the position is not checked before measurement, as in the stepped process, there is no expectation that points will be equally spaced, or that passes in opposite directions will align perfectly. The fixed-time procedure addresses the first concern by equally spacing points in time, and thus in position. The alignment also improves at lower motion speeds, but can be corrected for any speed by moving data to align features correctly. Both of these problems can be completely eliminated by storing x and y positions for each measurement point, and using software which graphs a 3 dimensional matrix, rather than an equally-spaced 2 dimensional matrix. Since neither of these problems has proved to be apparent, use of the fixed-time procedure is sufficient.

A potential additional benefit from the reduced scan time is reduced laser noise. The laser can be unstable over long periods of time, which manifests as periods of stability connected by noisy periods. A 45 minute scan will often span multiple stable periods, so that the unstable periods are also included. A shorter scan time is more likely to fall within a stable period, and can be easily repeated if it does not. This can be seen in the laser noise (small blue dots) on the right side of the 45 minute image in Fig. 5.9 and lack of apparent laser noise in the faster scans.

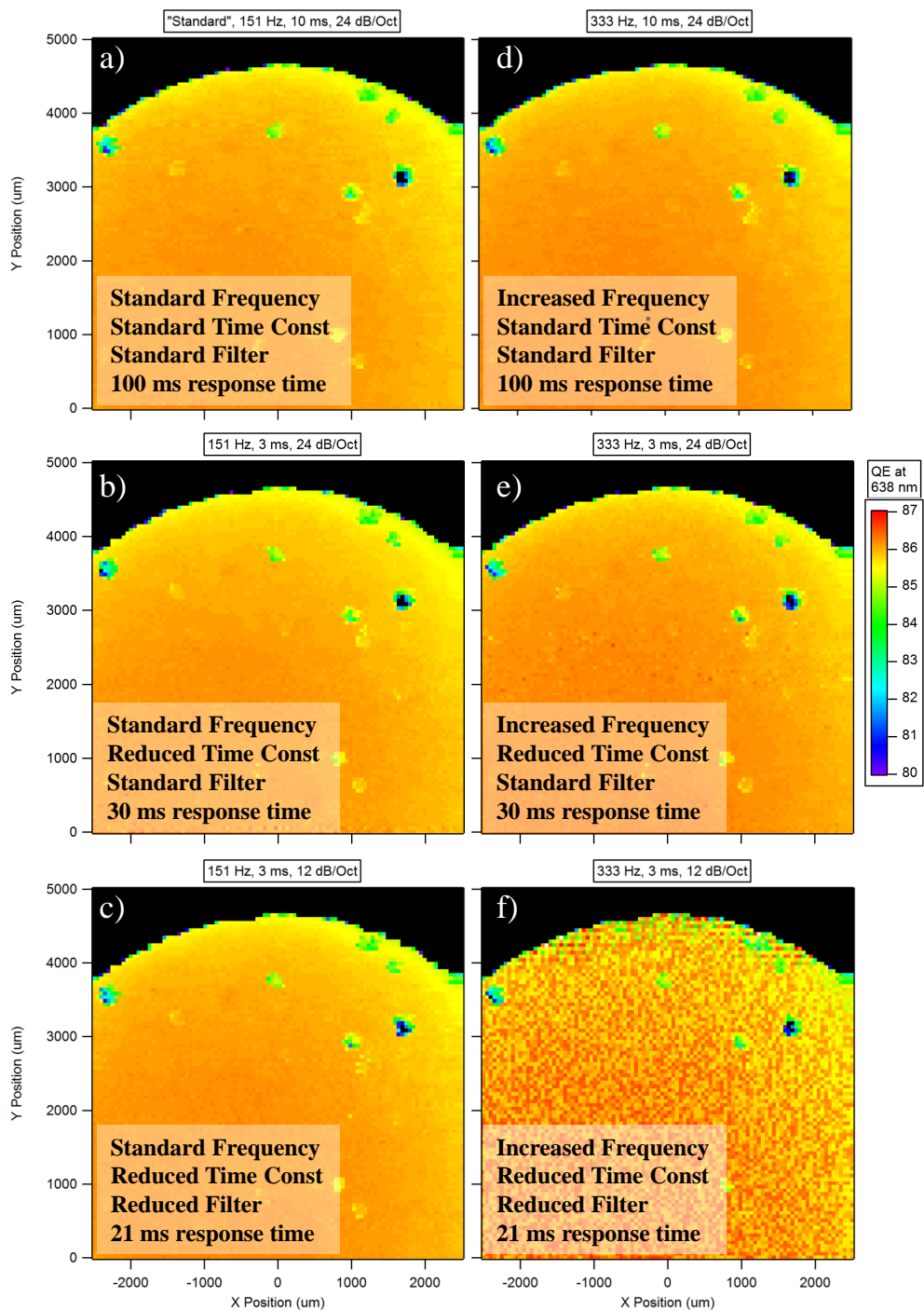


Figure 5.11: Scans of the same area using varying lock-in amplifier parameters and chopping frequencies. Standard settings are 151 Hz, 10 ms, 24 dB/octave. Modified settings are 333 Hz, 3 ms, 12 dB/octave.

Chapter 6

GENERAL STRATEGY FOR NONUNIFORMITY CHARACTERIZATION USING LBIC

Although LBIC is effective at detecting nonuniformities, the ultimate goal is to move beyond detection to characterization and ultimately identification of defects and their causes. For full characterization, a single scan is insufficient. Three LBIC tools which were used in this research to characterize nonuniformities are spectral dependence, voltage bias dependence, and resolution dependence. Fig. 6.1 shows the quantum efficiency for a sample cell at varying voltage biases [50]. The wavelengths used in LBIC are circled.

6.1 Wavelength Dependence

Four primary wavelengths are used in the CSU LBIC system: 405, 638, 830, and 850 nm. These wavelengths were chosen because of their value for measuring CdTe devices, as can be seen in Fig. 6.1. Other wavelengths may be of more value for studying different technologies.

The 405 nm light is primarily beneficial for measuring the window layer, often CdS, as discussed in Section 5.1.1. The light is parasitically absorbed by the CdS, so the 405 nm measurements are primarily a measurement of CdS thickness. It can be used to identify thin regions of CdS, which may cause a reduction in performance at other wavelengths, as was seen in Fig. 5.2.

As can be seen in Fig. 6.1, 638 nm is near the peak response of the cell. The cell response is often relatively flat between the CdS and CdTe bandgap (~ 510 to 830 nm), so the 638 nm response usually represents this region well. In addition, 638 nm is near the peak of the solar spectrum. Since it is in the middle of the visible range and the range of wavelengths used in the LBIC, 638 nm also interacts well with the optical elements chosen for the LBIC. Because of all of these factors, the 638 nm laser is used as the primary wavelength for initial characterization of a cell.

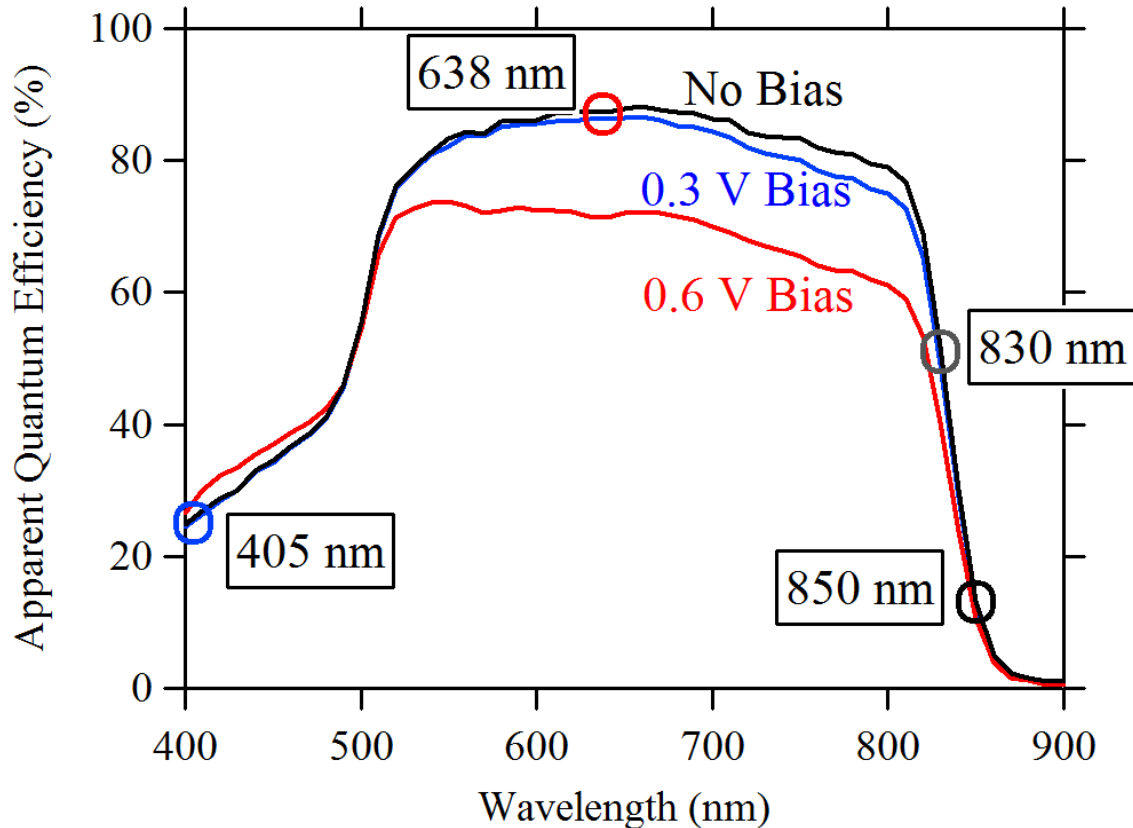


Figure 6.1: QE of sample cell at varying voltage biases. Wavelengths used in LBIC are circled. This cell is used in Figs. 6.2-6.5 and Figs. 6.7-6.9.

830 nm is closer to the band gap of CdTe than 638 nm, so it will tend to be absorbed farther into the CdTe layer. Therefore, it is potentially sensitive to nonuniformities which are farther towards the back of the device. The 830 nm light can also be sensitive to thickness variations in the CdTe, especially for very thin CdTe, under 1 μm .

The 850 nm light is at or beyond the band gap of CdTe. Because it is on a steeply sloping part of the QE curve, it will be more sensitive to lateral shifts in the edge than to vertical shifts. This means that the 850 nm QE is primarily sensitive to changes in the band gap of CdTe. The band gap of the entire layer can shift due to changes in the processing, as can be seen by comparing published QE curves from varying sources, for example Fig. 2 in [51]. However, localized variations can also exist in the band gap. These are often attributed to

sulfur diffusion from the CdS into the CdTe, which results in a lower band gap for small amounts of sulfur [52].

Because the different wavelengths are sensitive to different layers and different types of nonuniformities, the characterization power comes from scanning at all wavelengths, as seen in Fig. 6.2. Due to low laser power, the 405- and 830-nm scans have higher noise. Some features are apparent at some wavelengths, but not at others. Other features have opposite responses at different wavelengths.

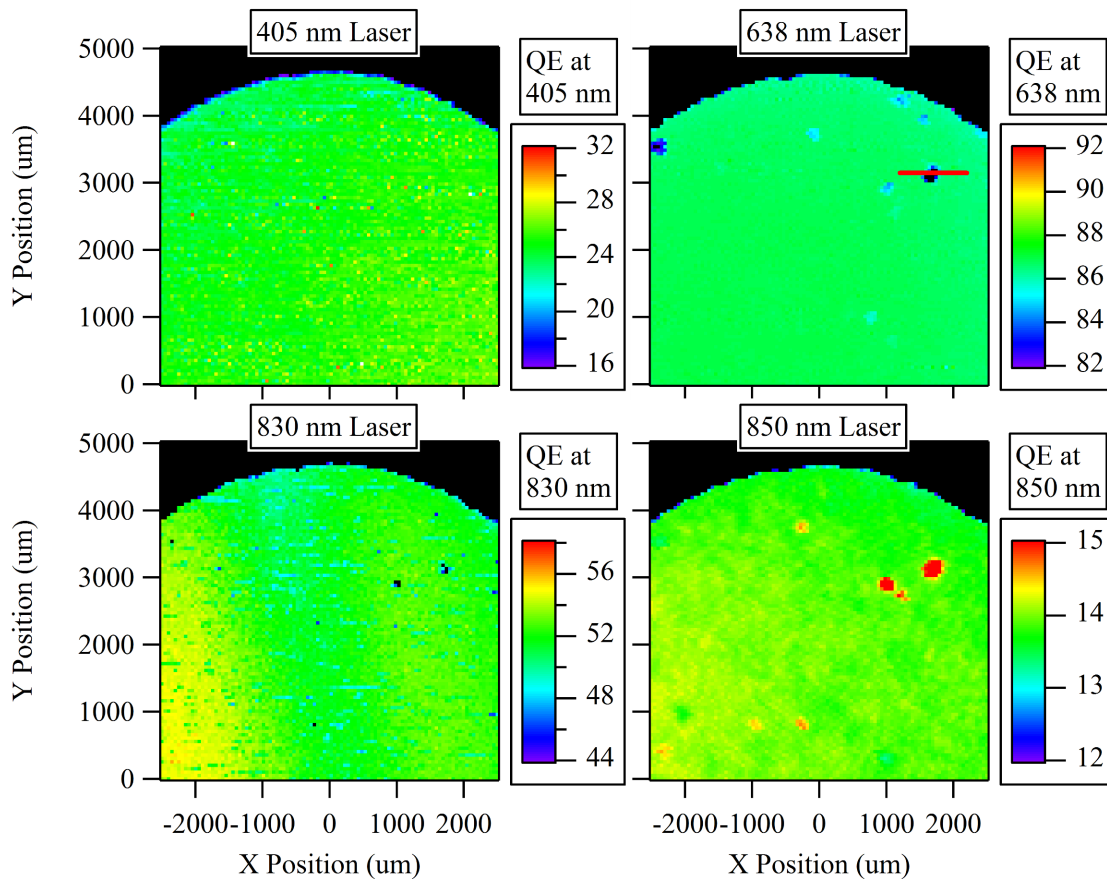


Figure 6.2: LBIC scans of cell at four different wavelengths. The red line in the upper right is shown as a linescan in Fig. 6.3. Scans are with no applied bias and 100- μm spot size.

The line marked in the 638 nm scan of Fig. 6.2 is shown as a line scan in Fig. 6.3. The line scan shows that the feature has reduced QE at 638 and 830 nm, no change at 405 nm,

and increased QE at 850 nm. Since 850 nm is most sensitive to the band gap of CdTe, this is likely an area of sulfur diffusion into the CdTe. A high-sulfur area might also cause electrical issues which reduce the signal. This reduction overwhelms any increase in signal at 830 nm due to a shift in the band gap. Note that the fine structure in the 638-nm scan also appears at 830 nm, suggesting that it is caused by real variations in the response, rather than noise in the signal.

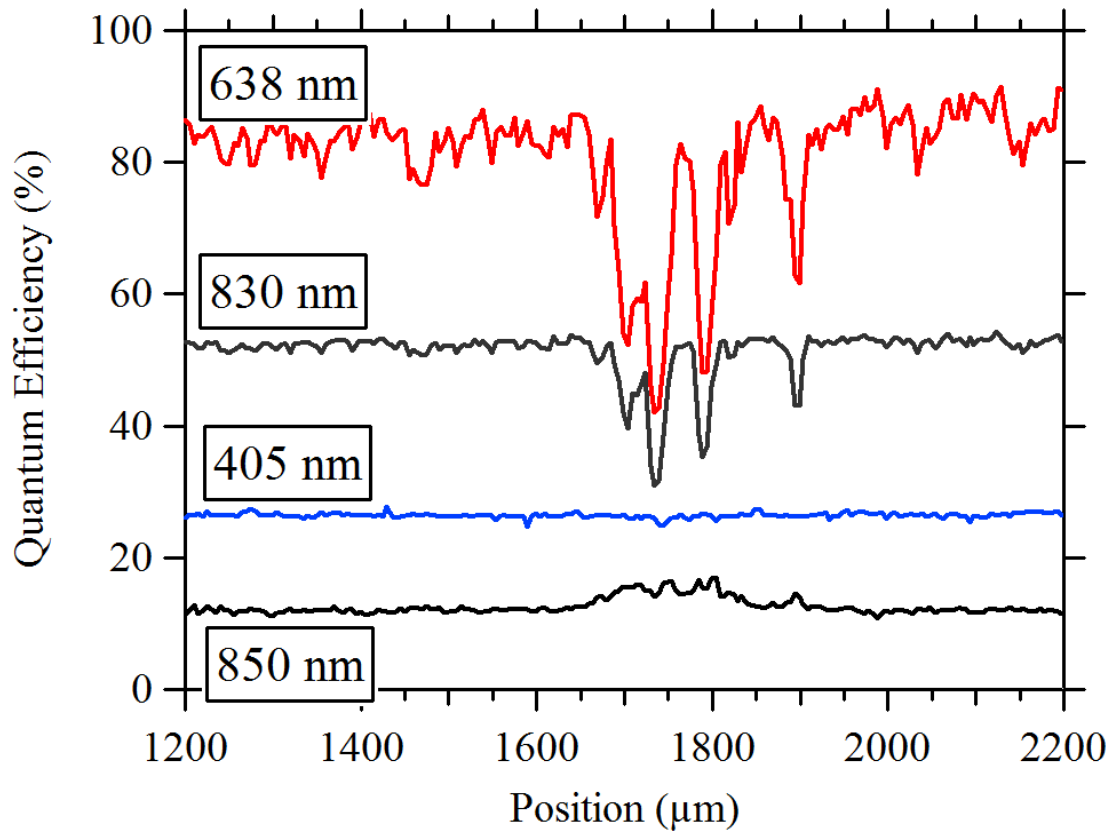


Figure 6.3: Line scans of a nonuniformity using four different wavelengths. Scans are with no applied bias and 10-μm spot size.

Although the four wavelengths in this system are ideal for CdTe cells, a different set of wavelengths could be more beneficial for other materials. The 638 nm will be useful for most materials due to its importance in the solar spectrum. The other wavelengths are highly material dependent, however. If a window layer with a different band gap is used, the 405

nm would need to change to accommodate. Likewise, for a different absorber, wavelengths which are close to the absorber band gap should be used in place of the 830 and 850 nm.

6.2 Voltage Bias Dependence

The measured, or apparent, quantum efficiency (AQE) of a cell is expected to decrease as a forward bias is applied, as can be seen in Fig. 6.1. The change in response, however, can be nonuniform both in space and in wavelength. Regions of weak diodes (high J_0) will have their AQE reduced faster than regions with well-behaved diodes (low J_0). Weak diodes can be caused by problems such as thin CdS or high interface recombination. Series resistance, CdS photoconductivity, and energy band barriers can all have significant impact on quantum efficiency under voltage bias [38].

Figure 6.4 shows LBIC scans of a cell at four different voltage biases: 0.3 V reverse bias, no bias, and 0.3 and 0.6 V forward bias. The nonuniformity clearly increases with increasing forward bias. The uniformity slightly improves with reverse bias. In addition, features appear at far forward bias which are not visible without bias.

Such a feature is shown by the red line in the upper right of Fig. 6.4, and expanded upon as a line scan in Fig. 6.5. This figure shows a line scan of a weak diode region. At zero bias, the feature is small, less than 50 μm , and has a small impact on QE, less than 5%. This feature will likely not appear in a low resolution scan, because it is smaller than the spot size of the laser. At far forward bias, however, the feature grows to nearly 200 μm and has a reduction in AQE of 30%. At 0.8 V, the apparent QE even drops below zero. This is consistent with a weak diode which has passed the V_{oc} point and reduced response over a larger area. Note here as well that the fine structure is consistent between the line scans, suggesting that the variations are real, and not caused by noise.

Fig. 6.6 shows an EL image of half a cell, in combination with LBIC scans at four different wavelengths and three different biases. This figure shows how the combination of wavelength and voltage bias can be very powerful for characterizing nonuniformities. Each scan shows different information, based on the presence, size, and direction of nonuniformities in all

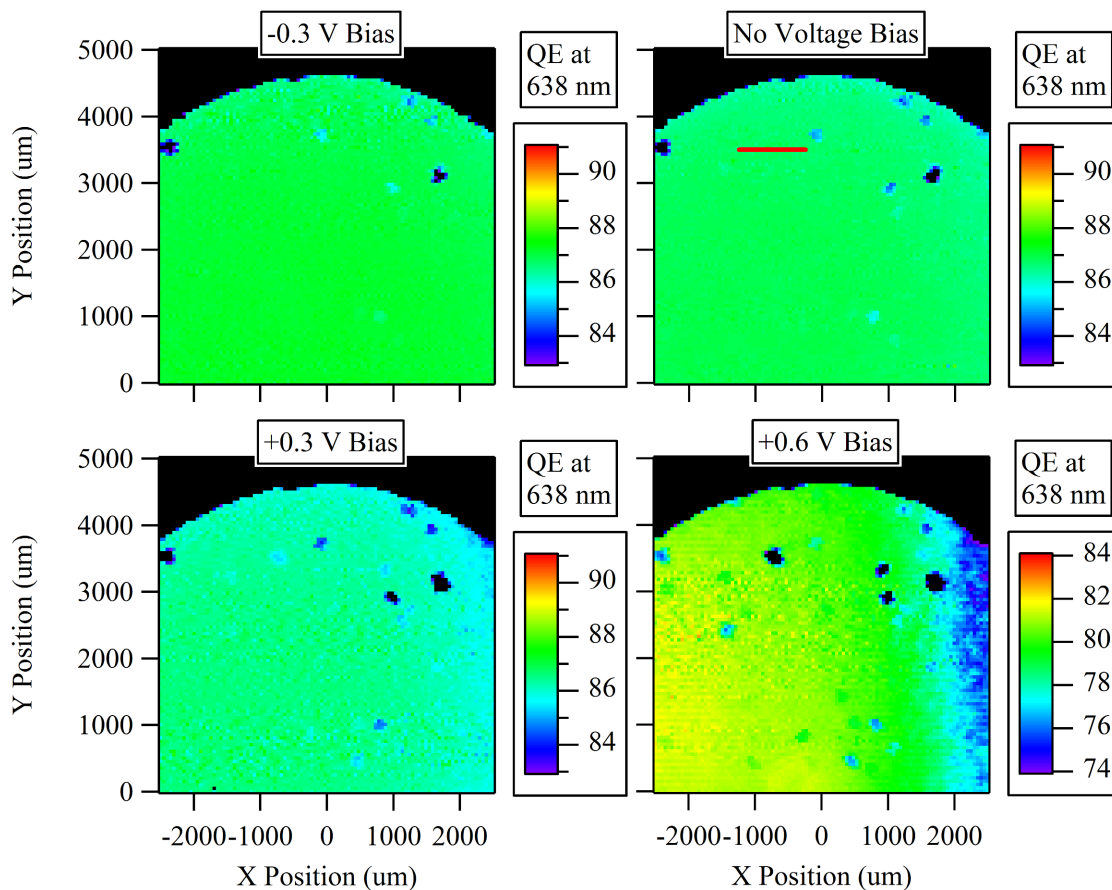


Figure 6.4: LBIC scans of cell at four different voltage biases. The red line in the upper right is shown as a linescan in Fig. 6.5. Scans are at 638 nm and 100- μm spot size.

the different scans. A thin CdS region can be identified from the 405 nm scan, and sulfur diffusion can be identified from the 850 nm scan. The line on the right of most images is likely a scratch in the TCO. The scratch has limited effect at zero bias, but causes an increase in resistance which reduces AQE at forward bias. More signatures from these varied scans could be correlated with physical causes. See Section 6.4 for further discussion of the relationship between EL and LBIC.

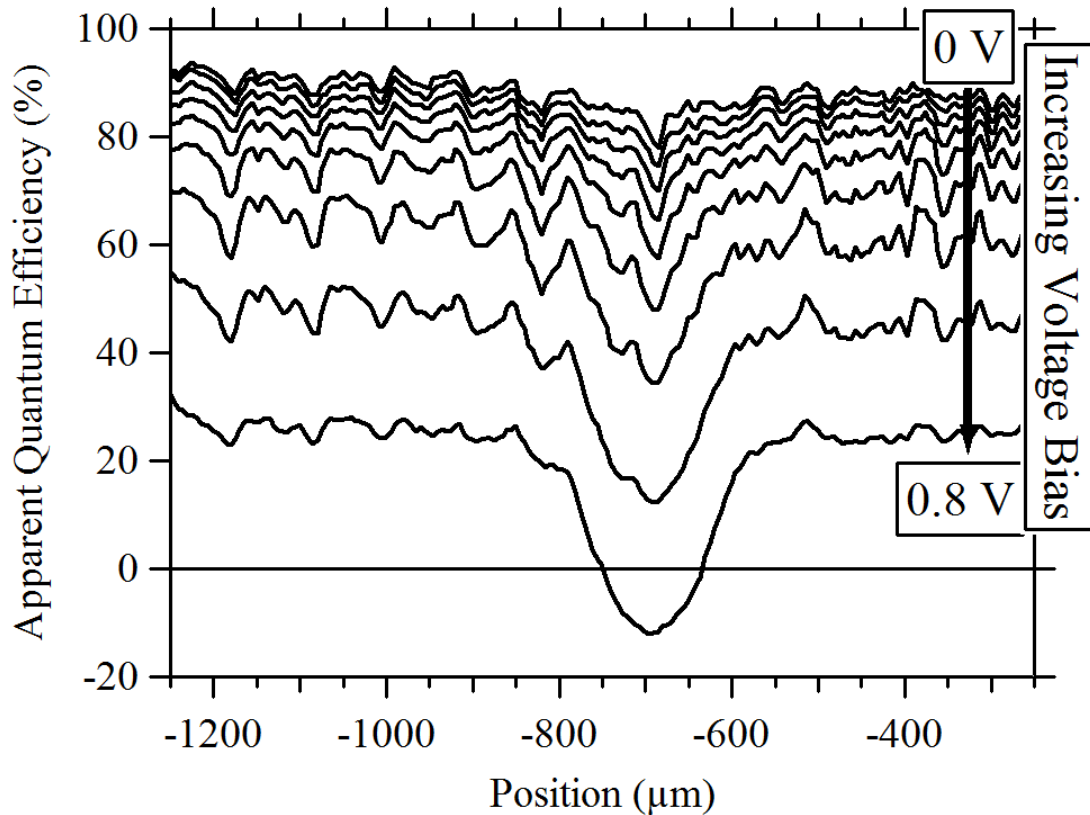


Figure 6.5: Line scans of a nonuniformity at increasing voltage bias. Scans are at 638 nm and 10- μm spot size.

6.3 Resolution Dependence

Since nonuniformities exist on many different scales, it is useful to be able to change resolutions. Three standard resolutions in our system are 100, 10, and 1 μm spot sizes. A standard scan size has been adopted which has a square grid of 10,000 points and a step size which is half of spot size. This makes the standard low-, medium-, and high-resolution scan areas 5000×5000 , 500×500 , and $50 \times 50 \mu\text{m} \times \mu\text{m}$, respectively. The low resolution is a large enough area that it can cover a significant fraction of the cell. If necessary, the full cell can be covered in 30-40 minutes using the fast scanning procedure. The medium resolution is on the scale of many of the defects which are identified by the low resolution scan. The high

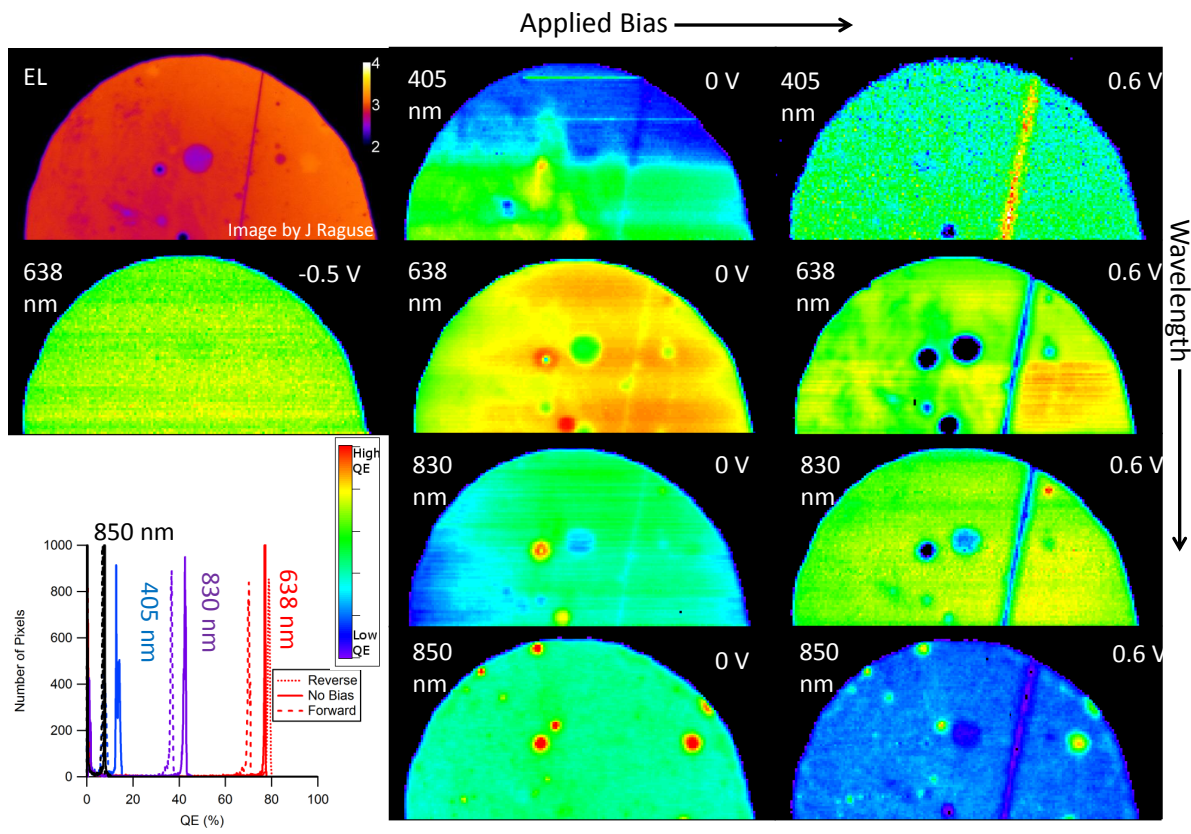


Figure 6.6: EL of half a cell, and LBIC scans of the same area at 4 wavelengths, with three biases. Scales have been removed for space, but the histogram in the lower left shows approximate range for each.

resolution is the limit based on diffraction, and can see many defects which are 10s of μm in size.

Fig. 6.7 shows scans at the three standard resolutions. From the low-resolution scan, we can see that there are nonuniformities distributed around the edge of the cell, but few in the middle. The medium-resolution scan shows a detailed view of one of the nonuniformities, which is also shown as a line scan in Fig. 6.3. The nonuniformity is about $200\ \mu\text{m}$ in diameter and has some interior features, which agrees with the line scan. The high-resolution scan shows that the cell has features which vary in QE by 5-10% and are around $30\ \mu\text{m}$ in size. These features do not show up in the low-resolution scan because they are averaged by the $100\text{-}\mu\text{m}$ spot size.

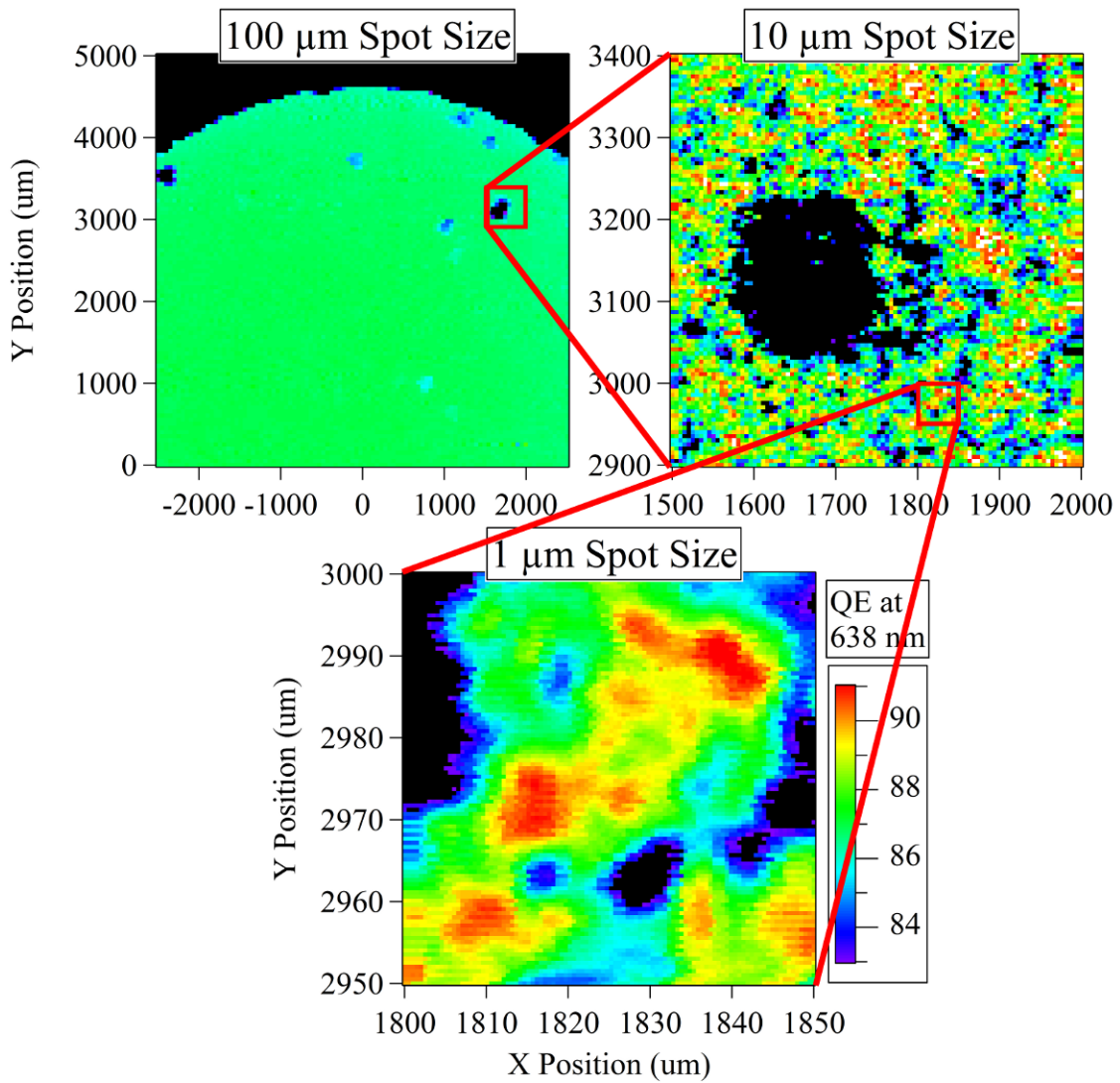


Figure 6.7: LBIC scans at different resolutions: 100, 10, 1 μm spot sizes. Scans are with 638 nm and at no voltage bias.

Typical CdTe grain size is on the order of 1 μm , which is the same as the minimum spot size of the LBIC system. However, in order to resolve within a grain or between different grains, a spot size smaller than the grain size is necessary. One approach to reducing the spot size is using oil-immersed optics [53]. Another approach is near-field scanning optical microscopy [54]. Although both of these can reduce the resolution to 200 nm, both have the drawback of requiring a very small working distance. Since CdTe is in a superstrate configuration, it has a 3 mm piece of glass on top, and an opaque electrode on the back. Thus, a CdTe cell is inaccessible using either of these techniques. Further microscopy techniques, such as electron microscopy or Kelvin probe microscopy require direct access to the semiconductor material. This requires either an unfinished device or a cleaved device. In both cases, it is difficult to connect cell performance at this location to the microscopy results.

6.4 EL and LBIC as Complementary Tools

Electroluminescence (EL) is another uniformity characterization tool. In an EL measurement, the cell is forward biased, which causes light to be emitted with a wavelength near the band gap. A camera takes an image of the light emitted from the cell, usually with a 100 s collection time. Although EL has proved to be a powerful characterization tool by itself [9] [55] [56], a combination of EL and LBIC can be extremely powerful.

Both EL and LBIC provide spatial information, but since they provide different information, they can be combined for added value. One way in which they provide different information is based on where the measurements operate on the cell's J-V curve. Fig. 6.8 shows dark and light J-V curves for a cell. EL operates in forward bias (usually chosen as 40 mA/cm²) in the dark, while LBIC operates in the light, either at no bias or forward bias (often 0.6 V). Forward-bias LBIC tends to produce more similar features to EL than no-bias LBIC, since both are operating at forward bias [57]. EL intensity has been shown to be exponentially related to open-circuit voltage [9], while LBIC is directly related to short-circuit current.

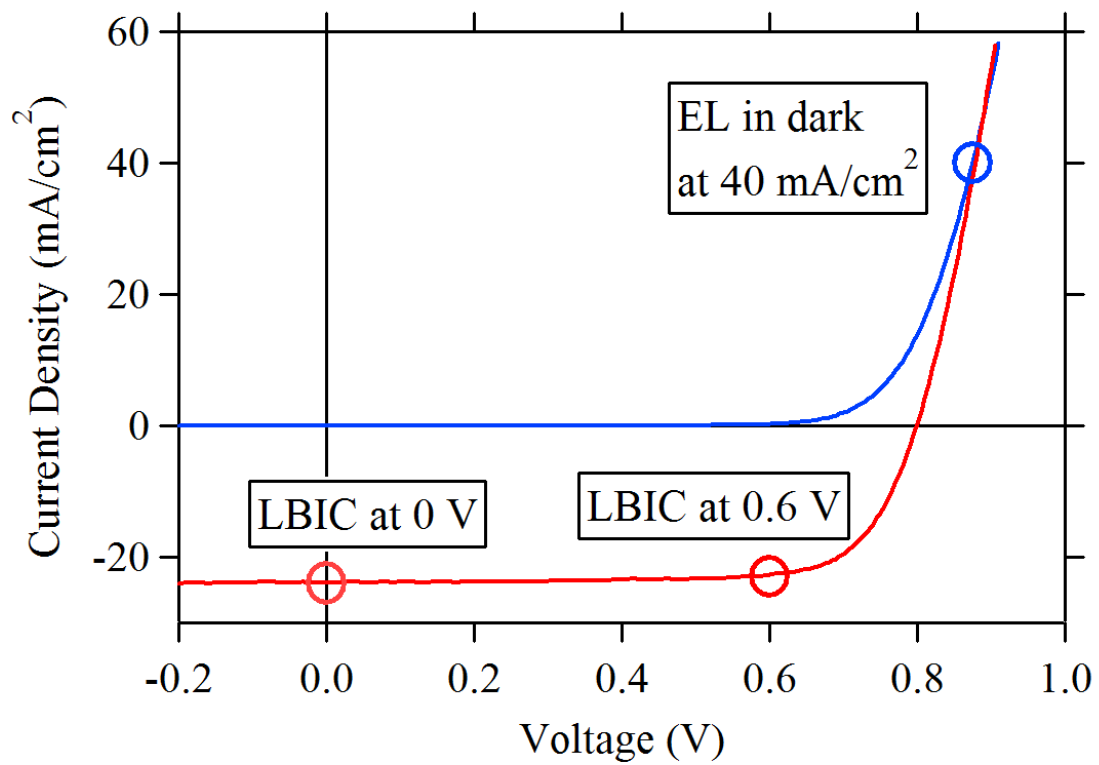


Figure 6.8: Light and dark J-V curves. Circles show current and voltage values where EL images and LBIC scans are measured.

One powerful way of combining EL and LBIC is to use EL for screening large numbers of cells, followed by in-depth characterization of particular cells or nonuniformities using LBIC. EL imaging time is short compared with LBIC and is independent of area. An EL image can be collected in 100 seconds, while an LBIC scan of an entire cell, even at the fastest setting, takes 20 minutes. EL can thus be used for selection of cells which have interesting features or merit further study. However, since there are few parameters to vary in EL, it is difficult to use EL for detailed characterization of these features. Instead, LBIC can be used as described above for spectral-, voltage-bias-, and resolution-based characterization of the cell. When combined in this manner, EL and LBIC are a powerful spatial characterization suite, as will be shown in examples below.

Fig. 6.9 shows a comparison between EL and LBIC measurements, where the LBIC is done both without and with bias. The feature directly above the number 1 was studied in Fig. 6.3 and the medium-resolution scan of Fig. 6.7. This feature is both apparent in the EL, and has the complicated interior structure seen in medium-resolution LBIC. The feature directly above the number 2 was examined in Fig. 6.5. This is an example of the closer overlap between EL and forward-bias LBIC than between EL and no-bias LBIC. Since this feature appears at forward bias, but not at zero bias, it does not have significant impact on current, but only on voltage.

Fig. 6.10 shows EL and LBIC being used together to explore how addition of different metal halides to the CdCl_2 passivation affects cell uniformity [58]. EL was measured on many samples by J. Raguse, and a small set was chosen for LBIC study. For both treatments, there is close agreement between EL and forward-bias LBIC. With 850 nm light, however, there is little agreement between EL and LBIC for the MgCl_2 -passivated cell. In contrast, there is strong overlap between the 850-nm LBIC and the EL for the MnCl_2 -passivated cell. Although the features appear in both, however, they move in opposite directions; the features have lower EL response but higher 850-nm QE response. This suggests that the MnCl_2 is affecting the bandgap of the CdTe, while the MgCl_2 is not.

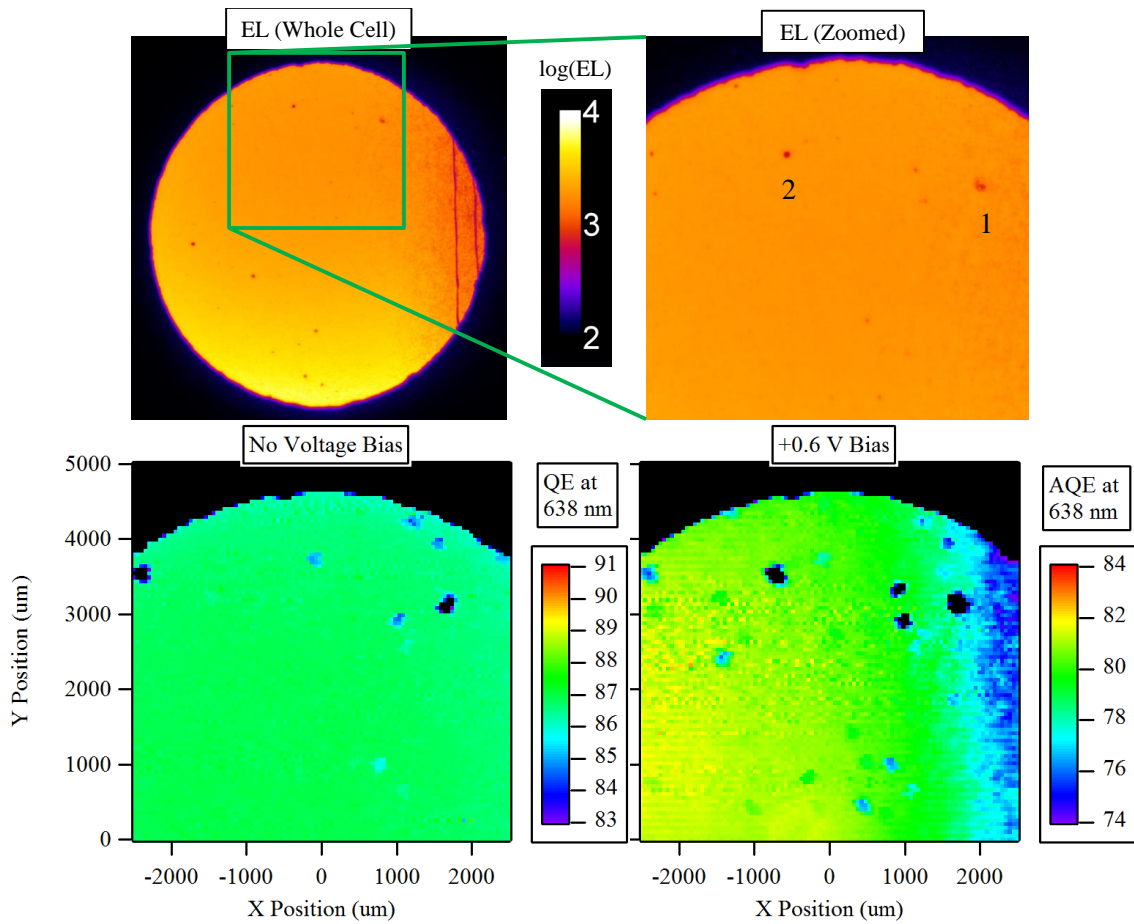


Figure 6.9: EL images and LBIC scans of the same area. EL images are shown on a logarithmic scale. Upper left shows EL of the full cell, while upper right shows the area measured in LBIC. LBIC scans are taken from Fig. 6.4.

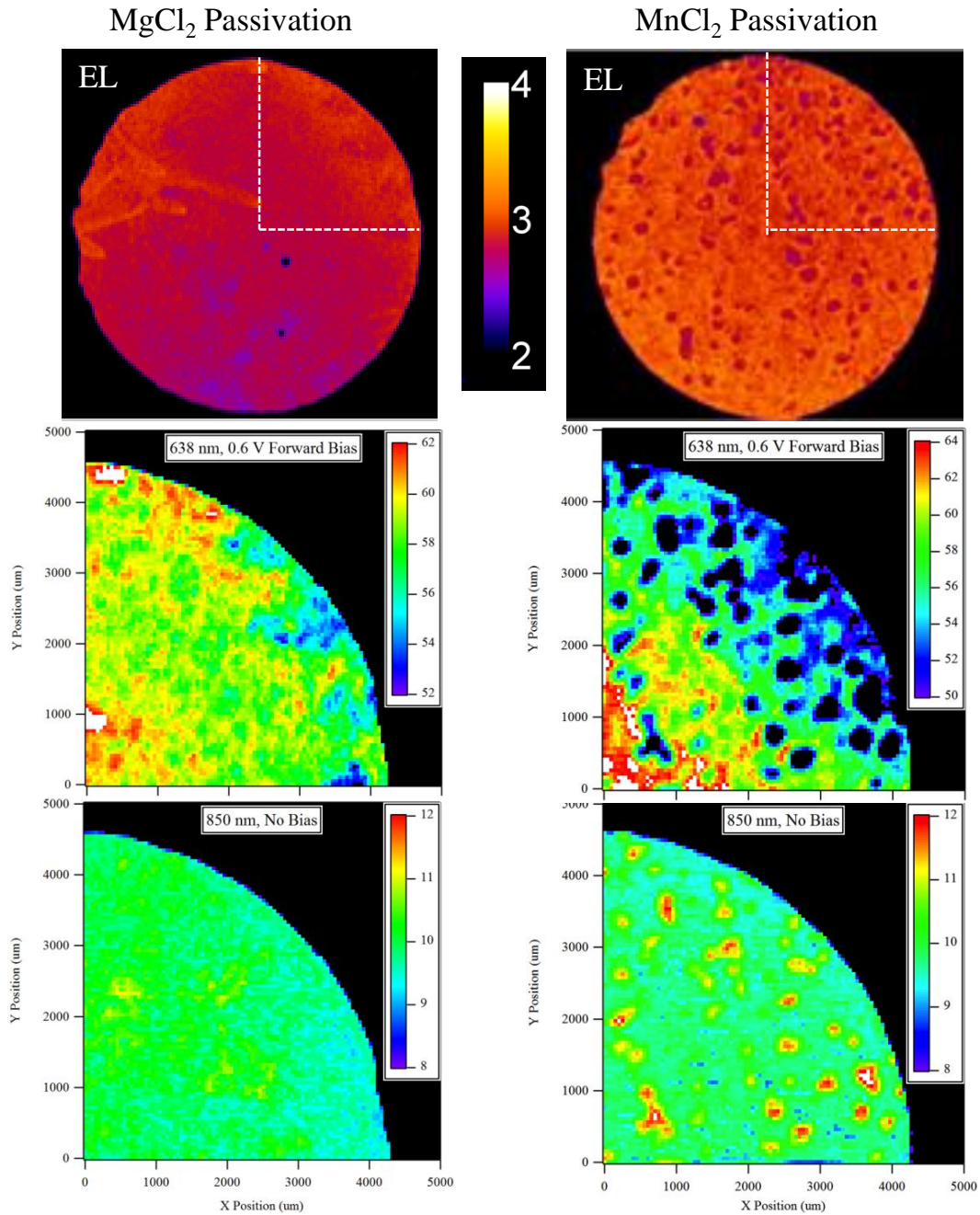


Figure 6.10: EL images (log scale, taken by J. Raguse) and LBIC scans for cells with different passivation treatments, MgCl_2 in the left column, MnCl_2 in the right. EL images (top row) are shown on a logarithmic scale. LBIC is done with 638 nm and 0.6 V bias (middle row) and 850 nm and no bias (bottom row).

Chapter 7

CONCLUSIONS

Thin-film photovoltaics have the potential to make a large impact on the world energy supply. They can provide clean, affordable energy for the world. Understanding the device physics and behavior will enable increases in efficiency which will increase their impact. This work presented novel approaches for evaluating efficiency, as well as a set of tools for in-depth whole-cell and uniformity characterization.

The understanding of efficiency losses is essential for reducing or eliminating the losses. The efficiency can be characterized by a breakdown into three categories: solar spectrum, optical, and electronic efficiency. For several record devices, there is little difference in the solar spectrum efficiency, modest difference in the optical efficiency, and large difference in the electronic efficiency. This suggests that there is the most room for improvement in the electronic efficiency.

The losses within each category can also be further characterized. The losses due to the broad solar spectrum and finite temperature are well understood from a thermodynamic physics perspective. Optical losses can be fully characterized using quantum efficiency and optical measurements. Losses in fill factor can be quantified from series and shunt resistance, as well as the expected fill factor from the measured V_{oc} and A . Open-circuit voltage losses are the most significant, but are also be the hardest to understand, as well as the most technology-dependent.

The tools presented for efficiency analysis are all technology independent, which is beneficial for a general framework. To probe deeper into specific losses, a specific technology must be used. The rest of the work focused on analysis of CdTe devices, as well as improvements to the tools used for characterizing CdTe solar cells.

Characterization of the whole cell helps to understand the behavior, performance, and properties of the cell. It is important that the characterization be as thorough and accurate

as possible. To this end, improvements were made to the calibration and hardware of the measurement systems. Additional area measurement and accelerated stress tools were also developed and implemented.

Several different tools can be used for whole-cell characterization, including current-voltage, quantum efficiency, and capacitance measurements. Each of these tools give specific information about the behavior of the cell. When combined, they can lead to a more complete understanding of the cell performance, than when taken individually.

These tools were applied to several specific CdTe experiments. They have helped to characterize the baseline performance of both the deposition tool and the measurement systems. Characterization of plasma-cleaned cells showed an improvement in performance, even at thinner CdS layer thickness. Measurements of thinning CdTe samples revealed additional optical losses, likely caused by the increasing importance of the back diode. Characterization of Cd(S,O) devices showed improved performance, both from improved optical and band alignment properties. They also provide insight into a way to higher efficiency.

Uniformity can have an effect on whole-cell performance, but can also be an important parameter to characterize on its own. Light-beam-induced current is a powerful tool for characterizing uniformity. The LBIC tool was upgraded to improve its accuracy, functionality, and speed. A 405 nm laser was added, which enables characterization of the uniformity of the CdS window layer. The accuracy was improved significantly through a series of hardware upgrades. The speed was improved by replacing the stepped measurement process with a continuous measurement process. This reduced the measurement time over a standard area from 45 minutes to 10 minutes with no apparent loss of accuracy.

The improved LBIC system aids in the collection of uniformity data. A number of parameters can be varied to provide in-depth uniformity information and help identify causes of nonuniformity. The wavelength can be varied to provide information on different layers. This can help identify variations in CdS thickness and local CdTe band gap. An applied voltage bias can be used to identify locations with weak diode properties. The resolution can

also be varied to provide information on nonuniformities at different scales, from variations across the whole cell to variations on the size of several grains.

LBIC can also be paired with electroluminescence to create a powerful nonuniformity characterization suite. EL is fast and scales easily with area, but does not provide the in-depth information of LBIC. The two can be paired, with EL used as a screening tool to identify cells or areas which need further characterization. LBIC can then be used to characterize and identify the causes of specific nonuniformities.

Future work could be done in all of these areas. In both the efficiency analysis, and whole-cell characterization, further work should be done to connect cell performance with the specific mechanisms which limit efficiency. To better understand limitations in V_{oc} , especially for CdTe, it may be better to start from idealized systems and work towards realistic systems, rather than the reverse order which has been the task so far. This fits well with the simulation work which is being done to understand defects, doping, and recombination mechanisms in CdTe. Another approach is to use single-crystal CdTe with very few defects, and introduce defects in a controlled manner. The penultimate goal would be a quantification of losses as was done for crystalline silicon in Fig. 3.6. The ultimate goal would be to then eliminate those losses and move towards the efficiency limit.

For the LBIC system, a number of further upgrades could improve the performance of the system. The noise can always be further reduced. One prime candidate would be temperature control for the laser diodes, which should improve laser stability. The measurement algorithm could also be optimized to further increase the speed and accuracy of the continuous measurement process. I believe that the algorithm could be improved to the point that a standard area could be covered in 5-6 minutes with no loss of accuracy by correcting for the distortion which is now present at the highest scan speeds.

Further work could also be done to identify the signatures of various sources of nonuniformity. Fig. 6.6 alone presents several different signatures which could be investigated in further detail. Further measurement tools, such as photoluminescence and lock-in thermography may improve the ability to identify nonuniformities [59]. This may, however be a

case of diminishing returns, as the most detrimental nonuniformities are identified and eliminated. That point is likely far down the road, however, and huge gains may be possible by eliminating the worst nonuniformities immediately.

A large body of future work would be to evaluate the connection between uniformity and whole-cell performance. This could be done by quantifying nonuniformity for many cells, and determining the correlation between nonuniformity and any of several device parameters. This could be done across all of the uniformity tools and the whole-cell tools, creating a very large parameter space to compare. Understanding which uniformity and performance parameters do or do not correlate could provide great insight into the link between uniformity and performance.

Bibliography

- [1] U.S. Energy Information Administration. International energy outlook 2013, July 2013.
- [2] Intergovernmental Panel on Climate Change. Climate change 2014: Impacts, adaptation, and vulnerability, March 2014.
- [3] D. Abbott. Keeping the energy debate clean: How do we supply the world’s energy needs? *Proceedings of the IEEE*, 98(1):42–66, Jan 2010.
- [4] First Solar. Utility-scale generation. <http://www.firstsolar.com/en/solutions/utility-scale-generation>.
- [5] M.J. (Mariska) de Wild-Scholten. Energy payback time and carbon footprint of commercial photovoltaic systems. *Solar Energy Materials and Solar Cells*, 119(0):296 – 305, 2013. Thin-film Photovoltaic Solar Cells.
- [6] Martin A. Green, Keith Emery, Yoshihiro Hishikawa, Wilhelm Warta, and Ewan D. Dunlop. Solar cell efficiency tables (version 43). *Progress in Photovoltaics: Research and Applications*, 22(1):1–9, 2014.
- [7] Antonio Luque and Steven Hegedus, editors. *Handbook of Photovoltaic Science and Engineering*. Wiley, 2011.
- [8] D. E. Swanson, R. M. Geisthardt, J. T. McGoffin, J. D. Williams, and J. R. Sites. Improved CdTe solar-cell performance by plasma cleaning the TCO layer. *IEEE Journal of Photovoltaics*, 3(2):838–842, 2013.
- [9] John M. Raguse, J. Tyler McGoffin, and James R. Sites. Electroluminescence system for analysis of defects in CdTe cells and modules. In *38th IEEE Photovoltaics Specialist Conference*, 2012.

- [10] D. M. Chapin, C. S. Fuller, and G. L. Pearson. A new silicon p-n junction photocell for converting solar radiation into electrical power. *Journal of Applied Physics*, 25(5):676–677, 1954.
- [11] Greg Wilson and Keith Emery. Best research-cell efficiencies. http://commons.wikimedia.org/wiki/File:Best_Research-Cell_Efficiencies.png.
- [12] William Shockley and Hans J. Queisser. Detailed balance limit of efficiency of p-n junction solar cells. *Journal of Applied Physics*, 32(3):510–519, 1961.
- [13] Martin A. Green. *Solar Cells*. Prentice-Hall, 1982.
- [14] Raffi Garabedian. First solar 2014 analyst meeting technology update, March 2014.
- [15] Markus Gloeckler. Progress towards practical cdte solar modules with 17% efficiency. In *European Materials Research Society Spring Meeting*, 2014.
- [16] Panasonic HIT solar cell achieves world’s highest energy conversion efficiency of 25.6% at research level. http://news.panasonic.net/stories/2014/0416_26881.html, April 2014.
- [17] A. De Vos, J. E. Parrott, P. Baruch, and P. T. Landsberg. Bandgap effects in thin-film heterojunction solar cells. In *12th European Photovoltaic Solar Energy Conference*, 1994.
- [18] Martin A. Green. Radiative efficiency of state-of-the-art photovoltaic cells. *Progress in Photovoltaics: Research and Applications*, 20(4):472–476, 2012.
- [19] S. H. Demtsu and J. R. Sites. Effect of back contact barrier on thin-film CdTe solar cells. *Thin Solid Films*, 510:320–324, 2006.
- [20] Jun Pan, Markus Gloeckler, and James R. Sites. Hole current impedance and electron current enhancement by back-contact barriers in CdTe thin film solar cells. *Journal of Applied Physics*, 100(12):124505, 2006.

- [21] T. Song, J. Tyler McGoffin, and J.R. Sites. Interface-barrier-induced j–v distortion of CIGS cells with sputtered-deposited Zn(S,O) window layers. *IEEE Journal of Photovoltaics*, PP(99):1–6, 2014.
- [22] Martin A. Green, Keith Emery, Yoshihiro Hishikawa, Wilhelm Warta, and Ewan D. Dunlop. Solar cell efficiency tables (version 42). *Progress in Photovoltaics: Research and Applications*, 21(5):827–837, 2013.
- [23] Martin A. Green, Keith Emery, Yoshihiro Hishikawa, Wilhelm Warta, and Ewan D. Dunlop. Solar cell efficiency tables (version 40). *Progress in Photovoltaics: Research and Applications*, 20(5):606–614, 2012.
- [24] Albert Polman and Harry A. Atwater. Photonic design principles of ultrahigh-efficiency photovoltaics. *Nature Materials*, 11:174–177, 2012.
- [25] Louise C. Hirst and Nicholas J. Ekins-Daukes. Fundamental losses in solar cells. *Progress in Photovoltaics: Research and Applications*, 19(3):286–293, 2011.
- [26] O. D. Miller, E. Yablonovitch, and S. R. Kurtz. Strong internal and external luminescence as solar cells approach the Shockley-Queisser limit. *IEEE Journal of Photovoltaics*, 2(3):303–311, July 2012.
- [27] Uwe Rau. Reciprocity relation between photovoltaic quantum efficiency and electroluminescent emission of solar cells. *Physical Review B: Condensed Matter and Materials Physics*, 76(8):085303, 2007.
- [28] Eric S. Toberer, Adele C. Tamboli, Myles Steiner, and Sarah Kurtz. Analysis of solar cell quality using voltage metrics. In *38th IEEE Photovoltaic Specialists Conference*, 2012.
- [29] Richard M. Swanson. Approaching the 29% limit efficiency of silicon solar cells. In *31st IEEE Photovoltaic Specialists Conference*, 2005.

- [30] R. Scheer. Activation energy of heterojunction diode currents in the limit of interface recombination. *Journal of Applied Physics*, 105:104505, 2009.
- [31] Jason M. Kephart, Russell M. Geisthardt, and W. S. Sampath. Optimization of CdTe thin-film solar cell efficiency using a sputtered, oxygenated CdS window layer. *Progress in Photovoltaics: Research and Applications*, Submitted.
- [32] National Renewable Energy Laboratory. Simple model of the atmospheric radiative transfer of sunshine (SMARTS). <http://www.nrel.gov/rredc/smarts/>.
- [33] Matic Herman, Marko Jankovec, and Marko Topič. Optimal I-V curve scan time of solar cells and modules in light of irradiance level. *International Journal of Photoenergy*, 2012:151452, 2012.
- [34] John Raguse, Russell Geisthardt, Jennifer Drayton, and James R. Sites. Compact accelerated life testing with expanded measurement suite. In *40th IEEE Photovoltaic Specialists Conference*, 2014.
- [35] G. Stollwerck and J. R. Sites. Analysis of CdTe back-contact barriers. In *13th European Photovoltaic Solar Energy Conference*, 1995.
- [36] Galymzhan T. Koishiyev, James R. Sites, Sachin S. Kulkarni, and Neelkanth G. Dhere. Determination of back contact barrier height in $\text{Cu}(\text{In,Ga})(\text{Se,S})_2$ and CdTe solar cells. In *33rd IEEE Photovoltaic Specialists Conference*, 2008.
- [37] Timothy J. Nagle. *Quantum Efficiency as a Device-Physics Interpretation Tool for Thin-Film Solar Cells*. PhD thesis, Colorado State University, 2007.
- [38] M. Gloeckler and J. R. Sites. Quantum efficiency of CdTe solar cells in forward bias. In *19th European Photovoltaic Solar Energy Conference*, pages 1863–1866, 2004.
- [39] P. K. Johnson, A. O. Pudov, J. R. Sites, K. Ramanathan, F. S. Hasoon, and D. E. Tarrant. Comparison of trap states between CIGSS/CdS/ZnO and Cd PE CIGSS/ZnO cells. In *17th European Photovoltaic Solar Energy Conference*, 2001.

- [40] John H. Schofield. Effect of series resistance and inductance on solar cell admittance measurements. *Solar Energy Materials & Solar Cells*, 37:217–233, 1995.
- [41] Jian V. Li, Adam F. Halverson, Oleg V. Sulima, Shubhra Bansal, James M. Burst, Teresa M. Barnes, Timothy A. Gessert, and Dean H. Levi. Theoretical analysis of effects of deep level, back contact, and absorber thickness on capacitance-voltage profiling of CdTe thin-film solar cells. *Solar Energy Materials and Solar Cells*, 100(0):126 – 131, 2012. Photovoltaics, Solar Energy Materials, and Technologies: Cancun 2010.
- [42] Kuo-Jui Hsiao and James R. Sites. Electron reflector to enhance photovoltaic efficiency: application to thin-film CdTe solar cells. *Progress in Photovoltaics: Research and Applications*, 20(4):486–489, 2012.
- [43] D. E. Swanson, R. M. Geisthardt, P. S. Kobyakov, J. M. Raguse, J. Drayton, K. L. Barth, J. R. Sites, and W. S. Sampath. Reduction of carrier recombination by the addition of a $\text{Cd}_{1-x}\text{Mg}_x\text{Te}$ electron reflector film. In *40th IEEE Photovoltaic Specialists Conference*, 2014.
- [44] J.M. Kephart, R. Geisthardt, and W. S. Sampath. Sputtered, oxygenated CdS window layers for higher current in CdS/CdTe thin film solar cells. In *38th IEEE Photovoltaic Specialists Conference*, pages 000854–000858, 2012.
- [45] Zhixun Ma, James McCamy, Jason M. Kephart, Russell M. Geisthardt, W. S. Sampath, Victor V. Plotnikov, and Alvin Compaan. Superstrate design for increased CdS/CdTe solar cell efficiencies. In *39th IEEE Photovoltaic Specialists Conference*, 2013.
- [46] Galymzhan T. Koishiyev. *Analysis of Impact of Non-Uniformities on Thin-Film Solar Cells and Modules with 2-D Simulations*. PhD thesis, Colorado State University, 2010.
- [47] Jason Hiltner. *Investigations of Spatial Variations in Collection Efficiency of Solar Cells*. PhD thesis, Colorado State University, 2001.

- [48] Mohammed Abdulaziz Tashkandi. *Pinholes and morphology of CdS films : the effect on the open circuit voltage of CdTe solar cells*. PhD thesis, Colorado State University, 2012.
- [49] Jason M. Kephart, Russell M. Geisthardt, Zhixun Ma, James McCamy, and W.S. Sampath. Reduction of window layer optical losses in CdS/CdTe solar cells using a float-line manufacturable HRT layer. In *39th IEEE Photovoltaic Specialists Conference*, 2013.
- [50] Russell M. Geisthardt and James R. Sites. Nonuniformity characterization of CdTe solar cells using LBIC. *IEEE Journal of Photovoltaics*, PP(99):1–5, 2014.
- [51] M. Gloeckler, I. Sankin, and Z. Zhao. CdTe solar cells at the threshold to 20% efficiency. In *39th IEEE Photovoltaics Specialists Conference*, 2013.
- [52] Keiichi Ohata, Junji Saraie, and Tetsuro Tanaka. Optical energy gap of the mixed crystal $\text{CdS}_x\text{Te}_{1-x}$. *Japanese Journal of Applied Physics*, 12(10):1641–1642, 1973.
- [53] David P. Ostrowski, Micah S. Glaz, Brian W. Goodfellow, Vahid A. Akhavan, Matthew G. Panthani, Brian A. Korgel, and David A. Vanden Bout. Mapping spatial heterogeneity in $\text{Cu}(\text{In}_{1-x}\text{Ga}_x)\text{Se}_2$ nanocrystal-based photovoltaics with scanning photocurrent and fluorescence microscopy. *Small*, 6(24):2832–2836, 2010.
- [54] M. S. Leite, M. Abashin, H. J. Lezec, A. G. Gianfrancesco, A. A. Talin, and N. B. Zhitenev. Mapping the local photoelectronic properties of polycrystalline solar cells through high resolution laser-beam-induced current microscopy. *IEEE Journal of Photovoltaics*, 4(1):311–316, 2014.
- [55] Takashi Fuyuki and Athapol Kitiyanan. Photographic diagnosis of crystalline silicon solar cells utilizing electroluminescence. *Applied Physics A*, 96(1):189–196, 2009.
- [56] Matevž Bokalič, John Raguse, James R. Sites, and Marko Topič. Analysis of electroluminescence images in small-area circular CdTe solar cells. *Journal of Applied Physics*, 114(12):123102, 2013.

- [57] Katherine Zaunbrecher, Steve Johnston, and James R. Sites. Analysis of thin-film inhomogeneities using electroluminescence and LBIC measurements. In *39th IEEE Photovoltaics Specialists Conference*, 2013.
- [58] Jennifer Drayton, Russell Geisthardt, John Raguse, and James Sites. Various passivation treatments on CdTe solar cells. In *2013 MRS Spring Meeting*, 2013.
- [59] Katherine Zaunbrecher. *Imaging as Characterization Techniques for Thin-Film Cadmium Telluride Photovoltaics*. PhD thesis, Colorado State University, 2014.